CONFORMAL COATING AND SHAPE-PRESERVING CHEMICAL CONVERSION OF BIO-ENABLED AND SYNTHETIC 3-DIMENSIONAL NANOSTRUCTURES

by

Jiaqi Li

A Dissertation

Submitted to the Faculty of Purdue University

In Partial Fulfillment of the Requirements for the degree of

Doctor of Philosophy

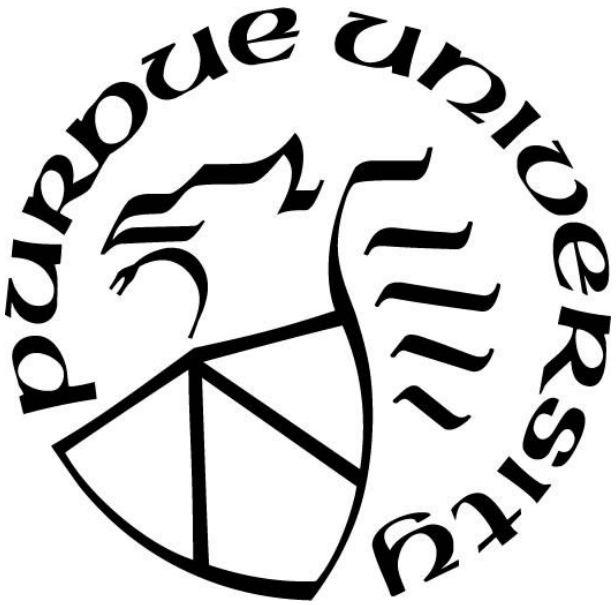

School of Materials Engineering

West Lafayette, Indiana

December 2020

THE PURDUE UNIVERSITY GRADUATE SCHOOL
STATEMENT OF COMMITTEE APPROVAL

Dr. Kenneth H. Sandhage, Chair
School of Materials Engineering

Dr. Kevin P. Trumble
School of Materials Engineering

Dr. Jeffrey P. Youngblood
School of Materials Engineering

Dr. Eric P. Kvam
School of Materials Engineering

Approved by:
Dr. David F. Bahr

To my parents.

ACKNOWLEDGMENTS

My sincerest thanks are extended to my advisor, Professor Kenneth Sandhage, for his guidance and support over the past five years here at Purdue. I appreciate the freedom he has given to me to explore research topics that triggered my interest, and the rigorous scientific research methods he has taught me to find the solution. His knowledge, diligence and passion have set a great example and will continue to influence me in my future career. I would also like to thank my committee members, Professor Kevin Trumble, Professor Jeffrey Youngblood, and Professor Eric Kvam for their constructive critiques and support for my research endeavors at Purdue.

I have been fortunate to work with and learn from many bright minds in a distinguished lab. Dr. Mario Caccia and Dr. Grigorios Itskos have been wonderful research scientists who have helped with my research and manuscript writing. I would like to express gratitude to now Dr. Sunghwan Hwang, for obtaining beautiful TEM images included in this work, and for his immense help as a teammate. Many thanks also go to Naotaka Ogura, Alexander Strayer, Adam Caldwell, Supattra Singnisai, Dr. Meysam Tabandeh, and Dr. Morteza Adinehnia for together setting up facilities in a vast empty lab when we started at Purdue, and for your supports and friendship.

Some work wouldn't have been possible without collaborations with hard-working and intelligent individuals who expanded the scope of my research. I'd like to thank Dr. Vincent Chen, Dr. Taylor Allen, Dr. Joseph Perry, Mihit Parekh, Dr. Dhanya Puthusseri, Dr. Vilas Pol, Dr, Michael Allen and Dr. Dimitri Deheyn for their efforts to conduct measurements for my samples and numerous valuable discussions. I thank Professor Jeffrey Youngblood, Professor John Howarter and their former graduate students for use of equipment and helpful trainings. Likewise, I thank Dr. Chris Gilpin, Laurie Muller, and Dr. Andrew White for their help with characterization tools and advice.

To my parents who made me what I am today, I am deeply grateful to you for allowing your only child to be 7000 miles away for 5 years. I couldn't have accomplished my goals without your unconditional love and support. To my loving grandparents, aunts, cousins and friends in China, you have no idea how much your continued care and encouragement meant to me. I look forward to reuniting soon. To my friends here, thank you for taking weekend trips to the best city Chicago with me when days got too repetitive. Thank you for the great laughs and memories.

TABLE OF CONTENTS

LIST OF TABLES

LIST OF FIGURES

LIST OF SYMBOLS AND ABBREVIATIONS

3D	Three Dimensional
A.U.	Arbitrary Units
AFM	Atomic Force Microscopy
BSE	Back Scattered Electron
DI	Deionized
EDS	Energy Dispersive X-ray Spectroscopy
FIB	Focused Ion Beam
EtOH	Ethanol
IR	Infrared
λ	Wavelength (nm)
M. rhetenor	*Morpho rhetenor*
QCM-D	Quartz Crystal Microbalance with Dissipation
RT	Room Temperature
SE	Secondary Electron
SEM	Scanning Electron Microscopy
SSG	Surface Sol Gel
TEM	Transmission Electron Microscopy
TEOS	Tetraethyl Orthosilicate
XRD	X-ray Diffraction

ABSTRACT

Impressive examples of the generation of hierarchically-patterned, three-dimensional (3-D) structures for the control of light can be found throughout nature. *Morpho rhetenor* butterflies, for example, possess scales with periodic parallel ridges, each of which consists of a stack of thin (nanoscale) layers (lamellae). The bright blue color of *Morpho* butterflies has been attributed to controlled scattering of the incident light by the lamellae of the wing scales. Another stunning example is the frustule (microshell) of the *Coscinodiscus wailesii* diatom, which is capable of focusing red light without possessing a traditional lens morphology. The photonic structures and the optical behaviors of *Morpho* butterflies and *Coscinodiscus wailesii* diatoms have been extensively studied. However, no work has been conducted to shift such light manipulation from the visible to the infrared (IR) range via shape-preserving conversion of such biogenic structures. Controlling IR radiation (i.e., heat) utilizing biogenic or biomimetic structures can be of significant utility for the development of energy-harvesting devices. In order to enhance the optical interaction in the IR range, inorganic replicas of biogenic structures comprised of high-refractive-index materials have been generated in this work. Such replicas of *Morpho rhetenor* scales were fabricated via a combination of sol-gel solution coating, organic pyrolysis, and gas/solid reaction methods. Diatomimetic structures have also been generated via sol-gel coating, gas/solid reaction, and then patterning of pore arrays using focused ion beam (FIB) milling.

Throughout the sol-gel solution coating and chemical conversion steps of the processes developed in this study, attention was paid to preserve the starting shapes of the nanopatterned, microscale biogenic or biomimetic structures. Factors affecting such shape preservation included the thicknesses and uniformities of coatings applied to the biogenic or biomimetic templates, nano/microstructural evolution during thermal treatment, and reaction-induced volume changes. A conformal surface sol-gel (SSG) coating process was developed in this work to generate oxide replicas of *Morpho rhetenor* butterfly scales with precisely-controlled coating thicknesses. The adsorption kinetics and relevant adsorption isotherm of the SSG process were investigated utilizing a quartz crystal microbalance. Analyses of thermodynamic driving forces, rate-limiting kinetic steps, and volume changes associated with various chemical reactions were used to tailor processing parameters for optimized shape preservation.

1. SYNTHESIS OF SOL-GEL DERIVED SILICA THIN FILMS AND CHEMICAL CONVERSION INTO HIGH REFRACTIVE INDEX MAGNESIUM SILICIDE

1.1 Introduction

Magnesium silicide (Mg_2Si) thin films have attracted significant attention owning to their unique thermal, electrical and optical properties [1–3]. Numerous studies have investigated the applications of Mg_2Si thin films in optoelectronic [4–7], thermoelectric [8–11], and superconducting devices [12]. Another attraction of using Mg_2Si for such applications is the relative abundance in the earth's crust, and the non-toxicity, of the constituent elements [13, 14]. Several synthesis techniques have been developed to fabricate Mg_2Si thin films for functional devices, including solid-state growth [13, 15–17], gas/solid reaction [18–20], molecular beam epitaxy [21], ion beam sputtering [22–24], and pulsed laser deposition [12, 21, 25]. However, these techniques either require high-vacuum equipment, and/or are line-of-sight processes, which can be expensive and difficult to scale up.

For more than six decades, sol-gel processing using metal alkoxide precursors has been used to prepare ceramic thin films and functional coatings using methods such as spin coating, dip coating, etc [26]. Spin coating is a commonly used technique to deposit thin films prepared from liquid precursors for production of microelectronic and semiconductor devices. Spin coating can generate uniform, contamination free, single side coatings, and allows for a relatively fast optimization; that is, parameters like spin speed, time, etc. are easily tuned for a given application [27]. A number of papers have been published on the preparation and optimization of sol-gel derived silica thin films by spin coating, with explanations provided on the effects of precursor choice [28], catalyst [26,27], temperature [31], and additives [32, 33], as well as spin speed and time [27] on the film thickness, structure, and chemistry.

Here, we propose an innovative method to fabricate thin Mg_2Si films that combines spin coating of a silica sol-gel solution on a flat substrate, thermal treatment to yield a SiO_2 film, and chemical conversion of the SiO_2 into Mg_2Si. After obtaining the SiO_2 thin film, a magnesiothermic reduction reaction was performed to convert the thin film into MgO/Si. MgO was then selectively dissolved using an acid solution, and the resulting porous Si films were reacted with Mg vapor to form crack-free Mg_2Si thin films with uniform thicknesses.

This work demonstrates, for the first time, the viability of fabricating dense, uniform, and crack-free Mg_2Si thin films (thickness ≤ 200 nm) via a combination of sol-gel processing and chemical conversion. Compared to other methods developed to fabricate Mg_2Si thin films, this approach doesn't require complex facilities that need high maintenance (e.g., ion beam sputtering, pulsed laser deposition), and is relatively easy to scale up.

The purpose of this chapter is to introduce and evaluate the innovative fabrication processes developed to generate high refractive index Mg_2Si thin films via sol-gel solution spin coating and chemical conversion. The density, uniformity, and porosity of the thin films were observed by electron microscopies. The reaction thermodynamics during the chemical conversion reactions from SiO_2 to Mg_2Si were calculated and discussed. Furthermore, thin film volumetric expansion from SiO_2 to Mg_2Si was also evaluated in this chapter to better understand the shape preservation throughout the fabrication processes.

1.2 Experimental Procedures

1.2.1 Silica Sol-gel Synthesis

Tetraethyl orthosilicate (TEOS, 98 % purity, Fisher Scientific, Hampton, NH, USA) was first diluted with anhydrous ethanol (99.5 % purity, 200 proof, Fisher Scientific, Hampton, NH, USA) to a 50 vol % solution. The TEOS/ethanol solution was then mixed with deionized (DI) water and 0.5 M hydrochloride acid (HCl, Fisher Scientific, Hampton, NH, USA) in a 1:4:4 molar ratio, and heated up to 70˚C with refluxing for 2 h. Then the mixture was cooled to room temperature (25 ± 2 ˚C) and blended with a methylcellulose (MC)-bearing aqueous solution so as to yield a methylcellulose : SiO_2 weight ratio of 22 : 78. The methylcellulose-bearing solution was prepared by mixing 0.30 g methylcellulose powder (A15C, Willpowder, Miami Beach, Florida, USA) with 15 mL DI water to yield a 2 wt % solution. The MC-bearing sol-gel solution was stirred using a magnetic stirring bar spinning at 300 rpm for 30 h at room temperature to allow for polymerization of the silica sols before spin coating.

1.2.2 Spin Coating of Silica Sol-gel Films

Prior to spin coating, a sapphire wafer (2" diameter, C-M plane, thickness 430 μm, double-side-polished, Roughness $R_a \leq 0.3$ nm, University Wafer, Boston, MA, USA) was cleaved into 1

cm x 1 cm square pieces with a diamond scoring pen (McMaster-Carr, IL, USA). The substrate was cleaned by ultrasonicating in DI water and then acetone for 10 mins each, and dried with nitrogen (99.9% purity, Air Gas, Radnor, PA, USA) at room temperature for 2 mins, with a flow rate of 1 cfm (cubic feet per minute). The substrate was then cleaned in a UV Ozone cleaner (ProCleaner^{TM} Plus, BioForce, Nanoscience, Salt Lake City, UT, USA) for 20 mins at room temperature to remove the organic residues immediately before spin coating. For spin coating, a cleaned substrate was first placed on the wafer chuck of the spin coater (650 Series, Laurell Technologies Corporation, North Wales, PA, USA). Attention was made to ensure that the center of the substrate was aligned with the center of the chuck. After a vacuum was used to apply suction to fix the substrate, the methylcellulose-bearing silica sol-gel solution was quickly applied (within seconds) to the sapphire substrate using a pipette until the whole surface area was covered by the sol-gel solution. Approximately 2 mL solution was needed to cover the whole sapphire substrate surface. Two different spin coating speeds were used for this study: 3000 rpm and 5000 rpm. The spin time was 20 seconds and the acceleration rate used was 1500 rpm/s.

1.2.3 Organic Removal and Conversion to Oxide Films

After spin coating of the silica sol-gel solution onto a sapphire substrate, the as-coated film was aged at room temperature overnight (~ 12 h) in a desiccator, and then dried in an oven at 60˚C under vacuum (0.7 mTorr) for 2 h. To remove the organics and convert the film into SiO_2, the as-dried film was placed on an alumina plate (Tateho Ozark Technical Ceramics, Webb City, MO, USA) in a horizontal tube furnace (Sentro Tech Corp, Strongsville, OH, USA) and heated at 2 ˚C/min to 700 ˚C in ambient stagnant air and held for 30 mins. The furnace was then cooled at 2 ˚C/min to room temperature before removal of the sample from the furnace.

1.2.4 Conversion to MgO/Si Films and Porous Si Films

The silica films were chemically converted into MgO/Si films via gas/solid magnesiothermic reduction, using Mg_2Si granules (3-12 mm pieces, 99.99 % purity, Alfa Aesar, Haverhill, MA, USA) as the Mg vapor source. The reactions during this step were as follows:

$$Mg_2Si(s) \rightarrow 2Mg(g) + Si(s) \qquad \text{Reaction. 1.1}$$

$$SiO_2(s) + 2Mg(g) \rightarrow 2MgO(s) + Si(s) \qquad \text{Reaction. 1.2}$$

The SiO_2 film was placed in a Ti boat prepared from folded Ti foil (thickness 0.1 mm, 99.9 % purity, MTI Corporation, Richmond, CA, USA). The SiO_2 film was exposed to Mg vapor generated from Mg_2Si granules that were placed on top of a low-carbon steel mesh sheet (0.024 inch thickness, 0.033 inch hole diameter, 28 % open area, 0.055 inch hole center-to-center, McMaster-Carr, IL, USA), which was placed on top of a Ti boat, as shown in Figure 1.1, The distance from the mesh to the film surface was 0.5 cm. The reactants were enclosed in a low-carbon steel tube (9" long, 1 ¼" diameter, McMaster-Carr, Elmhurst, IL, USA). The two openings of the tube were flattened with a shop press and welded shut in an Argon atmosphere glovebox ($p(O_2)$ < 0.1 ppm, Vacuum Atmosphere Company, Hawthorne, CA, USA) to avoid oxidation of the reactants and products (i.e., Mg_2Si and Si). The closed ampoule was then heated at 2˚C/min to 750 ˚C in flowing ultra-high-purity Ar (99.999 %) in a horizontal tube furnace and held at this temperature for 6 h. After the furnace cooled to room temperature, the steel ampoule was removed from the furnace and cut open with a horizontal band saw. Samples were removed from the ampoule for further processing.

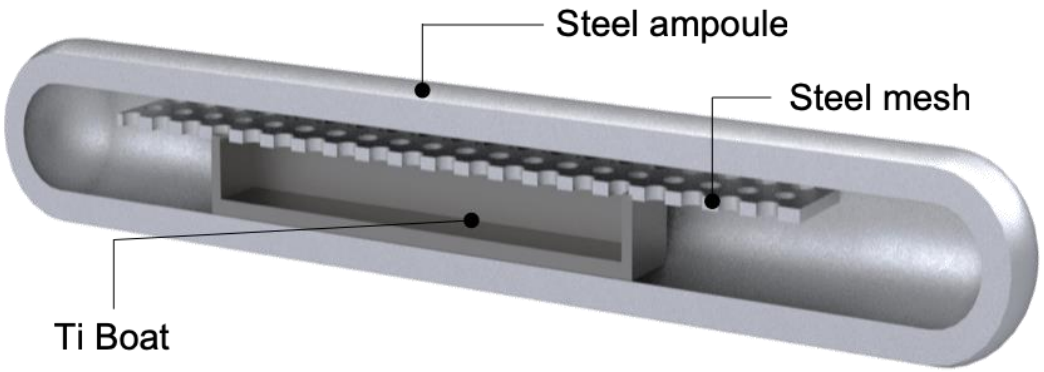

Figure 1.1. Schematic illustration of the cross section of a steel ampoule used for the magnesiothermic reduction reaction.

Selective acid dissolution of the MgO from the MgO/Si film was conducted using a 3M HCl aqueous solution. To minimize oxidation of the product porous Si film, such acid dissolution was conducted in the Ar atmosphere glovebox ($p(O_2)$ < 0.1 ppm). Immersion of the MgO/Si film in 3M HCl (aq) for 0.5 h was sufficient to remove MgO to yield a porous Si film. The film was then rinsed by immersing the film in DI water for 30 seconds ($MgCl_2$ would precipitate out during

drying if this rinsing step was skipped). After rinsing, the film was dried inside a glovebox (humidity < 0.5 ppm) for 12 h at room temperature.

1.2.5 Gas-Solid Conversion into Mg_2Si Films

The resulting porous Si film (after acid dissolution) was exposed to Mg vapor to generate Mg_2Si:

$$2Mg(g) + Si(s) \rightarrow Mg_2Si(s) \qquad \text{Reaction. 1.3}$$

For this chemical reaction, Mg foil (99.95 % purity, 0.5 mm thickness, Solution Materials, Santa Clara, CA, USA) was used as the Mg vapor source. The Si film was placed in a Ti boat, and the Mg foil was placed on top of the boat, as shown in Figure 1.2. The distance (L) from the Mg foil to the surface of the Si film was 0.5 cm. The reactants (Si films and Mg foil) were sealed in a steel ampoule prepared in the same way as for magnesiothermic reduction. The sealed ampoule was heated to 600 ˚C at 2˚C/min and kept for 2 h in a tube furnace with high purity Argon (99.999 %) gas flow. Sample was removed out of the ampoule after cutting the ampoule open at room temperature.

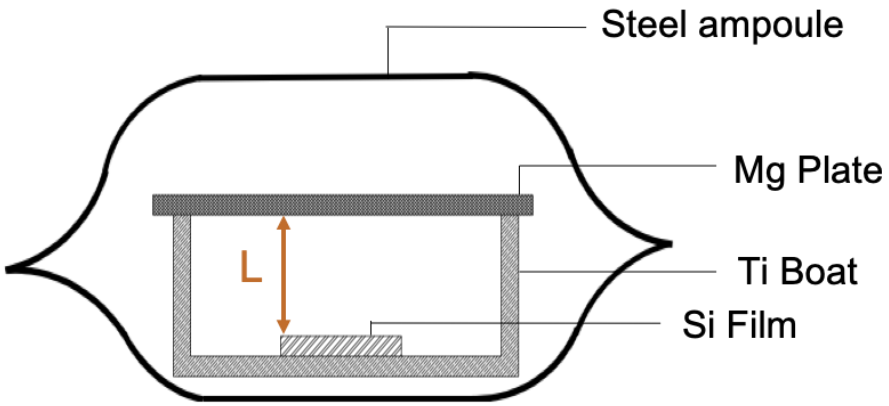

Figure 1.2. A schematic drawing of a steel ampoule made for converting a Si film into Mg_2Si.

1.2.6 Morphology and Phase Analyses

Top-down secondary electron (SE) images and focused ion beam (FIB) milling were acquired and conducted with a FEI Quanta 3D Field-emission Dual-beam Secondary Electron Microscope (SEM, Hillsboro, Oregon, USA). FIB milling was conducted using a 30 keV

accelerating voltage and ion beam currents ranging from 15 to 0.5 nA, with lower current used for more refined milling. Electron dispersive X-ray analyses (EDS) were conducted using an Oxford INCA Xstream-2 silicon drift detector with a Xmax80 window.

The transmission electron microscope (TEM) images were acquired with a Titan 80-300 kV Environmental Transmission Electron Microscope, operated at 300 keV. The surface roughness measurements were conducted using an Atomic Force Microscope (AFM) (NanoScope IIIa, Digital Instruments, Veeco Metrology Group, Santa Barbara, CA, USA) with a n-doped Si cantilever that possessed a resonance frequency of 300 kHz (Bruker, Billerica, MA, USA).

Film thicknesses were measured from cross-sectional SE images by measuring perpendicular distance from 10 different locations and taking the average value.

1.2.7 Focused-ion-beam (FIB) Milling of A Light-focusing Pore Pattern and Optical Behavior of the Patterned Thin Films

Vogel and synthetic light-focusing patterns were generated using MATLAB (MathWorks, Natick, MA, USA). For naturally-derived diatomimetic patterns, a high contrast SEM image of a native *Coscinodiscus wailesii* diatom frustule was binarized in MATLAB and manually adjusted using Image J software (i.e., smoothing the hole edge, removing odd shaped holes, filling in holes that were omitted by imaging processing by manually drawing the outline around the holes) by Taylor Allen at Georgia Tech [34]. The pattern files were imported to the electron microscope and the patterns were applied to the thin films by focused ion beam (FIB) milling using an accelerating voltage of 30 keV and ion beam current of 0.1-3.0 nA. For SiO_2 films, a thin conductive carbon layer was deposited onto the films via a carbon coater (SPI Supplies, West Chester, PA, USA) using 7.5 V for 5 s with a carbon fiber (1 mm diameter, SPI Supplies, West Chester, PA, USA) to avoid charging. After milling, the carbon layer was easily removed by firing the film in ambient stagnant air at 500˚C for 1 h.

The refractive indices of thin films were measured using a J. A. Woollam M-2000UI Spectroscopic Ellipsometer with a 245-1690 nm wavelength range. Typical scans were obtained from angles of 65˚, 70˚, and 75˚. The beam spot size for standard and focusing measurements (for smaller area) was ca. 3 mm and 300 μm in diameter, respectively. To reduce back reflections causing deleterious oscillations of the double-side-polished sapphire substrate, the backside was roughened using a diamond scribe to make scratches on the back side. Far field imaging to measure

the focusing behavior of the pattern films was conducted using a custom-built, modular microscope system (Figure 1.3, Georgia Tech). The light source used was a TOPAS-COPA (pulse widths typically < 100 fs) pumped by regeneratively amplified femtosecond system at 795 nm (Solstice, Spectraphysics, pulse widths typically < 90 fs, repetition rate 1 kHz). All samples were evaluated at 550, 650, 750, 860, 950, and 1050 nm. A 40x objective (Olympus, UPlanFLN, NA = 0.75, WD = 0.5 mm) and a Lumera Infinity 2 CCD camera were used for imaging. The ellipsometry and focusing measurements were performed by our collaborator Taylor Allen from the group of Joseph Perry at Georgia Tech.

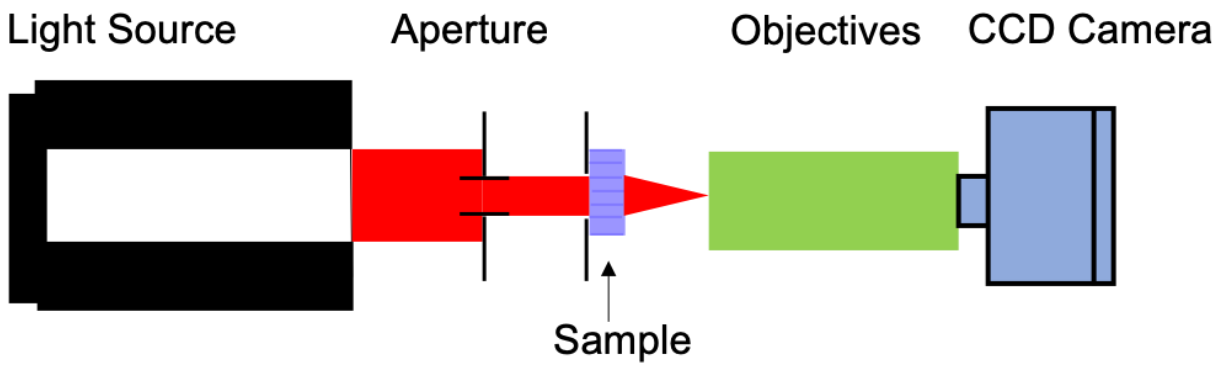

Figure 1.3. Schematic illustration of a light-focusing measurement setup (Perry Group, Georgia Tech).

1.3 Results and Discussion

1.3.1 Thermodynamic Analyses of Chemical Conversion Reactions

Traditional methods that have been used to convert SiO_2 into Si include carbothermal reduction [35] and electrochemical reduction in molten salts [36]. However, those methods either require high temperatures (≥2000˚C, which is above the Si melting temperature of 1414 ˚C) [35] or fail to retain the micro/nano structure of the initial silica reactants [36]. Previous work using the magnesiothermic reduction method to achieve shape-preserving transformation has been conducted by the Sandhage group [37–39]. During the reduction progress, there are four possible independent reactions between SiO_2 and Mg:

$$2Mg(g) + 3SiO_2 \rightarrow 2MgSiO_3 + Si \qquad \text{Reaction. 1.4}$$

$$2Mg(g) + 4MgSiO_3 \rightarrow 3Mg_2SiO_4 + Si \qquad \text{Reaction. 1.5}$$

$$2Mg(g) + Mg_2SiO_4 \rightarrow 4MgO + Si \qquad \text{Reaction. 1.6}$$

$$2Mg(g) + Si \rightarrow Mg_2Si \qquad \text{Reaction. 1.7}$$

The first two reactions can be considered as partial reduction of SiO_2, which results in forming magnesium silicate and Si. Reaction. 1.6 shows the complete reduction, indicating that the final product of such full conversion should be MgO and Si. If there is excess Mg (i.e., beyond the Mg content needed to complete SiO_2 reduction to Si), Reaction. 1.7 is favored to happen to form magnesium silicide, Mg_2Si. Since the reaction between Mg_2Si and SiO_2:

$$Mg_2Si + SiO_2 \rightarrow 2MgO + 2Si \qquad \text{Reaction. 1.8}$$

is highly favored (ΔG^o_{rxn} = -188.890 kJ/mol and -181.903 kJ/mol at 650˚C and 900˚C respectively [40, 41]), thermodynamically Mg_2Si would not be produced until all the SiO_2 is consumed. The corrected and better value for the standard enthalpy of formation of MgO was proposed by Gourishankar, *et al.* [41]. The new $\Delta_f H^0_{298}$ of MgO is ~ 34 kJ/mol more negative than the value provided in Reference # [40]. For all the thermodynamic calculations involving MgO, the $\Delta_f H^0_{298}$ (635.241 kJ/mol) from Gourishankar, *et al.* was used.

Prior work has been conducted to convert SiO_2 into MgO/Si via magnesiothermic reduction, with pure Mg metal used as the Mg vapor source [38, 42, 43]. If it is assumed that all the solid species involved in the above reactions are in a pure, stoichiometric state, and using pure, Raoultian reference frames, and the ideal gas assumption, then the reaction quotients can be approximated as a function of the partial pressure of magnesium p_{Mg} in the system. Assuming that Mg gas behaves like an ideal gas, and given the standard Gibbs formation energy ΔG_f^o values [40, 41], ΔG^o_{rxn} values for reaction (1.4)-(1.7) were calculated and are shown below.

Table 1-1. ΔG^{o}_{rxn} values of Reactions (1.4) – (1.7) when using Mg metal and Mg_2Si as the Mg vapor source, respectively.

Reaction	**Mg metal**		**Mg_2Si**	
	ΔG^{o}_{rxn} at 650˚C	ΔG^{o}_{rxn} at 900˚C	ΔG^{o}_{rxn} at 650˚C	ΔG^{o}_{rxn} at 900˚C
(1.4)	-337.6 kJ/mol	-324.8 kJ/mol	-266.5 kJ/mol	-261.3 kJ/mol
(1.5)	-293.5 kJ/mol	-273.1 kJ/mol	-222.5 kJ/mol	-209.6 kJ/mol
(1.6)	-197.0 kJ/mol	-183.3 kJ/mol	-125.9 kJ/mol	-119.7 kJ/mol
(1.7)	-71.0 kJ/mol	-63.5 kJ/mol	0 kJ/mol	0 kJ/mol

As discussed before, when there is an excess amount of Mg, Mg_2Si can start to form, and the overall reaction will be as follows:

$$4Mg(g) + SiO_2 \rightarrow Mg_2Si + 2MgO \qquad \text{Reaction. 1.9}$$

Although Mg_2Si is formed after this reaction, the product is not a single phase but rather an intermixed composite of MgO/Mg_2Si. The refractive index of MgO is relatively low (n=1.7 at 2 μm [44]), compared to Mg_2Si (3.74 at 10 μm [3]). In addition, the volume change of reaction (1.9) is around 126 % [45]. Such large compression stress induced by volume expansion could result in film buckling and cracking, thus reducing the film quality. However, if Mg_2Si is being used to generate Mg vapor, the ΔG^{o}_{rxn} value of reaction (1.7) is zero, so Mg vapor won't further react with Si to form Mg_2Si. The chemical reaction for this is as follows:

$$2Mg(g) + SiO_2 \rightarrow 2MgO + Si \qquad \text{Reaction. 1.10}$$

At 750 ˚C, which was the temperature chosen for magnesiothermic reduction for this study, the ΔG^{o} of reaction (1.10) is -318.5 kJ/mol [40, 41]. The equilibrium partial pressure of Mg vapor at 750 ˚C associated with reaction (1.7) ($p_{Mg(g)}[1.7] = 4.15 \times 10^{-4}$ atm) is much higher than that for reaction (1.10) ($p_{Mg(g)}[1.10] = 7.45 \times 10^{-9}$ atm). Hence, the Mg vapor generated from Mg_2Si granules was sufficient to drive the magnesiothermic reduction to form the product phases MgO and Si.

For the Mg_2Si conversion step, the Mg-Si phase diagram (Figure 1.4) shows that Mg_2Si is the only compound that forms between Mg and Si. Therefore, the chemical reactions during this step are as follows:

$Mg(s) \rightarrow Mg(g)$ Reaction. 1.11

$2Mg(g) + Si(s) \rightarrow Mg_2Si(s)$ Reaction. 1.12

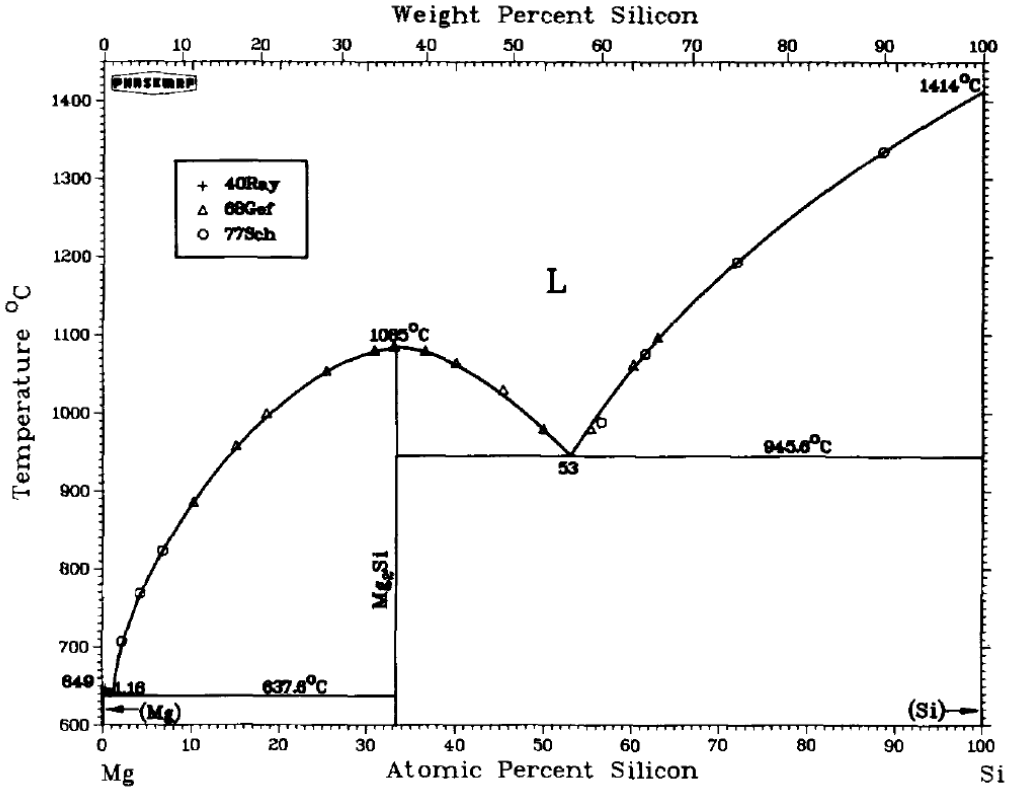

Figure 1.4. Phase diagram of Mg-Si (plot adopted from [46] with the publisher's permission).

ΔG^o of Reaction (1.12) at 600˚C is -166.3 kJ/mol [40]. At 600˚C, p_{Mg}[rxn(1.11)] is higher (1.46×10^{-3} atm) than p_{Mg}[rxn(1.12)] (1.06×10^{-5} atm) [40], so Mg vapor generated from Mg foil is sufficient to drive the Reaction 1.12 to the right.

1.3.2 Film Morphology and Microstructure

Silica sol-gel solutions with methylcellulose (MC) as an additive, and without MC, were prepared and spin coated on sapphire wafers at 3000 rpm for 20 s. The as-spun films were dried in a vacuum oven under vacuum (0.7 mTorr) at 60˚C for 2 h. Top-down SE images were obtained for the as-dried films, as shown in Figure 1.5. After firing at 700 ˚C for 0.5 h in air to allow for

organic pyrolysis, top-down SE images were taken of the as-fired films prepared from silica sol-gel with MC and without MC, as shown in Figure 1.6.

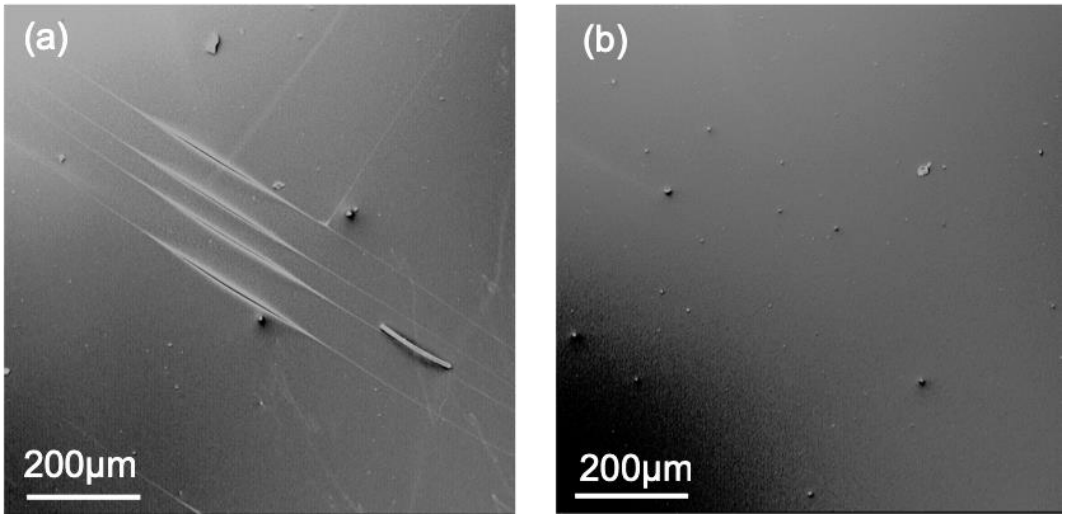

Figure 1.5. SE images of as-dried films prepared from spin coating (3000 rpm) of a silica sol-gel solution (a) without MC and (b) with MC.

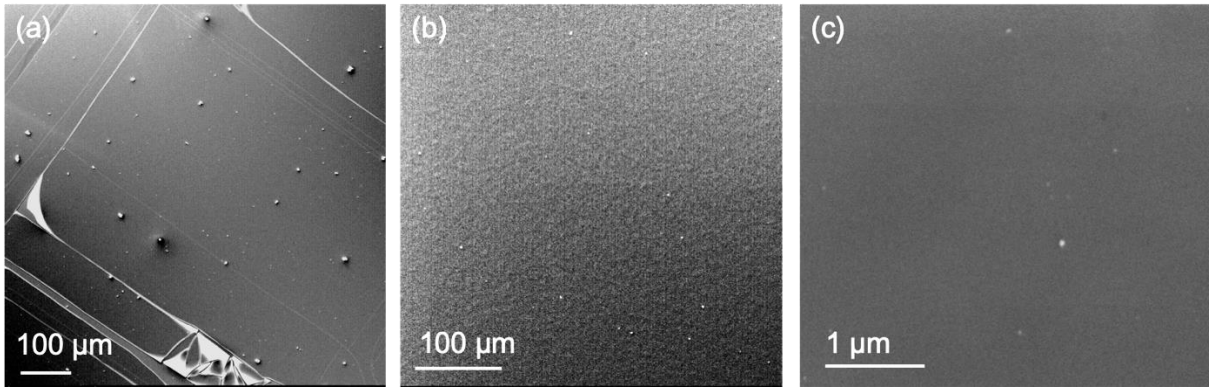

Figure 1.6. Top-down SE images of as-fired (700 ˚C for 0.5 h in air) SiO_2 films prepared from a silica sol-gel solution (spin coated at 3000 rpm) (a) without adding MC and (b)(c) with MC.

Without adding MC, the as-dried SiO_2 film was heavily cracked (Figure 1.5(a)). This cracking was caused by a significant volume shrinkage from the sol-gel polymer structure to a dense oxide structure. Methylcellulose has been successfully used as an additive in sol-gel processed SiO_2-TiO_2 composite thin films to enhance the quality of the sintered films (i.e., crack-free, uniform) [47]. In this case, the polymer additive was introduced to adjust the solution

viscosity, strengthen the gel network by filling the pores between the inorganic oxide chains, and act as a film toughening agent to prohibit the film from cracking upon drying (vacuum drying at 60 ˚C). Figure 1.5(b) confirmed that MC effectively prevented cracking in the as-dried SiO_2 film and yielded a dense, uniform layer after firing. A higher magnification image of an as-fired SiO_2 film in Figure 1.6(c) indicated that no micro-cracking was presented in the film. EDS analyses (Figure 1.7) of such films revealed the presence of appreciable Si and O, which was consistent with the formation of SiO_2. (Note: Al and O from the underlying sapphire substrate were also detected). In addition, the distribution of Si in the thin film according to the EDS mapping was similar over the film surface, indicating a uniform coating of silica on the sapphire substrate.

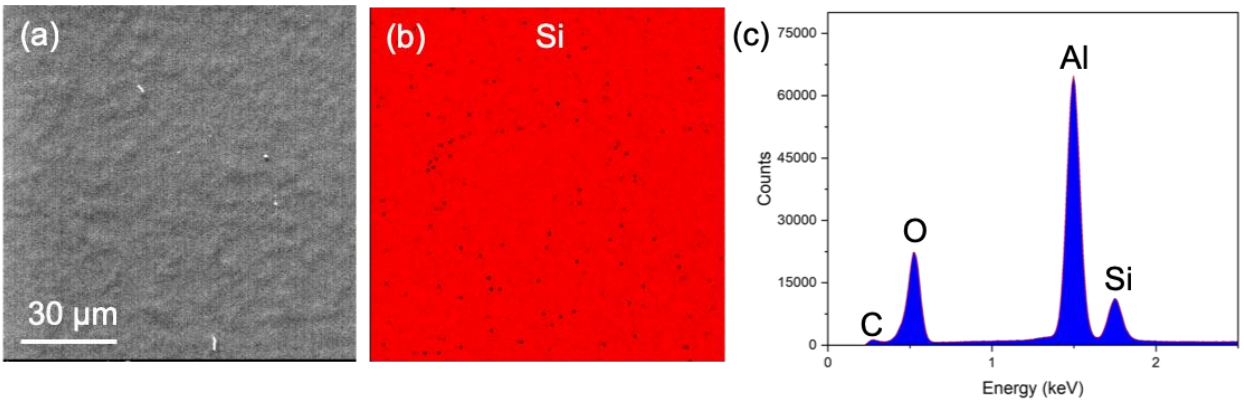

Figure 1.7. (a) SE image and (b) EDS mapping and (c) EDS spectra analyses of the as-fired (700 ˚C for 0.5 h in air) SiO_2 film spin coated on a sapphire substrate at 3000 rpm using a MC-bearing silica sol-gel solution.

The resulting dense, crack-free SiO_2 film was then reacted with Mg(g) generated from Mg_2Si granules for 6 h at 750 ˚C. The product MgO/Si film exhibited no obvious cracking as shown in Figure 1.8, EDS analyses of MgO/Si films indicated an appreciable amount of Mg, along with Si and O, which was consistent with the formation of MgO and Si products.

From SiO_2 to MgO/Si, the volume expansion ranges from 26% to 38% (depending on the type of SiO_2 formed after sol-gel spin coating and sintering in air) [29]. Such volumetric expansion cannot be ignored. S.C. Davis investigated the film stress evolution and relaxation during magnesiothermic reduction by exposing a quartz silica substrate to Mg vapor at high temperatures ranging from 650 – 900 ˚C [37]. During conversion from SiO_2 to MgO/Si, MgO crystals migrated to the top the MgO/Si layer to release the film internal compressive stress, and this stress-induced

migration helped prevent film cracking upon conversion. Indeed, in this study, Figure 1.8(b) showed MgO cubic crystals on top of the MgO/Si film after the reaction, which was further confirmed by the Mg distribution in Figure 1.8(c), and the film was free of micro-cracks and dense.

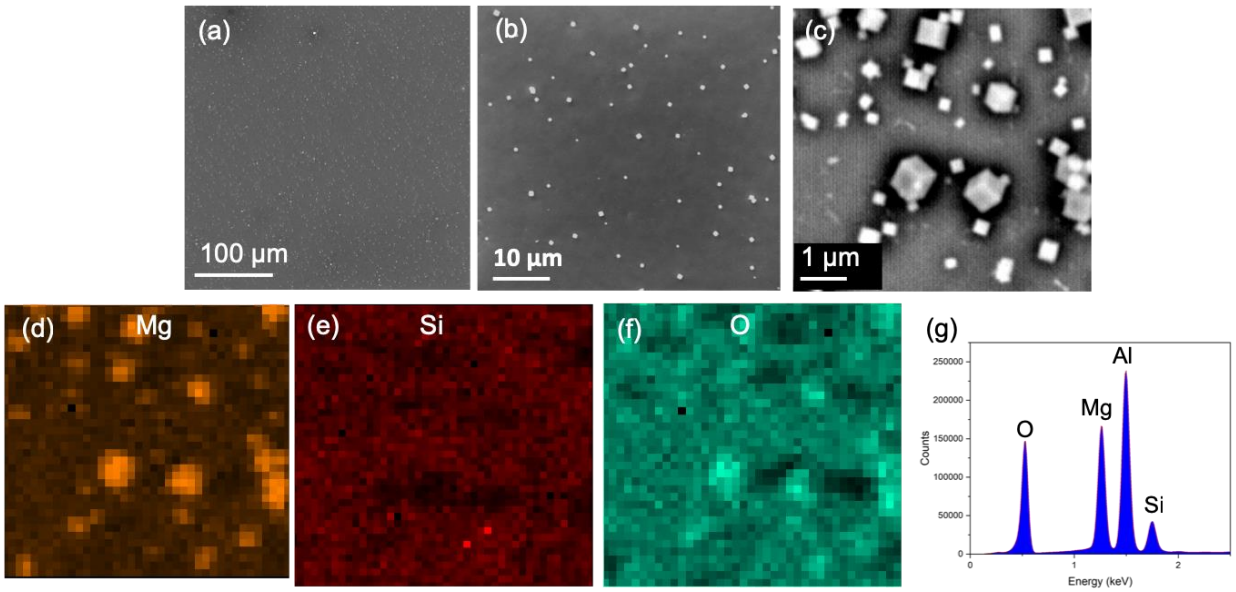

Figure 1.8. (a)(b)(c) Top-down SE images, EDS elemental mappings of (d) Mg, (e) Si, (f) O, and (g) EDS spectra of MgO/Si film after converting SiO_2 film (spin coated at 3000 rpm, fired in the air at 700 ˚C for 0.5 h) via magnesiothermic reduction at 750 ˚C for 6 h using Mg_2Si as the Mg vapor source.

Porous Si films were generated by immersing MgO/Si films in a 3 M HCl solution for 0.5 h, to selectively remove MgO, followed by rinsing in DI water. High magnification SE images and EDS analyses (Figure 1.9) revealed that the resulting dried, porous Si films were flat and free of macrocracks and magnesium.

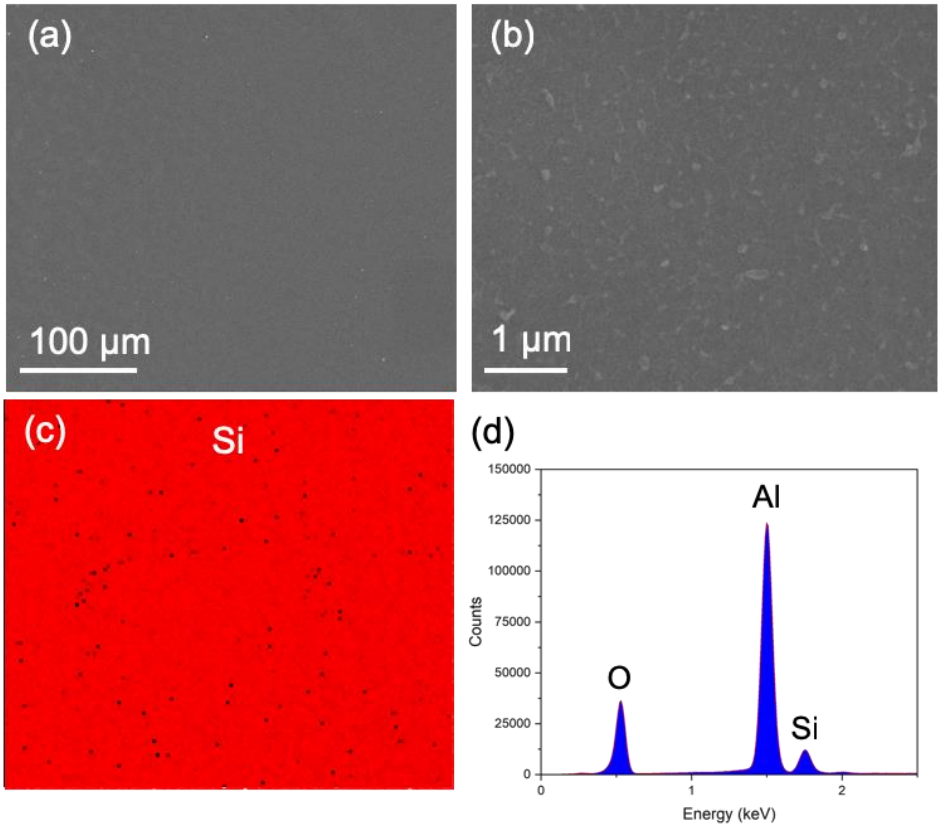

Figure 1.9. (a)(b) Top-down SE images and (c)(d) EDS analyses of a porous Si film prepared by spin coating a silica sol-gel at 3000 rpm for 20s, magnesiothermic reduction, and acid dissolution using 3 M HCl (aq) for 0.5 h.

Finally, the Si films were then exposed to Mg(g) generated from pure Mg metal foil at 600˚C for 2 h to form Mg_2Si. The quality of the converted final Mg_2Si thin film on a sapphire substrate was evaluated by SEM, EDS, and TEM, and the results are shown in Figure 1.10 and Figure 1.11. The resulting Mg_2Si film was crack-free and dense according to the top-down SE images in Figure 1.10 (a) and (b), although the surface was rougher than films from previous steps, probably due to grain coarsening (Figure 1.10(e)). EDS analyses (Figure 1.10(c)(d)(f)(g)) of the Mg_2Si film revealed appreciable presence of Mg and Si, and the atomic percentage ratio of Mg to Si was approximately 2:1, consistent with the formation of the product Mg_2Si.

Selected area electron diffraction (SAED) analyses and high-resolution TEM lattice fringe imaging of the films at each conversion stage further confirmed the phase content of the thin films. (Figure 1.11). TEM analyses of the SiO_2 film (spin coated at 3000 rpm) show a mixture phase of crystalline and amorphous silica. SAED analyses of the Mg_2Si film revealed a little MgO, probably

due to the oxidation of Mg_2Si when exposed in the air during transportation from TEM preparation (FIB milling and sample lift-out) to the TEM. For the converted final Mg_2Si film, TEM SAED analyses showed Mg_2Si diffraction and lattice fringe spacing values corresponding to Mg_2Si (111) and Mg_2Si ($1\bar{1}1$) (3.67 Å and 3.68 Å, respectively).

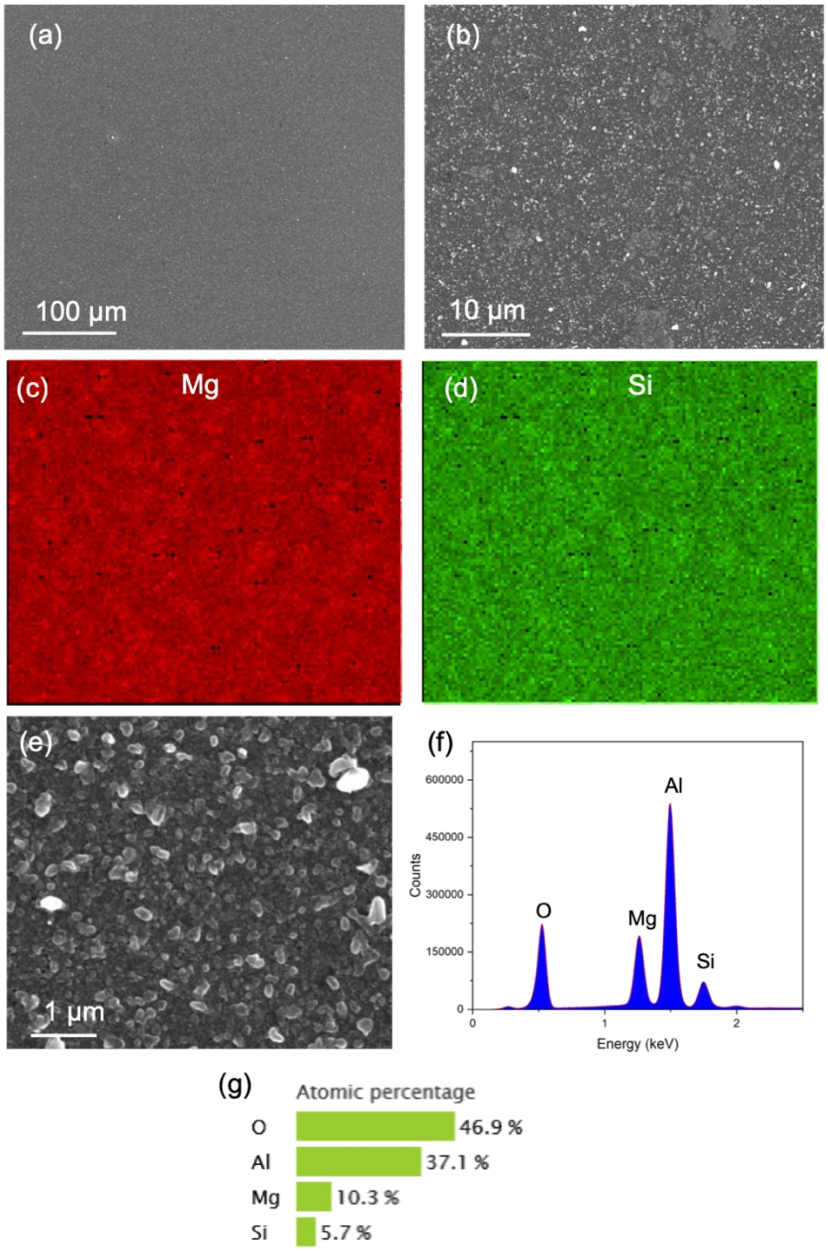

Figure 1.10. (a)(b) Top-down SE image of a converted Mg_2Si film from SiO_2 film (spin coated at 3000 rpm) on sapphire, (c)(d) Mg and Si EDS maps of the Mg_2Si film in (b), (e) High magnification top-down SE image of the Mg_2Si film, and (f)(g) EDS spectra and elemental quantification analyses of the Mg_2Si film.

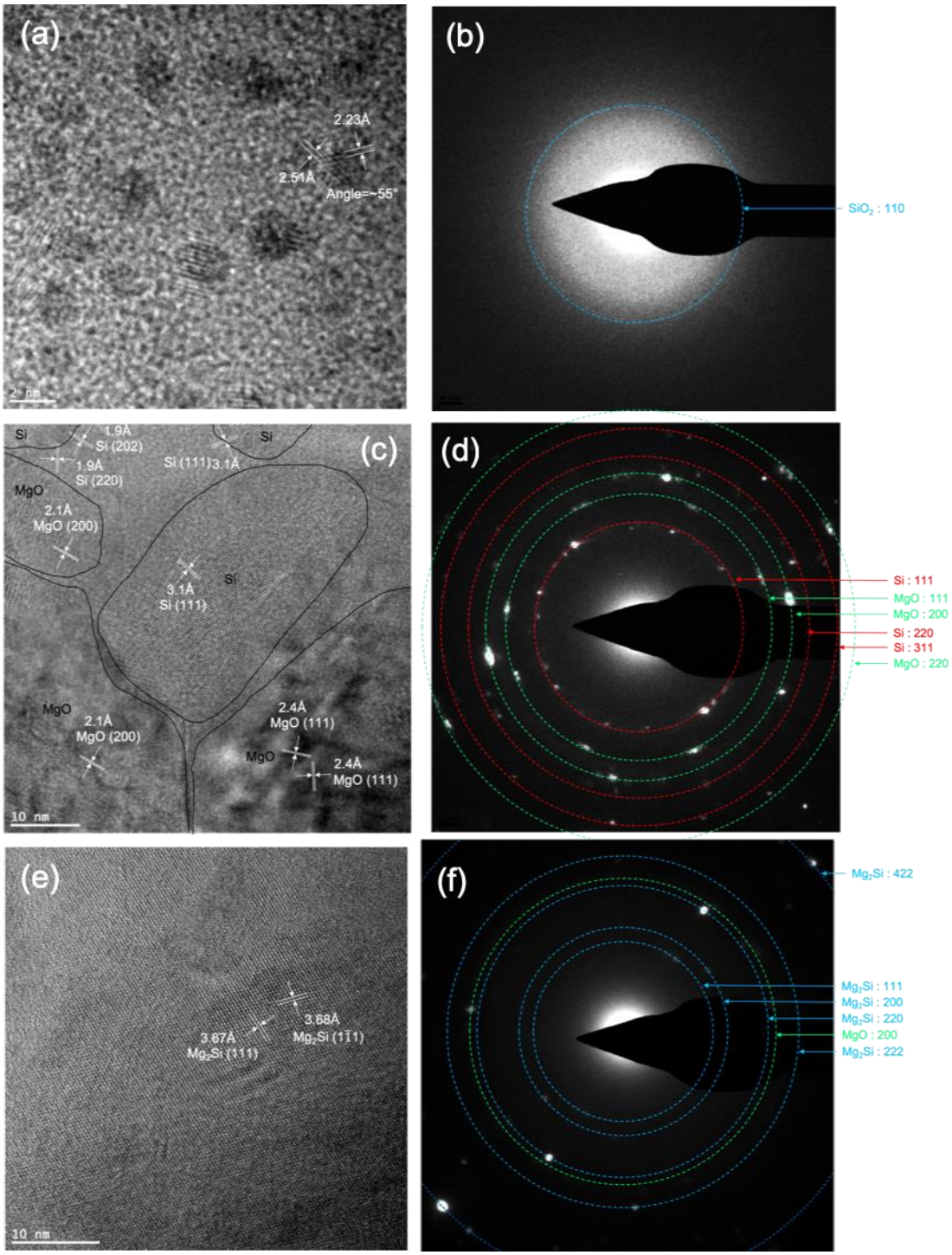

Figure 1.11. (a)(c)(e) High-resolution lattice fringe images and (b)(d)(f) selected area electron diffraction patterns of a SiO_2 film prepared by spin coating at 3000 rpm and sintered in the air at 700 ˚C for 30 min, a MgO/Si film after magnesiothermic reduction at 750 ˚C for 6 h, and a converted Mg_2Si film after reaction at 600 ˚C for 2 h. TEM courtesy of Sunghwan Hwang, Sandhage Group at Purdue University.

1.3.3 Film Volumetric Expansion

The molar volumes of SiO_2 [45], MgO, Si, and Mg_2Si are ~26 cm^3/mol, 11.26 cm^3/mol, 12.06 cm^3/mol and 38.58 cm^3/mol, respectively [48–50]. The solid volume difference upon reaction can be expressed by Equation 1.1:

$$\frac{\Delta V}{V_0} = \frac{\sum n_i \cdot V_{m,i} - V_{SiO_2}}{V_{SiO_2}} \times 100\% \qquad \text{Equation 1.1}$$

where V_{SiO_2} is the molar volume of silica, n_i is the number of moles of product i, and $V_{m,i}$ is the molar volume of product i.

Magnesiothermic reduction has been applied to convert SiO_2 to MgO/Si by numerous researchers, where Mg vapor was generated by Mg pure metal as opposed to Mg_2Si granules used in this study [38, 42, 43]. When using Mg pure metal as the vapor source for magnesiothermic reduction, the Mg vapor can further react with product Si to form an appreciable amount of Mg_2Si. Adjusting reaction temperature and time, as well as the distance between SiO_2 and the Mg source, could favor the formation of Mg_2Si or MgO/Si. It is, however, not possible to obtain phase pure Mg_2Si or MgO/Si after magnesiothermic reduction using pure Mg as the vapor source. Besides, the $\frac{\Delta V}{V_0}$ value of such reaction (Reaction (1.9)) is very large (around 126%), which would induce significant compression stress in the film and could cause undesirable film deformation, fracture, and delamination [51].

In this study, Mg_2Si granules were used as a Mg vapor source for SiO_2 reduction instead of pure Mg. Xia, *et al.* previously used Mg_2Si granules as the Mg vapor source to reduce SiO_2 at 650 – 850 ˚C [52]. The reasons and benefits are as follows. First of all, using Mg_2Si can prevent Mg vapor from further reacting with product Si, so a mixture of MgO and Si can be obtained. Second, the volume expansion when using Mg_2Si as the Mg vapor source for magnesiothermic reduction ($2Mg(g) + SiO_2 \rightarrow Si + 2MgO$) is only 26 % (compared to 126 % when using a Mg gas source in Reaction (1.9)), and such compression stress can be released partially by MgO migration to the surface of the film to prevent film cracking or buckling (confirmed in Figure 1.8). After completely dissolving MgO to form a porous Si film, the theoretical porosity of Si film is ~65 %. Since the molar volume of Mg_2Si (38.5 cc/mol) is slightly larger than that of 2MgO/Si (34.7 cc/mol), the pores generated during dissolution can be fully filled in to form a dense Mg_2Si film.

Ion-beam-milled film cross sections were obtained at each stage of conversion, and STEM imaging and mapping were used to measure the thickness of each film and the phase distribution within the film. The cross-sectional images further confirmed that the starting SiO_2 was dense, uniform and crack-free (Figure 1.12(a)). The thickness of the SiO_2 film was 202 ± 1 nm (± indicated a 95 % confidence range). After magnesiothermic reduction, the composite film consisted of an intertwined mixture of MgO and Si according to Mg and Si elemental mappings, as shown in Figure 1.12(b). The MgO/Si film thickness increased to about 270 ± 3 nm (± indicated a 95 % confidence range), exhibiting a ~30 % volume expansion from SiO_2 to MgO/Si, which falls in the theoretical volume expansion range (26 % - 38 %). However, the volume expansion from SiO_2 to Mg_2Si film was ~65 %, which was larger than the theoretical expansion derived from molar volumes of the species (41 % - 54 %). Indeed, Figure 1.12(c) showed that the final Mg_2Si film was neither uniform in thickness nor dense (i.e., the film was porous and exhibited buckling), which was consistent with such a large volume expansion. Furthermore, the correlation of the volume expansion with the film thickness increase was consistent with the volumetric expansion occurring predominantly in the film thickness direction. Therefore, preparing thinner films was examined to reduce reaction-induced stresses and to generate uniform and dense films.

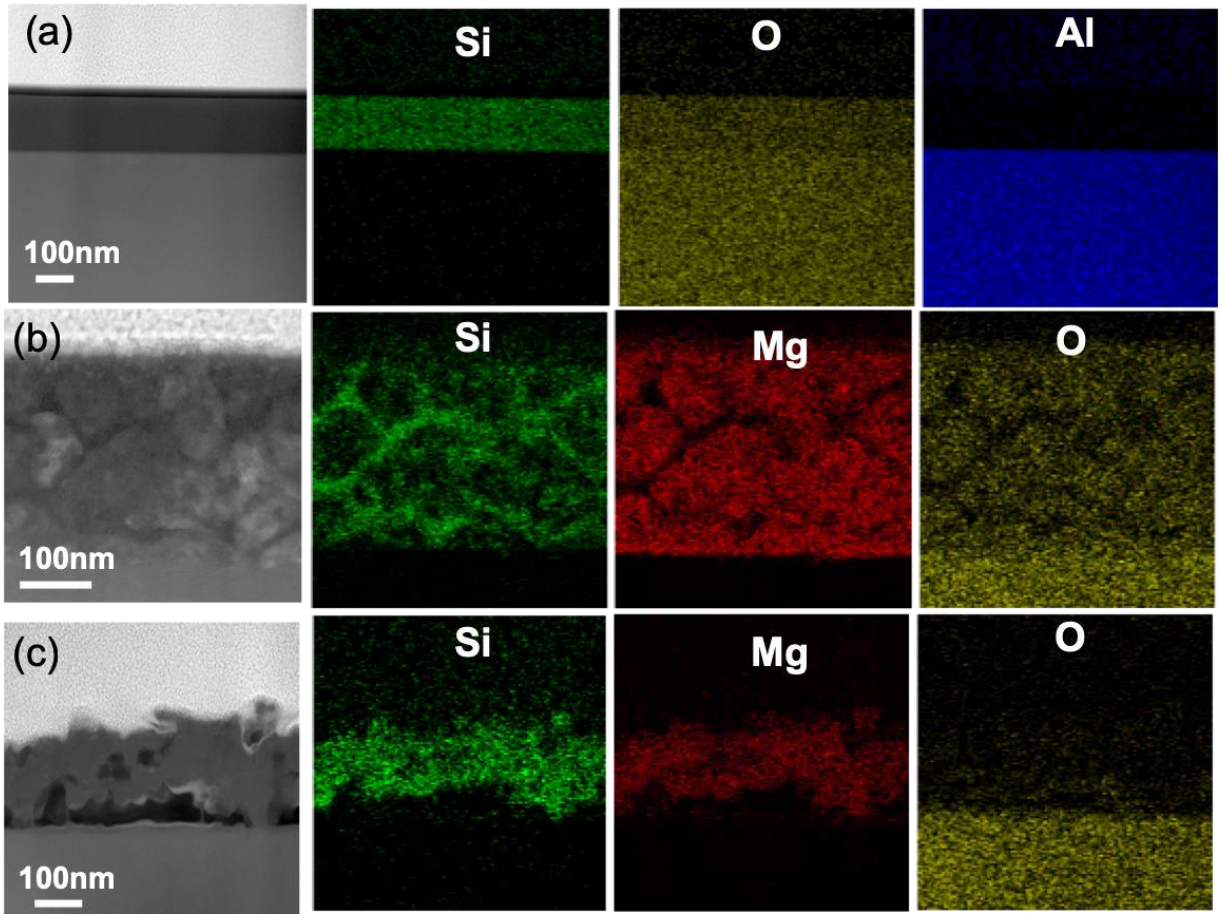

Figure 1.12. STEM imaging and elemental mapping on FIB cross sections of the (a) SiO_2, (b) MgO/Si and (c) Mg_2Si films on sapphire substrates (film preparation started from spin coating silica sol-gel solution at 3000 rpm). Courtesy of Sunghwan Hwang, Purdue University.

Table 1-2. Theoretical volume change and measured film thicknesses after each conversion step

Material	Molar Volume (cc/mol)	Theoretical Volume Expansion (%)	Film Thickness (nm)	Thickness Expansion (%)
SiO_2	~ 25.0 – 27.4	N/A	202 ± 1	N/A
2MgO/Si	34.6	26.3 – 38.4	270 ± 3	31.5 – 35.8
Mg_2Si	38.5	40.5 – 54.0	330 ± 15	55.2 – 71.6

Thinner films were then generated via spin coating the methylcellulose-bearing silica sol-gel solution on a sapphire substrate. Rotating at 5000 rpm spin speed was used, instead of 3000 rpm. The as-spun film was then dried, fired, and converted into a Mg_2Si film using the same

processing methods and conditioned as discussed above. Top-down SE images were obtained for the thinner films after each conversion stage, and cross-sectional SE images were acquired after milling the thin films with a focused ion beam.

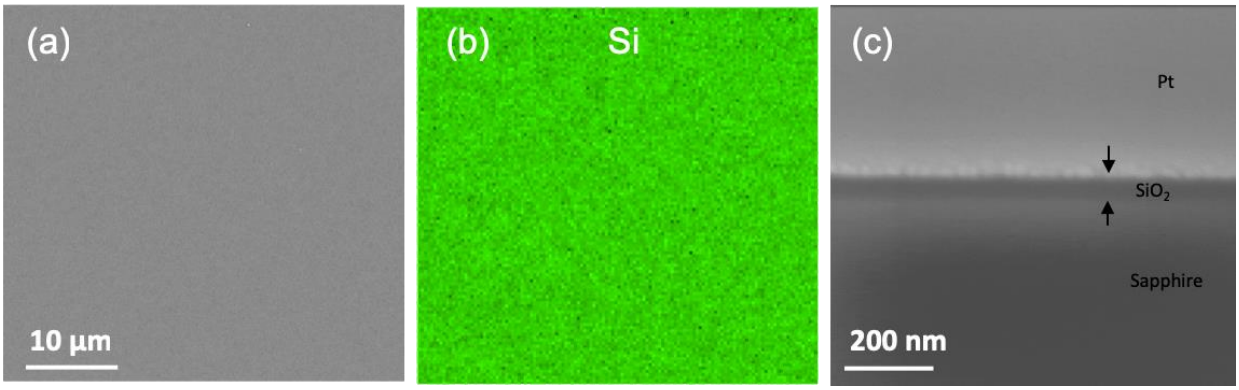

Figure 1.13. (a) Top-down SE image, (b) EDS Si map, and (c) FIB-milled cross-sectional SE image of a SiO_2 film with reduced thickness prepared by spin coating at 5000 rpm and sintered in air at 700 ˚C for 0.5 h.

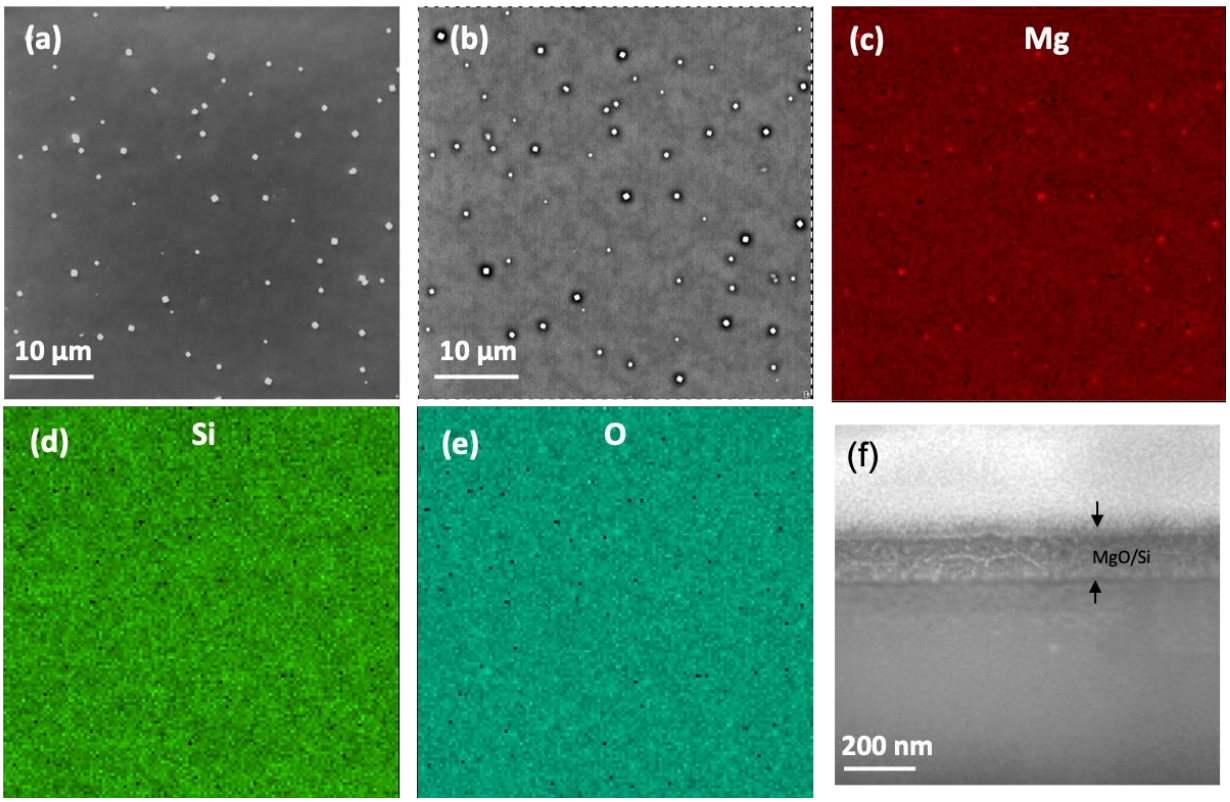

Figure 1.14. Top-down (a) SE and (b) BSE images, elemental mapping of (c) Mg, (d) Si, (e) O, and (f) cross-sectional SE image of a thickness-reduced MgO/Si film after magnesiothermic reduction at 750 ˚C for 6 h.

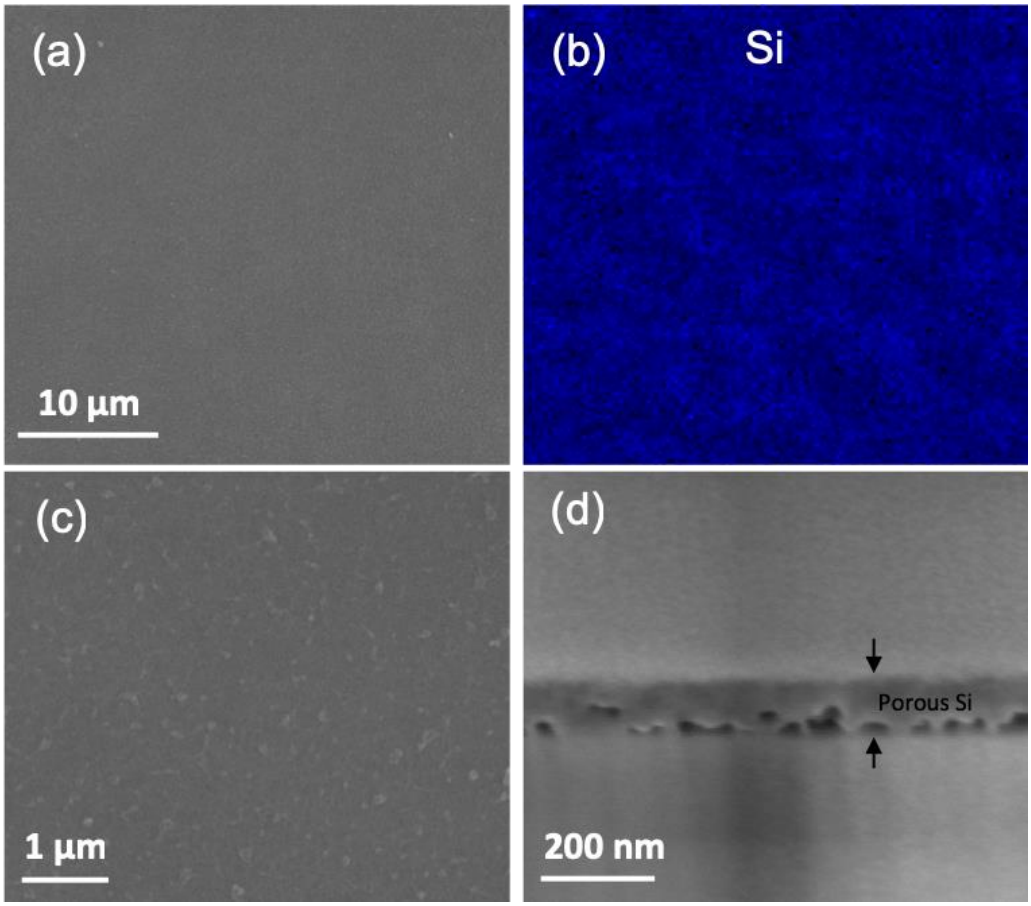

Figure 1.15. (a) Top-down SE image, (b) EDS elemental mapping of Si, (c) high magnification SE image, and (d) cross-sectional SE image of a thickness-reduced porous Si film after immersing a MgO/Si film in 1 M HCl for 0.5 h.

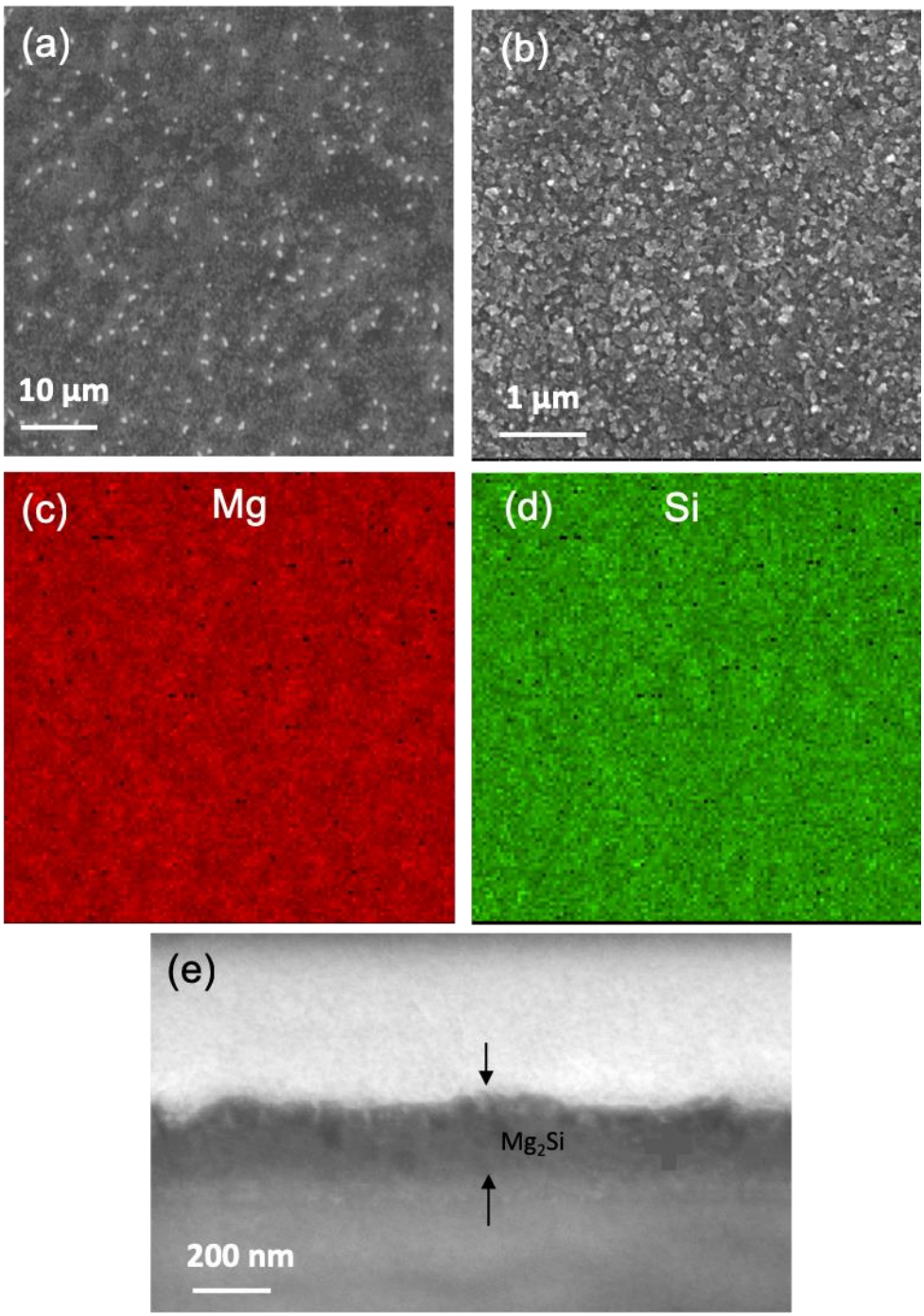

Figure 1.16. (a)(b) Top-down SE image, elemental mapping of (c) Mg, (d) Si, (e) cross-sectional SE image of a thickness-reduced Mg_2Si film.

Figure 1.13 shows a dense, uniform, and crack-free SiO_2 film prepared by spin coating a silica sol-gel at a higher spin speed (5000 rpm) and sintering in air at 700 ˚C for 0.5 h. The thickness revealed from the cross-sectional SE image was 99 ± 2 nm. After magnesiothermic reduction of

the SiO_2 film, the presence of the cubic MgO crystals on the surface of the MgO/Si film (Figure 1.14) was consistent with the theory that the compression stress can be released by MgO migration to the top of the film [37]. The cross-sectional SE image of a MgO/Si film (Figure 1.14(f)) indicated a dense and uniform film with a thickness of 133 ± 4 nm. For the Si film, nano-sized pores can be seen in Figure 1.15(d) after MgO was selectively removed from the MgO/Si film. The porous Si film was then exposed to Mg vapor at 600 ˚C for 2 h to generate a Mg_2Si film. Figure 1.16 shows that the final Mg_2Si film was crack-free, dense, and the phase distribution was uniform over the film according to the EDS maps of Mg and Si. The thickness evolution throughout the conversion steps is summarized in Table 1-3. The "Theoretical Volume Expansion" column values were calculated based on the molar volumes of the species involved in each conversion reaction, and "Film Thicknesses" values were obtained by measuring the thickness from the cross-sectional SE images. For the thickness measurement on each film, 10 different locations on the cross section of the film were measured and averaged. The ranges indicated are 95 % confidence intervals. According to the measurements, the increase of the film thickness from SiO_2 to 2MgO/Si step, and from 2MgO/Si to Mg_2Si, were consistent with the theoretical calculated volume expansion during these two steps. In addition, since the molar volume of Mg_2Si (38.5 cc/mol) is slightly larger than that of 2MgO/Si (34.7 cc/mol), the pores generated during dissolution can be fully filled in to form dense Mg_2Si and residual Si can be present if the volume doesn't expand. However, according to the thickness values measured on SE cross-sectional images after each reaction, the thickness increase was consistent with the theoretical molar volume expansion after Mg_2Si conversion stage. Therefore, the pores generated after acid dissolution were filled and Si was fully converted into Mg_2Si, indicated by the increase of the thickness.

Table 1-3. Theoretical volume change and measured film thicknesses after each conversion step (for thinner films spin coated at 5000 rpm).

Material	Molar Volume (cc/mol)	Theoretical Volume Expansion (%)	Film Thickness (nm)	Thickness Expansion (%)
SiO_2	~ 25.0 – 27.4	N/A	99 ± 2	N/A
2MgO/Si	34.6	26.3 – 38.4	133 ± 4	27.7 – 41.2
Mg_2Si	38.5	40.5 – 54.0	154 ± 8	44.6 – 67.0

Overall, it can be concluded that the volume expansion induced compressive stress from converting SiO_2 to Mg_2Si film was released by film growth along the thickness direction. By reducing the initial SiO_2 film thickness to 99 ± 2 nm, the film quality was significantly improved in terms of uniformity and density, especially for the Si to Mg_2Si conversion step. The final Mg_2Si film was uniform in thickness, dense, and free of cracks.

Furthermore, the surface roughness of the thinner thin films was also evaluated and compared to reveal the nanostructure evolution during the conversion steps. AFM scans were conducted on a 10 µm x 10 µm surface area at each conversion stage for the thinner films, with a scan rate of 0.5 Hz. The roughness values (R_a) obtained from AFM measurements of SiO_2, MgO/Si, porous Si, and Mg_2Si films were 0.5 nm, 4.2 nm, 7.5 nm, and 20.2 nm, respectively. Although the roughness increased to 20.2 nm for the final Mg_2Si film, probably due to grain coarsening, this Ra value was still significantly smaller than the thickness of the Mg_2Si film (154 ± 8 nm).

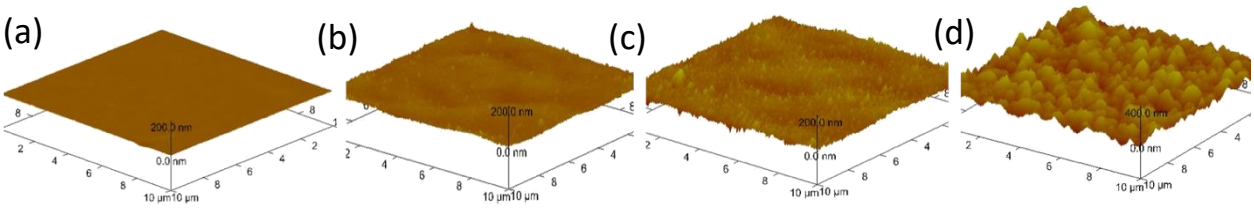

Figure 1.17. AFM 3-D scanning images of the thickness-reduced (a) SiO_2, (b) MgO/Si, (c) porous Si, and (d) Mg_2Si films on sapphire substrates.

1.3.4 Refractive Indices of SiO_2, MgO/Si and Mg_2Si Films from Ellipsometry Results

This work has developed a processing approach to fabricate high refractive index thin films converted from low refractive index films. Refractive index data was collected from ellipsometry measurements in the 500-1100 nm wavelength range. Since there is no optical data for MgO/Si and Mg_2Si films made with this sol-gel coating and chemical conversion method, it's important to know the refractive indices of such films to evaluate the optical behavior of such thin films.

The ellipsometry measurements were conducted for the thin films prepared by spin coating the silica sol-gel solution at 3000 rpm, followed by chemical conversion into Mg_2Si films. The transmittance measurement for each film was shown in Figure 1.18(a). The SiO_2 curve matched well with curves from the literature (within ± 0.01) when applying the model of a bilayer film with

sapphire as the substrate and silica as the top layer, using a Sellmeier dispersion relation [34]. An effective medium approximation (EMA) modelling assuming 65.1 vol % MgO and 34.9 vol % Si in the composite layer was applied, which agreed well with the expected values of molar volumes in MgO/Si thin film (65.1 vol % MgO and 34.9 vol % Si). Other parameters were also applied to modelling, including film thickness and roughness. This modelling analysis was done programmatically in the ellipsometry instrument software. The modelling yielded a dispersion curve intermediate of refractive index values between pure MgO and Si, as shown in Figure 1.18 (b). The ellipsometry measured refractive index value of the MgO/Si film was 16.7 % less than the calculated value based on 65.1 vol% MgO and 34.9 % Si composition. In addition, the refractive index values of the MgO/Si film were higher than those of the SiO_2 film.

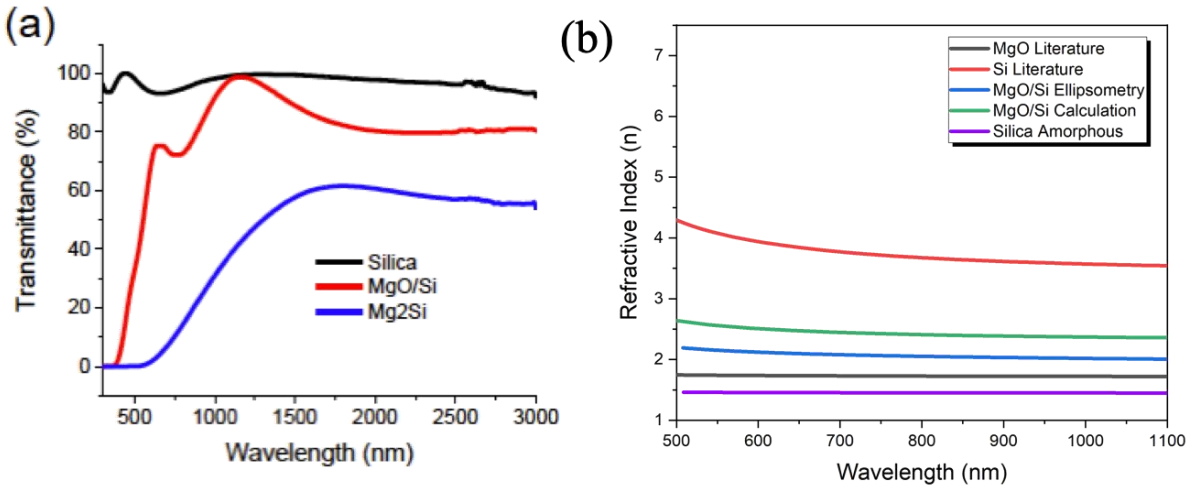

Figure 1.18. Plot of (a) transmittance spectra for thin films of silica, MgO/Si, and Mg_2Si. (b) dispersion curves over 550 -1100 nm for MgO and Si from literature[3, 53], MgO/Si from ellipsometry measurements. (Data acquired by Taylor Allen, Georgia Tech).

Measurement spectra on Mg_2Si films didn't fit reliably by any reasonable model (i.e., EMA, graded index, multilayer). One possible reason was that this mismatch was caused by significant surface roughness and porosity compared to other film compositions. As described in a previous section in this chapter, thinner films were successfully prepared and they exhibited better film uniformity, lower roughness, and they were free of cracks. Unfortunately, ellipsometry on these thinner films were not conducted due to the non-availability of our collaborators and equipment. More investigations on the optical properties of the thinner films are worth exploring in the future.

1.3.5 Light-focusing Measurement on FIB Milled Patterns on Thin Films

Mg_2Si thin films prepared via the approach developed in this study may be patterned to allow for controlled light focusing. Because Mg_2Si possesses a very high refractive index of 3.74 at 10 μm [3], it should exhibit enhanced interaction with light in the infrared (IR) range. Bio-inorganic structures have been found to exhibit impressive control of light. For example, the valves of *Conscinodiscus wailesii* diatoms, which are decorated with a quasi-regular hexagonal pattern of pores, have been found to exhibit wavelength-selective optical transmission and diffraction [54]. The pore distribution on the valve has also enabled these structures to act as micro-lenses. When a red laser beam of 100 μm diameter was transmitted through these valves, the light was focused to a diameter of < 10 μm [55]. Such lensless light focusing was attributed to the bio-derived valve photonic structure. Furthermore, synthetic pore-patterned films may also be used to manipulate light. For example, Vogel pore patterns have been fabricated using different methods for light-focusing application [56–58]. By forming these patterns on high refractive index thin films, such light-focusing behavior can be extended from the visible range to the IR range, which can be used to improve energy harvesting of solar IR radiation. Besides, the optical pore patterns are highly tailorable. By changing the pore patterns, different focusing distance can be obtained. This can be easily achieved during focused-ion beam patterning of the pores in the thin film. Synthetic pore patterns developed by Taylor Allen from Georgia Tech were imprinted on the prepared thin films using focused-ion beam milling to evaluate the effects of the refractive index on the light-focusing behavior of such patterns.

A standardized hole pattern with known dimensions was FIB-milled on SiO_2 and MgO/Si films (prepared by initially spin coating the silica sol-gel solution at 3000 rpm). By starting with a standardized pattern, a direct relationship between a change in index and the focusing distance with respect to wavelength could be obtained.

A synthetic pore pattern was successfully FIB-milled into the thin films. The hole array was constructed by placing 2 μm holes at 8 evenly spaced points (i.e., every $\pi/8$ radians) along the perimeter of three concentric circles of radii 4.5, 8.5 and 13 μm (Figure 1.19(a)). These patterns were measured using the far-field imaging method. Plots of the change in focal distance with wavelength (Figure 1.19(f)) indicated that the focal distances from patterned MgO/Si film were 34 % greater than those of the SiO_2 film on average. The increase in the refractive index from SiO_2

to MgO/Si was 35 % obtained from ellipsometry measurements. This trend suggested that the change of focal distance was correlated to the refractive index change.

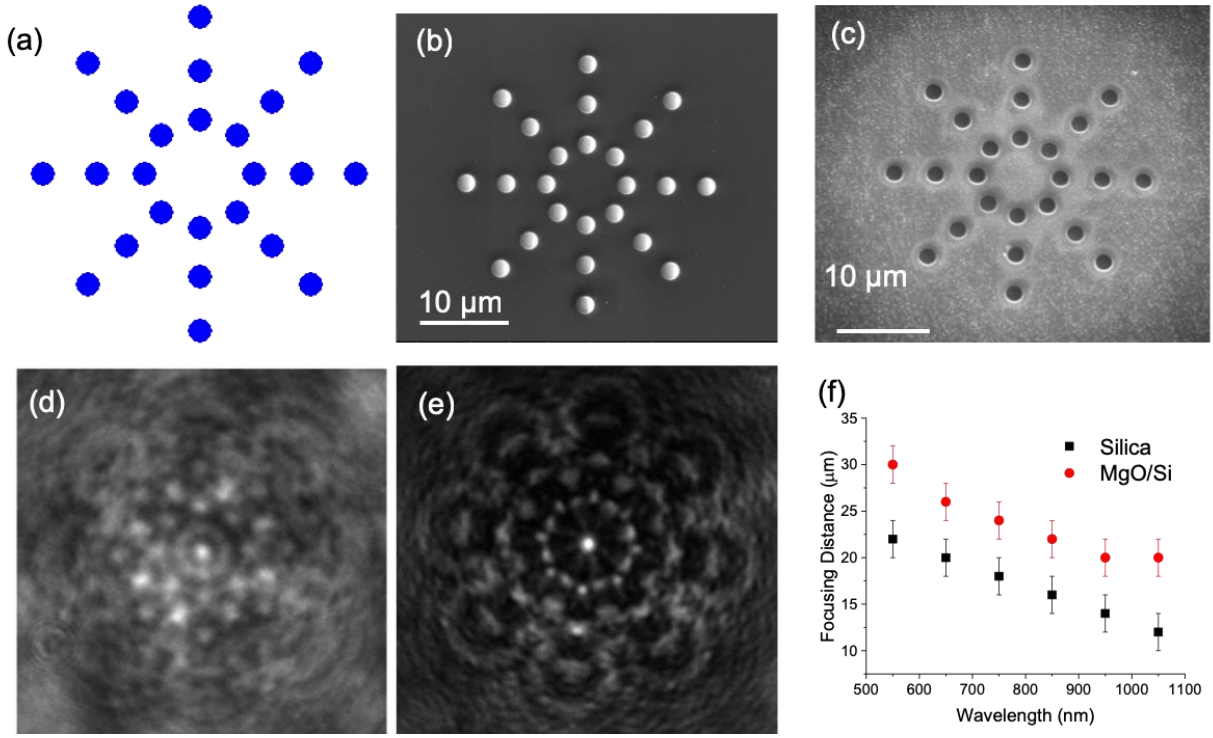

Figure 1.19. (a) Image of standardized pattern generated by MATLAB. (b) SE image of a FIB milled standardized pattern on a SiO_2 film. (c) SE image of a FIB milled standardized pattern on a MgO/Si film. (d)Far filed image of SiO_2 interference pattern at 22 μm, λ = 550 nm; and (e) Far field image of MgO/Si standard pattern interference at 30 μm, λ = 550 nm. (f) Focusing trend of the same standard pattern in SiO_2 and MgO/Si films. (Measurement and data acquisition in (d), (e) and (f) were obtained by Taylor Allen, Georgia Tech).

A light-focusing 500-hole Vogel pattern [57] was FIB-milled on the thin Mg_2Si film, with the ion beam sourcing operating at 30 keV and 3 nA. The hole size was 1.5 μm, and the diameter of the entire pattern was 100 μm. Figure 1.20(c) revealed a clear pattern with distinguished hole edges on the Mg_2Si thin film after ion-beam milling.

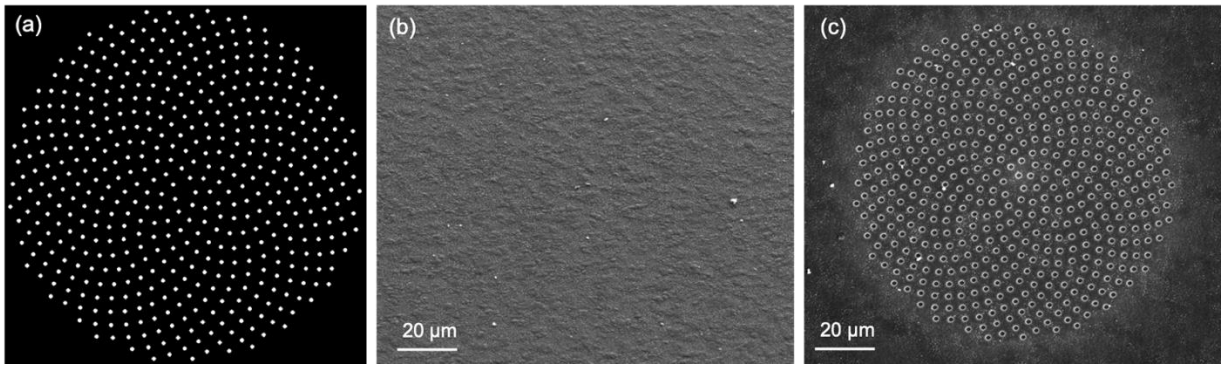

Figure 1.20. (a) A 500-hole Vogel pattern generated using MATLAB. (b) SE image of the Mg_2Si film surface before ion-beam patterning. (c) SE image of the FIB-milled Vogel pattern on the Mg_2Si film.

A diatommimetic pattern was also FIB-milled on a thin SiO_2 film, and a MgO/Si film after magnesiothermic reduction of a SiO_2 film. The diatommimetic pattern was adopted from a *Coscinodiscus wailesii* diatom frustule which possessed light-focusing behavior [55]. The FIB-milled patterns replicated the biogenic diatom structure well and light-focusing optical performance of such samples is worth pursuing in the future.

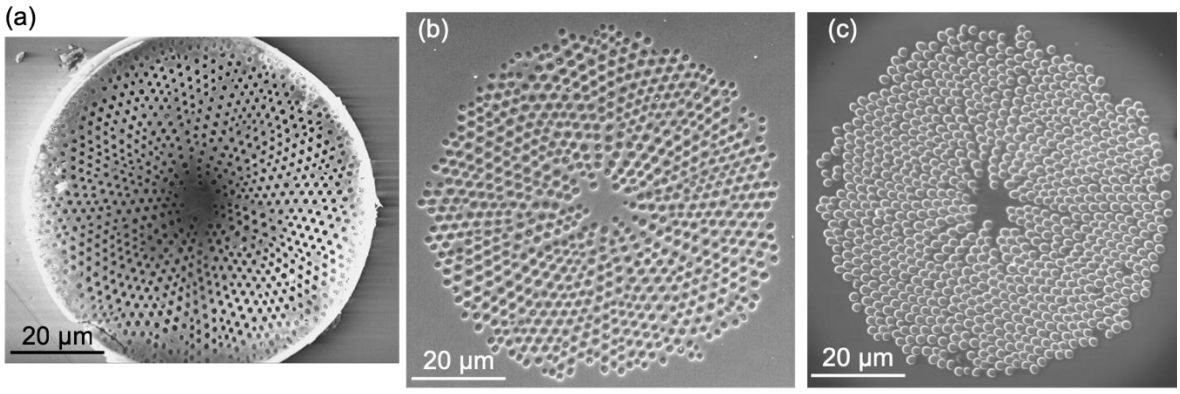

Figure 1.21. (a) SE image of a *Coscinodiscus wailesii* diatom frustule. (b)(c) SE images of FIB milled diatommimetic patterns on a SiO_2 film, and a MgO/Si film, respectively.

1.4 Conclusions

In conclusion, a new alternative method for fabricating thin, dense, and crack-free Mg_2Si films has been successfully developed, for the first time, by using sol-gel spin coating and reactive chemical conversion. First, a dense and uniform SiO_2 thin film was prepared by spin coating a methylcellulose-bearing silica sol-gel solution on a sapphire substrate, followed by pyrolysis in

the air. Then a modified magnesiothermic reduction process using Mg_2Si as a Mg vapor source was applied to convert the SiO_2 film to a MgO/Si film. After dissolving MgO using an acid solution, the porous Si film was reacted with Mg vapor to form a Mg_2Si film. This method could be easily scaled up and is relatively cost-effective, compared to other line-of-sight and/or vacuum deposition methods (e.g., ion beam sputtering, pulsed laser deposition).

Besides thin films, sol-gel processes have been also widely used to fabricate photonic materials in various shapes, such as fibers [59], monoliths [60], and waveguides [61] for optical devices. Our proposed methodology also applies for converting sol-gel silica into magnesium silicide in such varied configurations with excellent shape preservation for a broader variety of applications in optics, solar cells, thermoelectric devices, and anode materials for lithium ion batteries.

The refractive indices of the thin films at each stage of chemical conversion were measured using ellipsometry. The refractive index increased upon transformation of SiO_2 to MgO/Si. In addition, the measured refractive index of the MgO/Si thin film was in good agreement with the estimated value based on a crude rule-of-mixtures (65.1 vol % MgO, 34.9 vol % Si) from the refractive indices from MgO and Si. Artificial light-focusing patterns were printed on the prepared thin films using focused ion beam milling, and the light-concentration behaviours were measured by our collaborator at Georgia Tech. The results showed a clear trend of increased focusing distance as the refractive index of the film increased, confirming the optical behaviour dependence on the refractive index of the material. In the future work, obtaining the optical properties of the thinner films (more uniform, dense, and crack-free) would be valuable to pursue.

2. KINETIC MECHANISM OF MAGNESIUM SILICIDE FORMATION VIA Mg-Si GAS-SOLID REACTION

This chapter has been published and fully cited in this dissertation: Li, J., Hwang, S., Itskos, G., Sandhage K., Kinetic mechanism of conformal magnesium silicide (Mg_2Si) film formation via reaction of Si single crystals with Mg vapor, *Journal of Materials Science*, 2020, Copyright © Springer Nature.

2.1 Introduction

The thermal, electrical, optical, and chemical properties of magnesium silicide (Mg_2Si) have led to consideration of this semiconducting material for use in optoelectronic [4–7], thermoelectric [7–11], and superconducting [12] devices, and as a corrosion-resistant and wear-resistant coating [62]. The relative earth-abundant nature and non-toxicity of the constituent elements of this silicide are additional characteristics that can make Mg_2Si-based materials attractive as replacements for less environmentally-benign engineering materials [13, 14] (e.g., to replace tellurium-bearing and lead-bearing compounds used in thermoelectric energy conversion processes).

A variety of synthesis techniques have been examined for the fabrication of Mg_2Si films for device applications, including ion beam sputtering [22–24], pulse laser deposition [12, 21, 25], molecular beam epitaxy [63], solid-state growth [13, 15–17], and gas/solid reaction [18, 19, 64]. For the latter approach, conformal Mg_2Si layers have been generated on Si substrates via direct reaction with Mg vapor at modest temperatures (note: Mg_2Si is the only stable compound that can form by such reaction at ambient pressure, and the solid solubility of Mg_2Si in Si is negligible [46]). Such conformal gas/solid reaction processing enables patterned (conformal) Mg_2Si films to be generated on patterned (microfabricated) Si substrates at ambient pressure without the need for line-of-sight deposition or vacuum equipment.

To allow for control of the Mg_2Si film thickness for device fabrication, the rate of reaction of Mg vapor with solid Si needs to be understood. Significant complications associated with investigating such reactions include the tendencies of Mg vapor and solid Mg_2Si to oxidize (even at low oxygen partial pressures) and of Mg_2Si to lose Mg via selective evaporation at modest

temperatures [13, 15, 63, 65–68]. The purpose of this chapter is to determine the kinetic mechanism (rate-limiting step and associated rate law) of the growth of conformal Mg_2Si layers generated by the reaction of planar Si substrates with Mg vapor under well-controlled, non-oxidizing conditions.

2.2 Possible Rate-limiting Steps

2.2.1 Solid State Diffusion of Si or Mg Atoms

For Si or Mg atoms diffusing across the Mg_2Si layer, there are two possible diffusion pathways: the Mg_2Si lattice and grain boundaries (assuming that the Mg_2Si layer is dense and crack-free). In this case, the solid state diffusion process would involve either Si atoms diffusing outward or Mg atoms diffusing inward or both.

Si or Mg Diffusion through the Mg_2Si Lattice

Assume the Mg_2Si layer is planar, uniform in thickness, compact and that crack free, and the Mg_2Si layer growth is proportional to the flux of Si or Mg atoms across the reaction zone, which can be expressed by the equation below:

$$\frac{d\Delta x}{dt} = constant \times J \qquad \text{Eqn. 2.1}$$

Applying Fick's first law:

$$J = -D_{lattice} \frac{dc}{dx} \qquad \text{Eqn. 2.2}$$

Combining these two equations, we obtain:

$$\frac{d\Delta x}{dt} = constant \times D_{lattice} \frac{\Delta c}{\Delta x} \qquad \text{Eqn. 2.3}$$

where J is the flux of Si or Mg atoms across the reacted zone, D is the diffusivity of Si or Mg, and dc is the change of concentration, which is constant since local equilibrium is reached at the interfaces (chemical reactions happen quickly).

Eqn. 2.3 can be written as:

$$\frac{d\Delta x}{dt} = k_p \frac{1}{\Delta x} \quad \text{Eqn. 2.4}$$

Integrating both sides:

$$\Delta x^2 = k_p t \quad \text{Eqn. 2.5}$$

Hence, if the rate limiting step is the solid state diffusion through the lattice, the Mg_2Si layer growth will follow a parabolic rate law. A plot of log(thickness) vs. log(time) would yield a straight line with a slope close to 0.5.

Si or Mg Diffusion along Mg_2Si Grain Boundaries

If the rate limiting step is controlled by the solid state diffusion through grain boundary, two cases should be considered: i) absence of grain growth; ii) presence of grain growth.

i): Perrow *et al* studied the contributions of both lattice and grain boundary diffusion through an oxide during oxide layer growth upon oxidation of a metal [69]. The assumptions and calculations of grain boundary section in their study can be applied to the Si or Mg atoms diffusing through grain boundaries in the Mg_2Si layer. The effective diffusion coefficient can be defined as follows:

$$D_{eff} = D_{GB} f \quad \text{Eqn. 2.6}$$

where D_{GB} is the diffusion coefficient for transport along grain boundaries, and f is the area fraction of grain boundaries.

Assuming that the shape of grains is cubic, the grain edge length is G, and the width of an average grain boundary is δ (G>> δ), then $f \approx \frac{2\delta}{G}$ [69]. Other shapes of grain can also be assumed and f would be expressed differently.

If there is no presence of grain growth, which means G is a constant, then a parabolic layer growth should be observed if grain boundary diffusion in the Mg_2Si layer is the rate-limiting step.

ii): For the case when grains grow, Perrow *et al* observed that the average G of NiO grains increased parabolically with time at 600˚C [69]. Here a more general grain growth rate is presented as:

$$G^n - G_0^n = Kt \quad \text{Eqn. 2.7}$$

where K is a time-independent constant, and n is the power of grain growth rate.

Combining with Eqn. 2.6,

$$D_{eff} = D_{GB}\frac{2\delta}{(Kt + G_0^n)^{\frac{1}{n}}} \qquad \text{Eqn. 2.8}$$

Assuming the growth rate of Mg_2Si layer is proportional to the Si or Mg atom flux through the reaction zone, then:

$$\frac{d\Delta x}{dt} = -constant\ D_{eff}\frac{dc}{dx} \qquad \text{Eqn. 2.9}$$

or,

$$\frac{d\Delta x}{dt} = -constant\ D_{GB}\frac{2\delta}{(Kt + G_0^n)^{\frac{1}{n}}}\frac{\Delta c}{\Delta x} \qquad \text{Eqn. 2.10}$$

Integrating both sides and combining all the constants:

$$\Delta x^2 = k_{p,GB}(Kt + G_o^n)^{1-\frac{1}{n}} \qquad \text{Eqn. 2.11}$$

Therefore, if the grains grow and diffusion along grain boundaries is the rate-limiting step, then a parabolic growth of Mg_2Si would no longer be obtained. The Mg_2Si growth rate will depend on the grain growth rate in this case.

2.2.2 Mg Diffusion through the Bulk Gas Phase

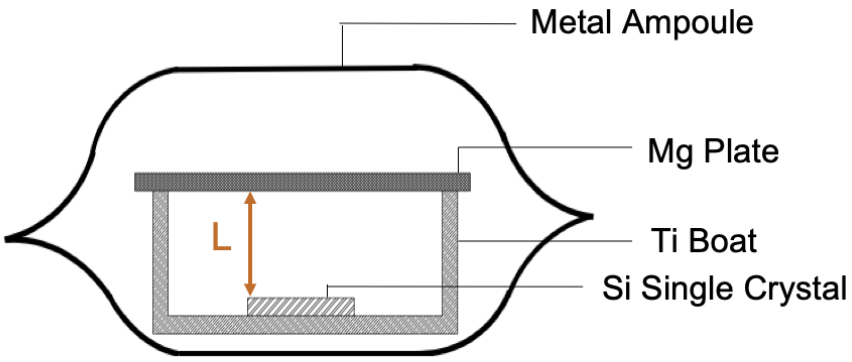

Figure 2.1. Schematic illustration of the reaction set-up for the Mg-Si Gas-Solid reaction.

As shown in Figure 2.1, the Mg foil was placed on top of the Si wafer to conduct the Mg-Si Gas-Solid reaction. At elevated temperature, Mg foil generates Mg vapor, which transports to the surface of the Si wafer underneath and react to form Mg_2Si. A possible rate limiting step would be Mg vapor diffusion through Mg bulk gas phase. In this case, the solid state diffusion through the Mg_2Si product layer and chemical reaction rates at the interfaces are relatively fast. Therefore, the concentration difference between the Mg(g)/Mg_2Si interface and Mg foil surface is constant. Assume the Mg_2Si layer growth rate is proportional to the Mg gas flux, the growth rate can be expressed as:

$$\frac{d\Delta x}{dt} = constant \times J \qquad \text{Eqn. 2.12}$$

Appling the Fick's first law:

$$J = -D\frac{\Delta c_{Mg}}{L} \qquad \text{Eqn. 2.13}$$

where L is the distance between Mg foil and Si substrate. Since Mg_2Si thickness Δx is much smaller than the distance, Δx can be ignored here. Also, flux is considered constant with the change of time.

Therefore,

$$\frac{d\Delta x}{dt} = \frac{k_p}{L} \qquad \text{Eqn. 2.14}$$

$$\Delta x = \frac{k_p}{L}t \qquad \text{Eqn. 2.15}$$

Eqn. 2.15 indicates a linear relation between layer thickness Δx and reaction time. In addition, Δx is also reversely proportional to L, which means when reaction time is constant, the Mg_2Si layer thickness will change linearly with 1/L.

2.2.3 Chemical Reaction

There are two interfaces where chemical reactions can happen: i) Mg(g)/Mg_2Si interface and ii) Mg_2Si/Si(s) interface. For a chemical reaction controlled reaction, the film growth rate is proportional to the appropriate interfacial area [70]. Since the interfacial area in this study is

constant during the gas-solid reaction, the reaction rate $\frac{d\Delta x}{dt}$ can be expressed as (assuming steady state flux):

$$\frac{d\Delta x}{dt} = k[A]^n \qquad \text{Eqn. 2.16}$$

where k is the rate constant, n is the order of the reaction, and [A] is the concentration of a reactant, which is constant with time.

Integrating Eqn. 2.16, one can obtain:

$$\int_0^{\Delta x} d\Delta x = \int_0^t k[A]^n dt \qquad \text{Eqn. 2.17}$$

$$\Delta x = k[A]^n t \qquad \text{Eqn. 2.18}$$

Therefore, if the chemical reaction is the rate limiting step, Mg_2Si layer will grow linearly with the reaction time, as indicated in Eqn. 2.18.

2.3 Experimental Procedures

2.3.1 Reaction of Single Crystal Si Substrates with Mg Vapor

Polished (average surface roughness, R_a < 0.5 nm) single crystal silicon wafers (0.4 mm thickness, 76 mm dia.) of <100>, <110>, and <111> orientations were obtained from a commercial source (UniversityWafer, Boston, MA, USA). For each reaction experiment, a plate-shaped, 1 cm x 1 cm x 0.4 mm specimen was cut from a given single crystal silicon wafer and was then placed in a titanium boat (1.5 cm width x 1.5 cm length x 0.5-0.7 mm height, > 99.9% purity Ti, MTI Corporation, Richmond, CA, USA). A magnesium plate (1.5 cm x 3.5 cm x 0.5 mm, 99.95% purity, Solution Materials, Santa Clara, CA, USA) was used as the magnesium vapor source. To evaluate the influence of the steady-state flux of magnesium vapor on the gas/solid reaction kinetics, the distance between the magnesium plate and the silicon plate was varied from 0.1 cm to 0.7 cm. For the shortest distance of 0.1 cm, a porous mesh spacer (304 stainless steel, 0.1 cm thick with 6.4 mm x 6.4 mm square holes, McMaster-Carr, Chicago, IL, USA) was placed between the magnesium and silicon plates. For distances of 0.5 cm and 0.7 cm, the magnesium plate was placed

as a lid on 0.5 cm tall and 0.7 cm tall titanium crucibles, respectively, containing the silicon plates (the Si plates were oriented horizontally at the bottom of the crucibles). The reactant assembly was then sealed in a metal ampoule (304 stainless steel, 2.5 cm internal diameter, McMaster-Carr) via welding within a dry Ar atmosphere glovebox ($\leq$ 0.5 ppm O_2, $\leq$ 0.8 ppm H_2O) so as to avoid oxidation during the subsequent silicide formation at 600°C. The Mg:Si molar ratio sealed within the ampoules was > 2.9:1. The metal ampoules were placed inside a horizontal mullite tube furnace (Sentro-Tech Corp., Strongsville, OH, USA) that was then evacuated and backfilled with argon. The specimen-bearing ampoules were heated to 600˚C and held at this temperature for 2 h to 10 h. After cooling to room temperature, the ampoules were removed from the furnace and cut open to retrieve the reacted samples. Sufficient Mg and Si were placed within the ampoule that excess unreacted Mg and Si were retained even at the longest reaction time examined (10 h); that is, the reaction process was not limited by the available Mg and Si reactants.

2.3.2 Characterization of Mg_2Si Films

Backscattered electron (BSE) images of fractured cross-sections of reaction-formed Mg_2Si films on Si single crystal plates were obtained with a scanning electron microscope (Phenom XL, Phenom-World BV, The Netherlands). The average thickness of a given Mg_2Si film, generated by the reaction of Mg vapor with a <100>, <110>, or <111> oriented single crystal Si plate for a given time at 600°C, was determined using measurements obtained at 15 locations over a 1 cm lateral span of a fractured Mg_2Si/Si specimen cross-section. X-ray diffraction (XRD) analyses (Bruker D2 Phaser, Bruker AXS GmbH, Germany) of the reacted specimens were conducted over a 2θ range of 20˚to 60˚ with a step size of 0.018° and a dwell time of 0.2 sec $step^{-1}$.

The mass changes of the Si single crystal plate specimens due to reaction with Mg(g) were obtained with an electronic microbalance (ME36S, 0.001 mg resolution, Sartorius, Germany). Such mass change measurements were also used to calculate the average thicknesses of the associated reaction-formed Mg_2Si films by use of the following equation:

$$h = \frac{\frac{\Delta m}{M_{Mg}} \times \frac{1}{2} \times M_{Mg_2Si}}{\rho_{Mg_2Si}\, A} \qquad \text{Eqn. 2.19}$$

where h is the average film thickness; Δm is the mass gain; M_{Mg} and M_{Mg_2Si} are the atomic mass of Mg and molecular mass of Mg_2Si, respectively; ρ_{Mg_2Si} is the density of Mg_2Si (1.99 g cm^{-3}) [50]; and A is the exposed specimen surface area.

2.3.3 Inert Marker Experiments

Owing to chemical compatibility with solid silicon and magnesium vapor at 600˚C, magnesia (MgO) particles were used as inert markers in this work [40]. A mixture of 0.05 wt% MgO powder (99.9% purity, 1 μm average particle size, Inframat Advanced Materials, Amherst, NY, USA) in hexane was prepared using ultrasonication for 10 min. A micropipette was used to deposit 200 μl of this mixture onto the surface of a given Si single crystal plate. After hexane evaporation, the MgO-bearing Si plates were exposed to Mg(g) at 600˚C for 2 h. The location of the MgO particles after such exposure was determined by examination of the external surfaces and fractured cross-sections of the reacted specimens using electron microscopy (BSE images) with energy-dispersive X-ray analyses (to obtain elemental maps of Mg, Si, and O).

2.4 Results and Discussion

2.4.1 Phase Content and Microstructure of Mg_2Si Films Formed on Si Single Crystal Plates

An XRD pattern obtained from the surface of a <100> oriented Si single crystal plate after reaction with Mg vapor at 600ºC for 10 h is provided in Figure 2.2. The only diffraction peaks detected were those associated with Mg_2Si from the product film. Diffraction peaks associated with the oxidation of magnesium silicide or silica (i.e., peaks for magnesia, silica, or magnesium silicate phases) were not detected. XRD patterns obtained from <100> oriented Si single crystal plates for other reaction times, and from the surfaces of <110> and <111> oriented Si single crystal plates after reaction with Mg(g) at 600ºC for 8 h, yielded similar results (i.e., diffraction peaks were detected for Mg_2Si but not for oxide phases).

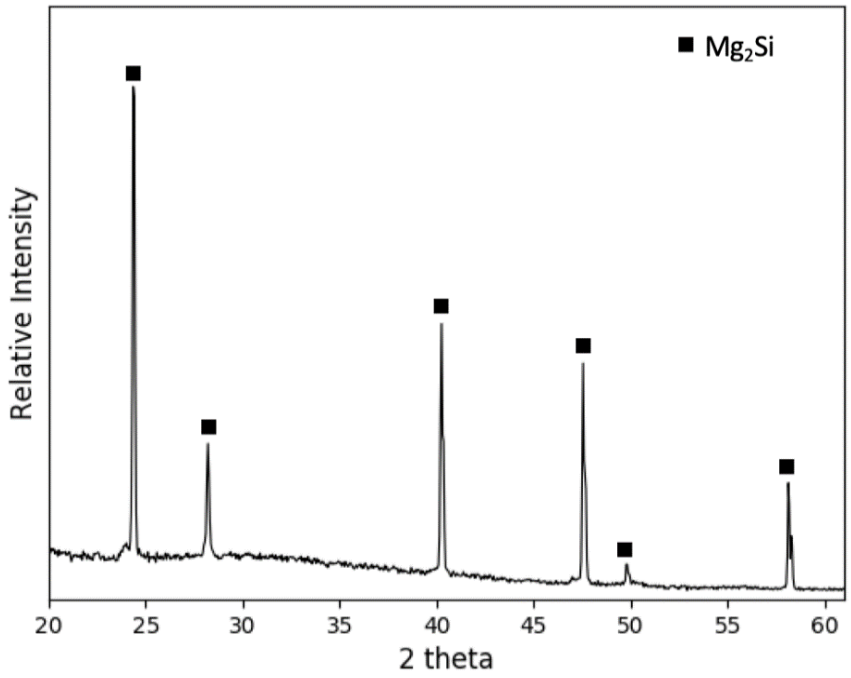

Figure 2.2. XRD pattern obtained from the surface of a <100> oriented Si single crystal plate after reaction with Mg vapor at 600°C for 10 h (with a Mg vapor diffusion distance of 0.5 cm)

The formation of Mg_2Si via the reaction of Mg vapor with solid Si can be described by the following reaction:

$$2Mg(g) + Si(s) \rightarrow Mg_2Si(s) \qquad \text{(Reaction 2.1)}$$

The equilibrium vapor pressure of magnesium associated with this reaction at 600°C (using a pure solid reference state for Si and a solid stoichiometric reference state for Mg_2Si, and assuming that Mg vapor behaves as an ideal gas) is 1.1 x 10^{-5} atm [40]. The vapor pressure of Mg(g) in equilibrium with pure solid Mg at 600 °C (using a pure solid reference state for Mg) is 1.5 x 10^{-3} atm [40]; that is, the magnesium partial pressure generated from solid Mg sealed within the metal ampoule at 600 °C was more than 100 times that calculated for reaction (Reaction 2.1) to proceed spontaneously to the right.

A non-trivial challenge in conducting experiments to evaluate the kinetics of Mg_2Si formation, via the reaction of Mg vapor with Si, is avoidance of oxidation during such silicide formation [13, 15, 63, 65–68]. Consider the oxidation of magnesium vapor and magnesium silicide via the following reactions:

$$2Mg(s) + O_2\ (g) = 2MgO(s) \qquad \text{(Reaction 2.2)}$$

$$Mg_2Si(s) + O_2(g) = 2MgO(s) + Si\,(s) \qquad \text{(Reaction 2.3)}$$

The calculated equilibrium oxygen partial pressures associated with reactions (Reaction 2.2) and (Reaction 2.3) (using pure stoichiometric solid reference states for MgO and Mg_2Si, a pure solid reference state for Si, and assuming that oxygen behaves as an ideal gas) at 600°C are extremely low (i.e., 1.8×10^{-65} atm and 3.4×10^{-61} atm, respectively [40, 41]). Hence, the Mg and Si reactants for the present work were sealed within metal ampoules in an Ar atmosphere glove box. Upon heating to 600°C, the excess solid magnesium could react with residual oxygen (present as a contaminant) in the argon within the sealed ampoule to form a small amount of MgO to achieve extremely low oxygen partial pressures (as per reaction (Reaction 2.2)). The remaining heated non-oxidized Mg could generate Mg vapor to react with solid Si via reaction (Reaction 2.1) (note: the MgO formed on solid Mg at 600 °C forms as a porous/cracked product, so that Mg vapor could migrate through such a permeable MgO product and then diffuse to the Si specimen within the ampoule to form Mg_2Si [71–73]). The absence of detectable X-ray diffraction peaks for magnesia, silica, or magnesium silicates on the specimen surfaces after reaction of the Si single crystal plates with Mg vapor (Figure 2.2) indicated that this sealed ampoule approach was an effective means of avoiding the oxidation of Mg vapor and Mg_2Si.

Titanium and 304 stainless steel were selected as the materials for the crucibles and metal ampoules, respectively, owing to the chemical compatibility of magnesium with titanium, iron, and chromium (note: iron and chromium comprise $\geq$85 wt% of 304 stainless steel); that is, magnesium does not form stable compounds with titanium, iron, and chromium at ambient pressure, and magnesium exhibits modest solubility in titanium (< 2 at%) and negligible solubility in iron and chromium, at 600°C [74–77]. While magnesium can undergo reaction with nickel (present at 8-11 wt% in 304 stainless steel), no appreciable reaction was detected between the magnesium vapor and 304 stainless steel within 10 h at 600 °C. (Note: 304 stainless steel was used for the metal ampoules, instead of titanium, owing to the relative ease with which the 304 stainless steel ampoules could be welded shut.)

BSE images of fractured cross sections of <100> oriented Si single crystal plates after reaction with Mg vapor at 600 °C for 2 h and 10 h are shown in Figure 2.3(a) and (b), respectively. Dense, conformal, and continuous Mg_2Si films were observed to have formed on the Si single crystal plates. BSE images obtained from fractured cross-sections of <110> and <111> oriented

Si single crystal plates after reaction with Mg vapor at 600°C for 2-10 h (not shown) also revealed the presence of dense, conformal, and continuous Mg_2Si films.

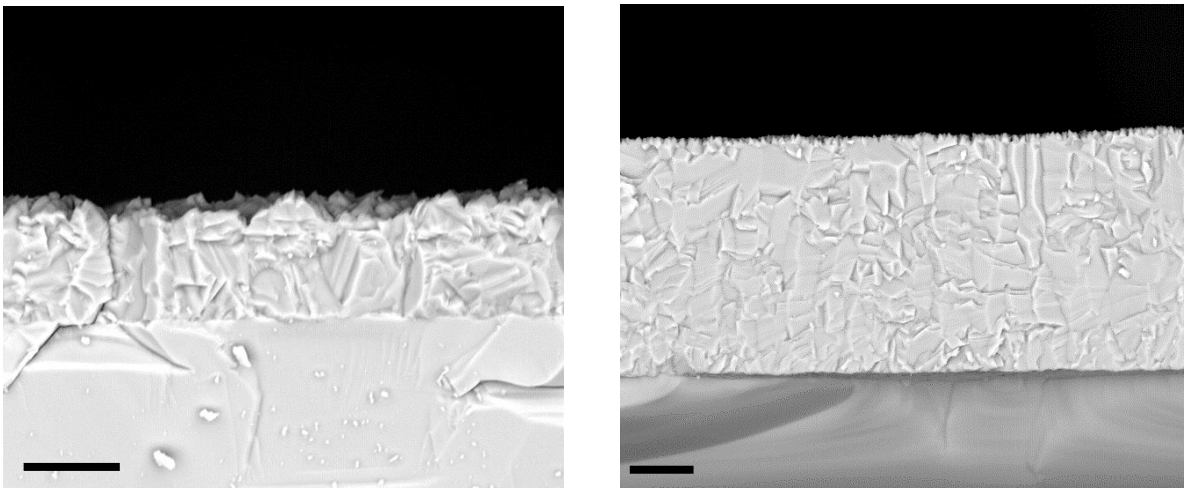

Figure 2.3. BSE images obtained from fractured cross-sections of Mg_2Si films formed on <100> oriented Si single crystal plates after reaction with Mg vapor (with a vapor diffusion distance of 0.5 cm) at 600˚C for: a) 2 h and b) 10 h (bars: 20 μm)

2.4.2 Mg_2Si Formation Kinetics

Values of the average Mg_2Si film thickness (ΔX) obtained from BSE images of fractured cross-sections, and of the specimen mass change per area ($\Delta m/A$), for <100> oriented Si single crystal plates after reaction with Mg(g) at 600°C for 2-10 h are provided in Table 2-1 (for a Mg vapor diffusion distance of 0.5 cm). Values of the average Mg_2Si film thickness obtained from mass change measurements using Eqn. 2.19 are also presented in this table. These calculated film thickness values were in good agreement with the values obtained from direct measurements via scanning electron microscopy of fractured cross-sections.

Table 2-1. Kinetic data for Mg_2Si film thickening via the reaction of <100> oriented Si single crystal plates with Mg vapor at 600 ˚C (with a vapor diffusion distance of 0.5 cm)

Reaction time	Mg_2Si film thickness* (ΔX, SEM)	Mass change/area ($\Delta m/A$)	Mg_2Si film thickness (ΔX, Eqn (E1))
2 h	27.4 $\pm$ 0.7 μm	3.69 mg cm^{-2}	29.3 μm
4 h	50.7 $\pm$ 0.5 μm	6.64 mg cm^{-2}	52.7 μm
6 h	61.5 $\pm$ 0.2 μm	7.53 mg cm^{-2}	59.8 μm
8 h	71.3 $\pm$ 0.8 μm	9.15 mg cm^{-2}	72.6 μm
10 h	76.0 $\pm$ 0.3 μm	9.54 mg cm^{-2}	75.7 μm

(*the $\pm$ range of SEM-derived ΔX values refers to the 95% confidence limit range)

Plots of the logarithm of the thickness of Mg_2Si films (formed on <100> oriented Si single crystal plates) vs. the logarithm of reaction time are shown in Figure 2.4. The film thickness data presented in Table 2-1 were obtained by direct measurements of the Mg_2Si layer thickness from BSE images of fractured specimen cross-sections (such as shown in Figure 2.3). The film thickness data presented in Table 2-1 were obtained from measurements of the mass change per area using Eqn. 2.19. Regression analyses to determine the best fitting straight lines yielded R^2 (coefficient of determination) values of 0.95 and 0.98 for Figure 2.4 (a) and (b), respectively. The slope values of the best fit lines shown in Figure 2.4 (a) and (b) were 0.51 ± 0.07 and 0.54 ± 0.05, respectively, which were consistent with parabolic film thickening kinetics. Given these R^2 and slope values, plots of the Mg_2Si layer thickness vs. the square root of time were constructed and are shown in Figure 2.5 (a) (for Mg_2Si layer thickness obtained from BSE images of fractured cross-sections) and (b) (for Mg_2Si layer thickness obtained from measurements of mass change per area using Eqn. 2.19). Best fit lines with R^2 values of 0.98 and 0.99 are shown in Figure 2.5(a) and (b), respectively. The slopes of these best fit lines were used to calculate the parabolic rate constant, K_p, for Mg_2Si layer thickening according to the following equation:

$$\Delta X = (2K_p t)^{1/2} \qquad \text{Eqn. 2.20}$$

where ΔX is the Mg_2Si film thickness, and t is the reaction time. The K_p values obtained from the slopes of the best fit lines in Figure 2.5(a) and (b) were 8.8×10^{-10} cm^2 s^{-1} and 8.6×10^{-10} cm^2 s^{-1}, respectively. The excellent agreement in these K_P values indicated that the assumptions

involved in the use of Eqn. 2.19 (i.e., that the Mg_2Si films were dense, conformal, and continuous) to calculate the average Mg_2Si film thickness from global mass change measurements were valid.

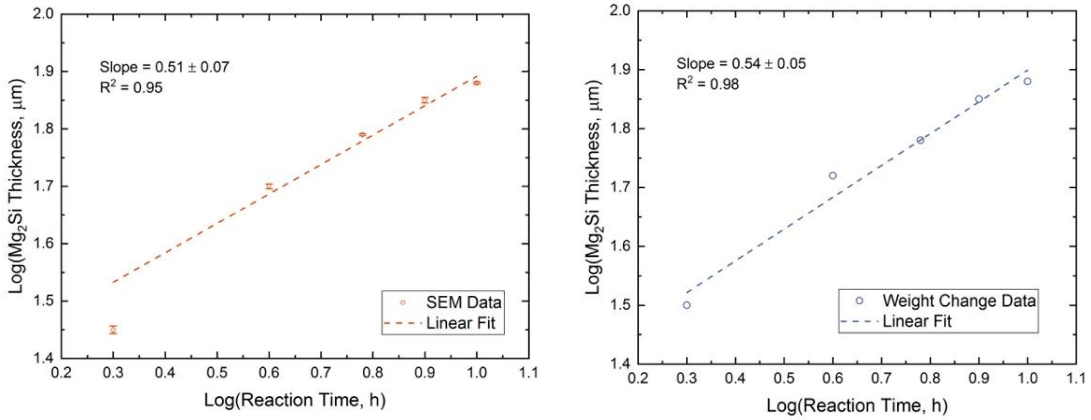

Figure 2.4. Plots of log [Mg_2Si film thickness] as a function of the log[reaction time] of <100> oriented Si single crystal plates with Mg vapor at 600˚C (for a Mg vapor diffusion distance of 0.5 cm), with the film thickness values shown in: a) obtained from scanning electron microscope (BSE) images of fractured specimen cross-sections and b) calculated from mass change per area measurements using Eqn. 2.19.

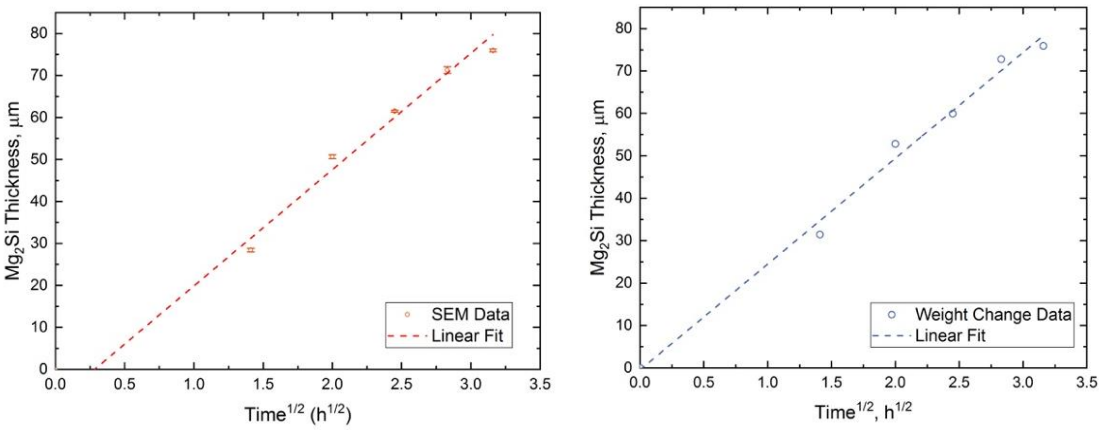

Figure 2.5. Plots of Mg_2Si film thickness as a function of the square root of the time of reaction of Mg(g) with <100> Si substrates at 600˚C (for a Mg vapor diffusion distance of 0.5 cm), with the film thickness values shown in: a) obtained from scanning electron microscope (BSE) images of fractured specimen cross-sections and b) calculated from mass change per area measurements using Eqn. 2.19.

Gordin *et al* [15] recently examined the kinetics of Mg_2Si film formation via solid-state reaction of thin Mg films (deposited by e-beam evaporation) with underlying planar Si single crystal substrates at 280-400 ^oC. These authors found that kinetics of such solid-state Mg_2Si film formation also followed a parabolic rate law. Extrapolation of the K_p value obtained by these authors at 400 ^oC to the 600 ^oC reaction temperature of the present work (using an activation energy of 102.3 $\pm$ 13.5 kJ mol^{-1} reported by Gordin and Sandhage [15]) yielded a K_p value of 1.9 $\pm$ 1.4 x 10^{-10} cm^2 s^{-1}, which was in reasonable agreement (within a factor of 5) with the K_p values obtained in the present work.

To evaluate the influence of the steady-state magnesium vapor flux on the kinetics of Mg_2Si film formation, experiments were conducted by varying the distance between the Mg vapor source (solid Mg) (denoted as "L" in Figure 2.6) and the Si single crystal plates from 0.1 cm to 0.7 cm. If gas-phase diffusion was a rate-limiting step, then such an increase in the magnesium vapor diffusion distance should have resulted in a proportional decrease in the steady-state Mg vapor flux and a decrease in the Mg_2Si film thickness for a given reaction time. However, as shown in Table 2-2, Mg_2Si films of similar thickness had formed on <100> oriented Si single crystal plates, with diffusion distances of 0.1 cm, 0.5 cm, and 0.7 cm, after 8 h of exposure to Mg vapor at 600^oC.

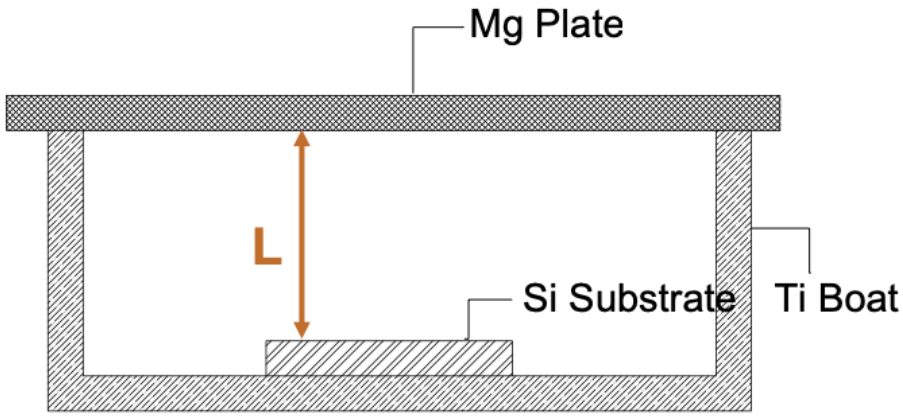

Figure 2.6. Illustration of the experimental set up inside the ampoule for Mg_2Si formation via Mg-Si Gas-Solid reaction at 600 ˚C.

Table 2-2. The effects of the diffusion distance of Mg vapor and of the Si single crystal orientation on the thickness of Mg_2Si films formed via the reaction of Si single crystal plates with Mg vapor at 600 ˚C for 8 h.

Si single crystal orientation	Mg vapor distance	Mg_2Si film thickness (ΔX, SEM)	Mass change/area ($\Delta m/A$)	Mg_2Si film thickness (ΔX, Eqn. 2.19)
<100>	0.1 cm	71.7 ± 0.5 μm	N/A*	N/A*
<100>	0.5 cm	71.3 ± 0.8 μm	9.15 mg cm^{-2}	72.6 μm
<100>	0.7 cm	70.4 ± 0.2 μm	8.79 mg cm^{-2}	69.8 μm
<110>	0.5 cm	69.6 ± 0.5 μm	9.28 mg cm^{-2}	73.6 μm
<111>	0.5 cm	70.1 ± 0.4 μm	9.23 mg cm^{-2}	73.2 μm

(*note: the stainless-steel mesh used to achieve a separation distance of 0.1 cm between the solid Mg vapor source and the Si single crystal plate covered part of the Si plate surface, so a global mass change measurement was not evaluated for this separation distance)

If a chemical reaction at the Si/Mg_2Si interface was a rate-limiting step, then a change in the orientation of the Si single crystal plates could affect the thickening rate of the Mg_2Si films. However, as also shown in Table 2-2, Mg_2Si films of similar thickness had formed on <100>, <110>, and <111> oriented Si single crystal plates after 8 h of exposure to Mg vapor at 600°C (for a vapor diffusion distance of 0.5 cm).

The parabolic kinetics found for the thickening of the Mg_2Si films, and the negligible influences of the Mg vapor diffusion distance and the Si single crystal orientation on the Mg_2Si film thickness, were consistent with solid-state diffusion through the Mg_2Si film as the rate-controlling step.

2.4.3 Inert Marker Experiment

BSE images, and associated elemental maps for oxygen, magnesium, and silicon, of the surface of a <100> oriented Si single crystal plate containing MgO particles as inert markers are shown in Figure 2.7. A dilute distribution of fine MgO particles was present on the Si plate. BSE images, and associated elemental maps for oxygen, magnesium, and silicon, of a fractured cross-section of a <100> oriented Si single crystal plate, containing MgO particles as inert markers, after reaction with Mg(g) at 600°C for 2 h are shown in Figure 2.8. BSE images, and associated elemental maps for oxygen, magnesium, and silicon, of the external surface of this specimen are

shown in Figure 2.9. Figure 2.8 and Figure 2.9 reveal the presence of the inert MgO markers only on the external surface of the product Mg_2Si film.

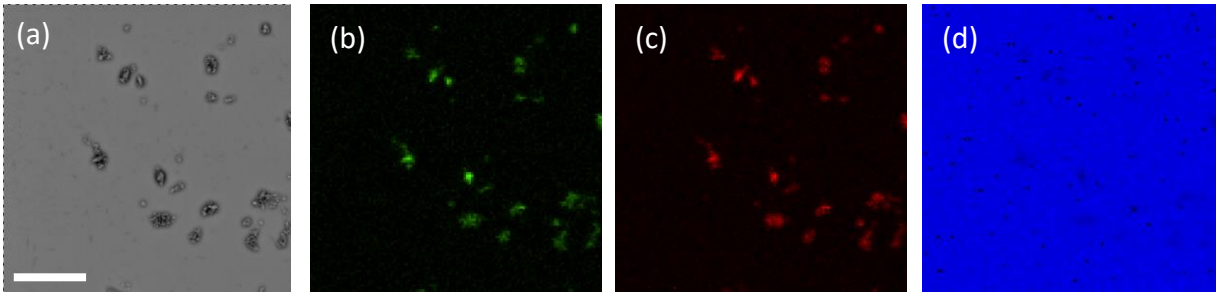

Figure 2.7. **a)** BSE image and associated element maps of **b)** oxygen, **c)** magnesium, and **d)** silicon obtained from the surface of a <100> oriented Si single crystal plate containing MgO particles (inert markers) prior to reaction with Mg vapor (bar: 20 µm).

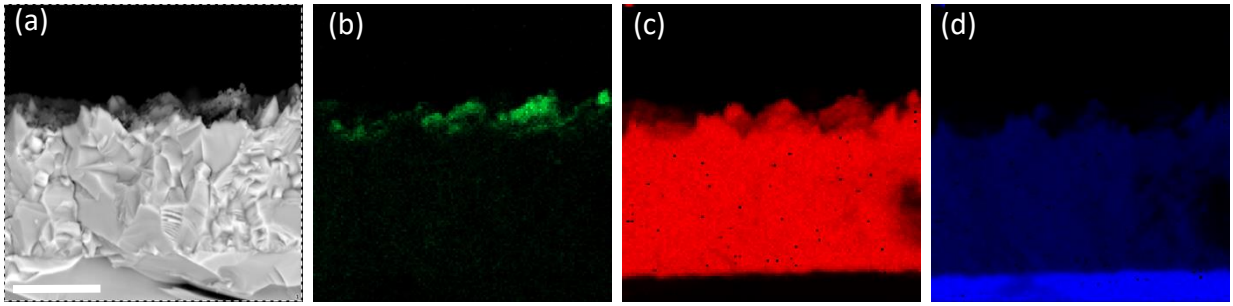

Figure 2.8. a) BSE image and associated element maps of b) oxygen, c) magnesium, and d) silicon obtained from a fractured cross-section of a <100> oriented Si single crystal plate containing MgO particles (inert markers) after reaction with Mg vapor (with a vapor diffusion distance of 0.5 cm) at 600˚C for 2 h (bar: 20 µm)

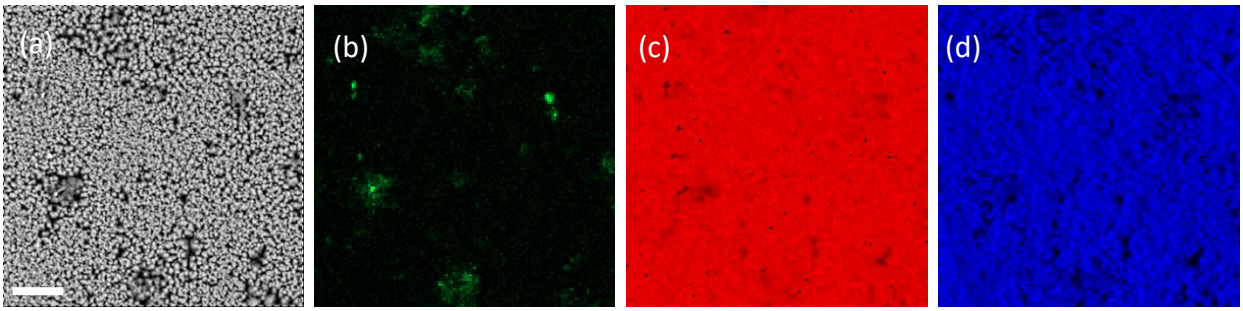

Figure 2.9. a) BSE image and associated element maps of b) oxygen, c) magnesium, and d) silicon obtained from the external surface of a <100> oriented Si single crystal plate containing MgO particles (inert markers) after reaction with Mg vapor (with a Mg vapor diffusion distance of 0.5 cm at 600˚C for 2 h (bar: 20 µm)

The inert marker experiment revealed the presence of MgO particles (Figure 2.8 and Figure 2.9) only on the external surface of the reaction-formed Mg_2Si film (not inside the Mg_2Si film and not at the Mg_2Si/Si interface), which indicated that Mg_2Si formation occurred predominantly at the Mg_2Si/Si interface; that is, new Mg_2Si formed under the MgO particles, causing the MgO particles to be retained at the Mg_2Si/gas interface. This observation also indicated that Mg inward diffusion through the Mg_2Si film was the rate-limiting process for Mg_2Si formation. This result was consistent with the work by Chu *et al* [16], who used implanted Xe ions in Si substrates as inert markers to determine that the solid-state formation of Mg_2Si (by the reaction of solid Mg films with Si at 275 ˚C) was controlled by inward Mg atom diffusion.

2.5 Conclusions

Dense, conformal, and continuous Mg_2Si films were generated on single crystal Si plates by the reaction of such plates with Mg vapor at 600^{o}C. Oxidation during such silicide formation was avoided by conducting the vapor/solid reaction within metal ampoules that were sealed in an Ar atmosphere. Upon heating, magnesium vapor (generated from solid magnesium sealed within the ampoule) migrated to, and underwent reaction with, the single crystal silicon plate. The thickness of the conformal Mg_2Si product layer formed on the Si plate was evaluated as a function of reaction time by direct (local) measurement of the layer thickness from specimen cross-sections (via electron microscopy) and by indirect (global) measurement of the mass change per area of the specimen.

The change in thickness of the Mg_2Si layer with reaction time at 600^{o}C was found to follow parabolic kinetics. The values of the parabolic rate constant, K_p, obtained from both types of film thickness measurements (utilizing electron microscopy and mass change per area) were in excellent agreement. These K_p values were also in reasonable agreement with extrapolations of previously-reported K_p values obtained at lower temperatures for the thickening of Mg_2Si films formed by the solid-state reaction of Mg films deposited on Si single crystal substrates. Changes in the diffusion distance of the Mg vapor (i.e., the distance from the solid Mg vapor source to the Si single crystal plate) and in the orientation of the Si single crystal substrate were found to have negligible influences on the thickness of the Mg_2Si films. These observations were consistent with solid-state diffusion through the Mg_2Si product layer as the rate-determining step for such silicide

formation. Inert markers (fine MgO particles) placed on the Si single crystal plate were found exclusively at the external Mg_2Si film surface after reaction, which indicated that Mg_2Si formed predominantly at the Mg_2Si/Si interface and that inward Mg diffusion through the Mg_2Si layer was the rate-limiting process.

3. CONVERSION OF *Morpho rhetenor* BUTTERFLY WINGS INTO 3D INORGANIC REPLICAS

3.1 Introduction

3.1.1 *Morpho rhetenor* Wing Photonic Structure and Replication

Nature provides impressive examples of hierarchically-patterned, three-dimensional (3-D) structures for the control of light. Among the most recognized examples are the structural colors of the intricate wing scales of butterflies and moths. For example, the wings of *Morpho* butterflies exhibit a brilliant, intense blue color that can even be observed from low-flying aircraft [78]. As shown in

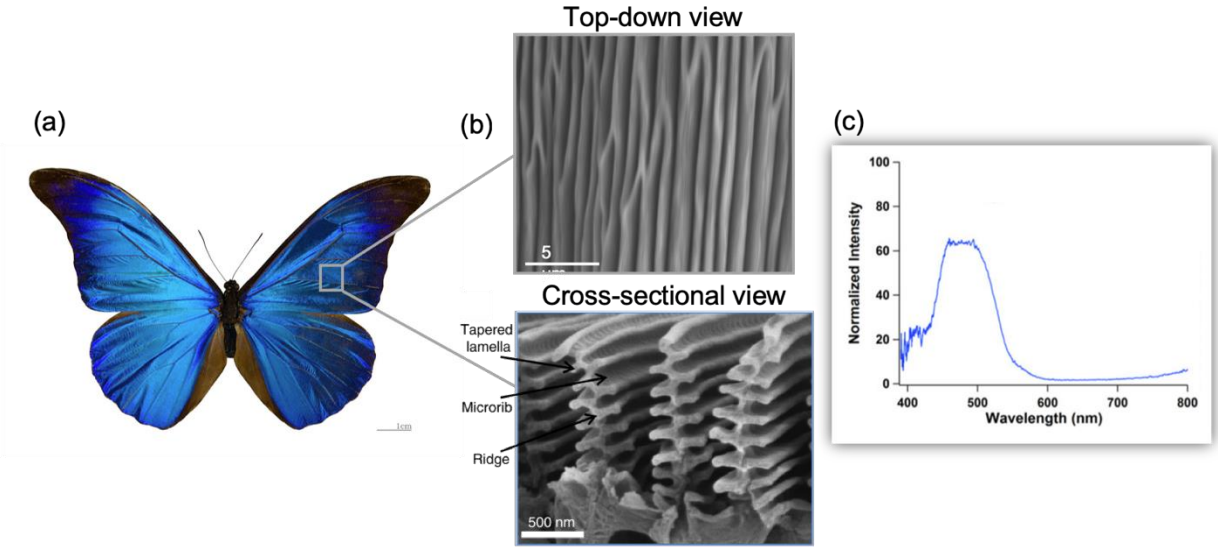

Figure 3.1, the photonic structures of *Morpho rhetenor* wings are comprised of discrete multilayers of cuticle and air [79]. Each wing scale possesses lateral dimensions of around 80 x 200 μm and contains parallel ridges that are 600 nm apart from each other [80]. A cross-sectional view of the scale shows that each ridge contains multiple lamellae, in the form of a "Christmas-tree" structure. The general agreement about the structural coloration of the *Morpho rhetenor* butterfly includes selective blue reflection from the multilayered ridge structure and broad-angle reflection due to the narrow, sub-wavelength width ridges [81–84].

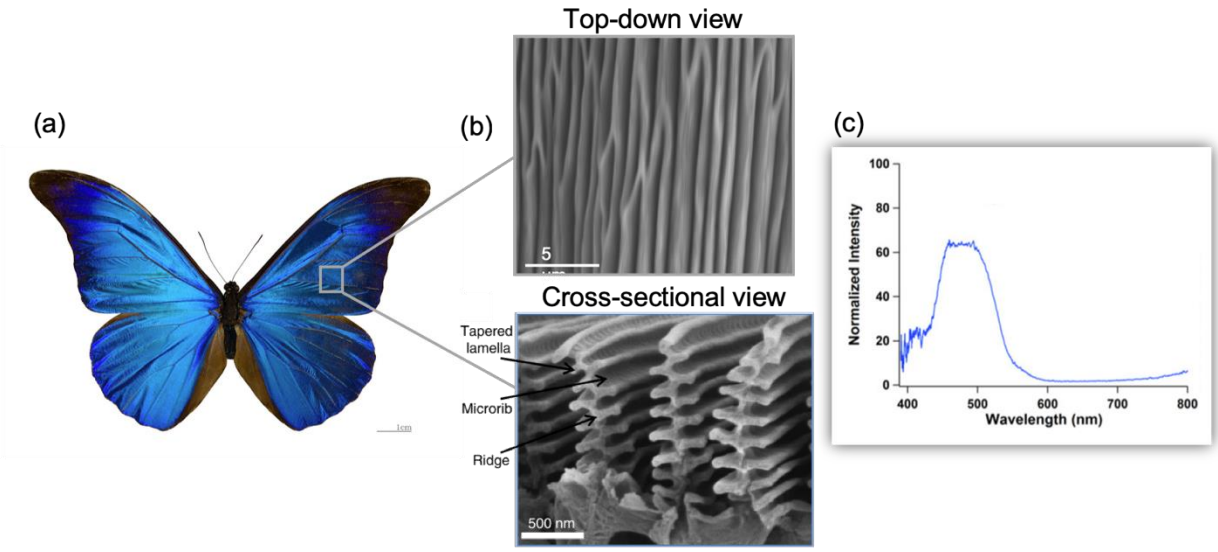

Figure 3.1. Images of *Morpho rhetenor*. (a) An optical image and (b) top-down and cross-sectional views of the butterfly wing scale. (c) reflectance spectra of a native *Morpho rhetenor* butterfly wing. Images (a)(b) were adapted from [85] with permission, Copyright of Creative Commons Attribution 4.0 International License: https://creativecommons.org/licenses/by/4.0/. Image (c) was adapted from [86] with permission from the publisher IOP Publishing.

The optical behavior of intricate 3-D *Morpho* butterfly scale structures has been studied [83, 87–89] and such structures have been replicated [85, 90–93]. Replication methods that have been developed include structural etching on thin films [90, 91] and focused-ion beam induced chemical vapor deposition (FIB-CVD) [92]. These methods require high-vacuum equipment, or line-of-sight deposition, which can be expensive and difficult to scale up. The complexity of the structure of *Morpho rhetenor* scales presents significant challenges for replication to mimic and tailor the brilliant optical behavior.

The major component of a native butterfly wing is an organic chemical named chitin [94]. Chitin contains abundant hydroxyl groups, which can react with metal alkoxides and release alcohols. Therefore, utilizing the native butterfly wings as bioorganic templates to replicate the nanostructure via surface sol-gel coating can be very promising, and was pursued in this chapter. In this work, a conformal surface sol-gel coating process using tetraethyl orthosilicate (TEOS) was developed to replicate the wing scale nanostructure. Such sol-gel derived replicas then underwent shape-preserving chemical reactions to form replicas with various compositions for a broader range of application. More details about the kinetics and adsorption behavior of the surface sol-gel coating of TEOS on chitin will be discussed further in Chapter 4.

3.1.2 Potential Applications of *Morpho rhetenor* Wing Scale Replicas

The brilliant blue iridescence of native *Morpho rhetenor* wings is a type of structural coloration due to interaction of the native wing scale with incident light. Some prior work has been conducted to tailor visible reflection by changing the chemistry (refractive index) of such nanostructures [90, 93, 95, 96]. Among those, S. Jo, *et al.* [96] proposed a facile method to fabricate bioinspired 3-D *Morpho* scale "Christmas-tree" structures by sequentially stacking 11 layers of alternating SiO_2 and TiO_2 films and dry-etching after nanoimprint lithography. The resulting replica exhibited a greenish color, indicating that the reflection was shifted by changing the chemistry of the replicas. Such initial work provided motivation to examine the unexplored coupling of biological and associated biomimetic structures with high IR refractive index synthetic materials, in order to be able to shift the impressive optical behaviors of such photonic structure from the visible range well into the IR, so as to yield a new generation of bio-enabled and biomimetic materials for tailorable control of IR radiation. The chitin present in butterfly scales only possesses a refractive index of less than 1.53 at ≥ 850 nm [84]. Therefore, it's not surprising that the structural coloration of butterfly wings falls in the visible range. In order to mimic such optical behavior in the IR range, such replicas should contain high refractive index chemistries to achieve enhanced interaction with the IR light. In Chapter 1 of this thesis, chemical conversion steps with excellent shape preservation have been developed to convert SiO_2 structures into Mg_2Si, which possesses a high refractive index at infrared wavelengths. Similar chemical conversions will be conducted on the wing replicas in this Chapter to yield *Morpho rhetenor* scales comprised of this high refractive index silicide.

Another potential application for such replicas is based on an intermediate Si product of the reactive conversion process. After dissolving MgO from MgO/Si replicas, porous Si replicas with the *Morpho* butterfly scale architecture can be obtained. In recent years, nanostructured Si has been very promising for high capacity anodes in lithium batteries, due to its high specific capacity compared to that of conventional graphite anodes [97–100]. Silicon has a high theoretical gravimetric capacity of approximately 4200 mA h/g, compared to only 372 mA h/g for graphite [101]. However, a critical issue with using Si for lithium ion battery anodes is the large volume change (~ 400 % [101]) during lithiation and delithiation, which results in poor cyclability and rapid degradation [102, 103]. The nanostructure of *Morpho rhetenor* replicas exhibits a large surface-to-volume ratio, and the ridges and lamellae could provide efficient transport channels for

Li ions during charge and discharge cycles. Researchers have explored replicating bio-inspired butterfly wing structures for lithium battery electrodes. Y. Li, *et al.* [104] prepared carbon/SnO_2 composite replicas using *Euploea mulciber* butterfly wings as templates for anodes in lithium batteries, and the composite replicas showed excellent reversible capacity and cycling consistency. Other researchers have utilized simple sol-gel processing to synthesize TiO_2 structures using butterfly wings as templates for lithium batteries, and they attributed the high performance of the TiO_2 anode to its high surface area and electron transport channels [105, 106]. Therefore, with the promising 3D periodic nanostructure of *Morpho rhetenor* wing scales for anodes in lithium batteries, coupled with our capability of fabricating porous Si replicas with outstanding shape preservation, the use of such replicas as battery anodes will be investigated and discussed in this Chapter.

Another method to enhance the cyclability of Si as an anode material is to prepare Si/C hybrid structures. By coupling C with Si, a combination of two favorable material properties can be achieved. The high lithiation capacity of Si and the mechanical and electrical properties of C make Si/C hybrid materials preferred candidates for enhanced anode performance [107–111]. If the native wings are used as bio-templates for fabricating replicas, then the carbon from the native organic material (chitin) in the wings can be retained by charring. In this way, a Si/C composite replica with a Si coating on a C bio-structure can be fabricated for anode applications. In addition, prior work has been conducted to deposit a thin conformal layer of graphite on complex-shaped materials. M. Caccia, *et al.* [112] has successfully deposited a thin layer of graphite (5-10 nm) uniformly on mesoporous SiO_2 powders using methane deposition and decomposition at 950 ˚C. Such a coating process was also conducted in this chapter on porous Si *Morpho* butterfly scale replicas to fabricate a Si/C hybrid replica with a conformal carbon layer on Si photonic nanostructure.

3.2 Experimental Procedures

3.2.1 Silica Sol-gel Coating of *M. rhetenor* Butterfly Wings

The silica sol-gel solution preparation can be found in Chapter 1.2.1 of this thesis. *M. rhetenor* butterfly specimens were purchased from Butterfly Utopia (Apex, NC, USA). Each butterfly has four wings, two on each side (a forewing and a hindwing). For a general silica sol-

gel coating process, a wing was immersed in a silica sol-gel solution for 3 mins to allow for chemisorption onto the wing template. Next, the wing was rinsed in anhydrous ethanol (99.5 %, 200 proof, Fisher Scientific, Hampton, NH, USA) by immersing in ethanol for 3 mins to wash off excess, non-chemisorbed molecules. Finally, the wing was immersed in DI water (MilliQ®, Burlington, MA, USA) at room temperature for 3 mins to hydroxylate the surface for the next coating cycle, followed by drying with clean nitrogen gas (99.9 %, Air Gas, Radnor, PA, USA) at room temperature for 1 min.

3.2.2 Conversion into SiO_2, MgO/Si, Porous Si, and Mg_2Si *M. rhetenor* Replicas

After silica sol-gel coating, the wing was carefully placed in between two glass substrates (McMaster-Carr, IL, USA), as shown in Figure 3.2. The glass substrates with the coated wings were placed on an alumina plate (9" x 1.5", Tateho Ozark Technical Ceramics, Webb City, MO, USA), and then fired in ambient stagnant air in a horizontal tube furnace (Sentro Tech Corp, Strongsville, OH, USA) at a low heating rate of 0.5 ˚C/min to prevent severe scale cracking and wrinkling to 500 ˚C and then held at this temperature for 4 h. The as-fired replicas turned white, indicating the formation of SiO_2 and a removal of organics. The SiO_2 replicas were then converted to MgO/Si via magnesiothermic reduction at 750 ˚C for 6 h. The MgO was then selectively dissolved using 3 M HCl solution, and the porous Si replicas were exposed to Mg vapor at 600 ˚C for 2 h to form Mg_2Si. The experimental set up and conditions for chemical conversion steps from SiO_2 to Mg_2Si were discussed in detail in Chapter sections 1.2.4, and 1.2.5 in this thesis.

Figure 3.2. A photograph of SiO_2 coated *M. rhetenor* wings clamped between two glass substrates.

3.2.3 Replica Morphology, Phase Content, and Optical Property Measurements

A FEI NOVA nanoSEM Field Emission SEM was used to observe the morphology of the *M. rhetenor* scale replicas. To acquire SEM images of the cross-sectional views of the replicas, the replica scales were milled using a focused ion beam, using a FEI Quanta 3D Field-emission Dual-beam SEM. The sample was then transferred to the higher resolution NOVA SEM to observe the "Christmas-tree" structure. Focused-ion-beam (FIB) milling was conducted using a voltage of 30 keV and ion-beam current of 0.5-3 nA. Prior to ion-beam milling, a ~1 μm Pt layer was deposited using an ion-beam Pt source at 20 keV and 19 nA. The Pt layer helped to protect the surface morphology from being milled so as to preserve the sample features. Electron dispersive X-ray analyses (EDS) were conducted using an Oxford INCA Xstream-2 silicon drift detector with a Xmax80 window. The phase content of the replicas after each conversion step was characterized by a D2 Phaser X-ray Diffraction (XRD) instrument from Bruker AXS GmbH, Germany. The coated wings became fragments (sizes less than 1 cm x 1 cm) after firing in the air. The replica fragments were placed in a zero-diffraction plate holder (MTI Corporation, Richmond, CA, USA) for XRD measurement. The 2θ scanning range was from 25˚ to 90˚, with a step size of 0.018˚ and a dwell time of 0.2 sec/step.

Optical images of *Morpho rhetenor* butterfly scale replicas were acquired using an Olympus BX51 microscope (Olympus Corp., Tokyo Japan). The spectral distribution over the surface of the replicas were performed using a PARISS hyperspectral imaging system (LightForm, Inc., San Francisco, CA, USA) mounted on a Nikon 80i microscope (Tokyo, Japan), with objective from 4x to 100x. The hyperspectral imaging system obtained the entire spectra simultaneously for every pixel of a column, which was repeated until the whole area of interested was covered. The PARISS software recorded and identified a set of absorption spectra, where absorbance is expressed in Arbitrary Units (A.U.). Each spectrum was assigned a coded color that reflects the identity of the spectrum from the corresponding area (and not the actual color of the sample).

3.2.4 Surface Sol-gel Coating of *M. rhetenor* Wing Scales

To fabricate *M. rhetenor* replicas with thinner lamellae layers, a surface sol-gel (SSG) coating process was developed and applied to the native butterfly scales. For SSG coating, TEOS molecules were reacted with hydroxyl groups on chitin in the native butterfly scales (similar to the hydrolysis reaction of TEOS with water). The SSG method provides a molecular layer-by-layer coating of TEOS on the native wing scales, and the thickness can be tailored by controlling the number of coating cycles. In this study, the TEOS precursor solution was prepared by diluting TEOS in anhydrous ethanol to a volume ratio of 1:1. The pH of this precursor solution was adjusted to 1 by using 0.5 M HCl (aq). One coating cycle is introduced as follows. First, the native wing was immersed in the TEOS/EtOH precursor solution for 3 min, followed by rinsing away the excess unreacted TEOS molecules in anhydrous ethanol via a 3-min immersion. Second, the rinsed wing was dipped in DI water (pH adjusted to 1, to catalyze hydrolysis) for 3 min, followed by rinsing in anhydrous ethanol again via a 3-min immersion, and drying by blowing nitrogen stream gently for 1 min at 1 cfm flow rate. The SSG layer-by-layer (LbL) process was conducted using a multi-vessel dip coater (KSV NIMA Dip Coater Multi Vessel Small, NanoScience Instruments, Phoenix, AZ, USA). The SSG coating process was repeated for 100 and 150 cycles, respectively. The resulting replicas were fired in air and converted in the same fashion as the silica sol-gel coated replicas. The morphology, chemistry, and phase content of such replicas were evaluated by SEM, EDS, and XRD analyses, respectively.

3.2.5 Fabrication of Si/C Composite Replicas by Carbonization of the Native Wings

To prepare Si/C hybrid replicas for the Li-ion battery anode application, one method that was developed in this study was to retain the native carbon in *M. rhetenor* wing scales by charring the silica sol-gel coated wings in an inert atmosphere. The butterfly wings are composed of mostly chitin, which contains long carbon-bearing chains in the polymer structure. The carbon in chitin can be retained and utilized as the carbon source to prepare Si/C hybrid nanostructures. For this sample preparation step, a silica sol-gel coating was applied on the native butterfly wings, as described in section 3.2.1 in this chapter. Next, instead of firing the coated wings in air to obtain SiO_2 replicas, the coated wings were fired in an Ar atmosphere (P_{O2} < 0.1 ppm) in a horizontal tube furnace to obtain SiO_2/C replicas. Charring was conducted by heating at 0.5 ˚C/min to 500 ˚C and holding at this temperature for 4 h.

One other difference for preparing this Si/C replica was the acid solution used for MgO dissolution. Instead of using a 3 M aqueous HCl solution, where water was the sole solvent, a 3 M HCl methanol solution was prepared by diluting concentrated HCl (37 % solution in water, Fisher Scientific, Hampton, NH, USA) in anhydrous methanol (Certified ACS, Fisher Scientific, Hampton, NH, USA). The MgO/Si/C replicas were immersed in this HCl-MeOH acidic solution for 4 h, followed by rinsing in methanol via a 1-min immersion and drying in the Ar atmosphere glovebox for 6 h to obtain Si/C replicas.

3.2.6 Fabrication of Si/C Hybrid Replicas by Methane Vapor-based C Deposition on Si

Another approach created to fabricate Si/C replicas was to coat the porous Si replicas uniformly with a thin layer of graphite, which is more conductive than amorphous carbon. In this study, porous Si replicas were prepared first. Then replicas were placed in a round alumina crucible (diameter 1”, height 0.5”, Tateho Ozark Technical Ceramics, Webb City, MO, USA) and inserted in a horizontal tube furnace. The furnace was first evacuated using a RV Two Stage Rotary Vane Pump (Edwards, Burgess Hill, England) until the vacuum reached -30 in Hg (indicated by the pressure gauge on the end cap), and then backfilled with a mixture of 10 vol % methane with Ar (Indiana Oxygen, Lafayette, IN, USA) at a flow rate of 20 ± 4 mL/min. The evacuation and backfill cycle were repeated 3 times. Then the deposition reaction was conducted at 950 ˚C with continuous methane/Ar mixture gas flowing at a rate of 20 ± 4 mL/min, by heating at rate of 3 ˚C/min to 950

˚C. The methane chemical vapor deposition reaction was conducted for 6 h and 0.5 h at 950 ˚C to apply graphite coatings of different thicknesses. After retrieving the samples from the furnace, XRD analyses were used for phase identification, and cross sections were generated using focused-ion-beam milling. Morphology and chemical characterization were conducted using FEG-SEM and EDS.

3.3 Results and Discussion

3.3.1 Morphology and Phase Analyses of the Sol-gel Coated Replicas

Native *Morpho rhetenor* wings were coated with a pre-hydrolyzed silica sol-gel solution prepared using a TEOS alkoxide precursor, by immersing in the sol-gel solution for 3 min, rinsing in anhydrous ethanol, and incubating in DI water for 3 min, followed by drying in flowing nitrogen. This coating cycle was repeated twice. After firing the as-coated wings in air for 4 h at 500 ˚C, a thin carbon layer (5 – 10 nm) was deposited using a carbon coater to make the sample conductive for SEM analyses.

The SE images in Figure 3.3 revealed the nanostructure of the SiO_2 replicas. Overall, the shapes of the native scales were well preserved in the SiO_2 replicas. The complex delicate features, such as ridges and lamellae, were well retained in the replicated silica structures. The FIB milled cross sections clearly revealed the "Christmas-tree" structure. Each ridge consisted of around 10 stacks of the layers and each lamella was approximately 80 nm thick.

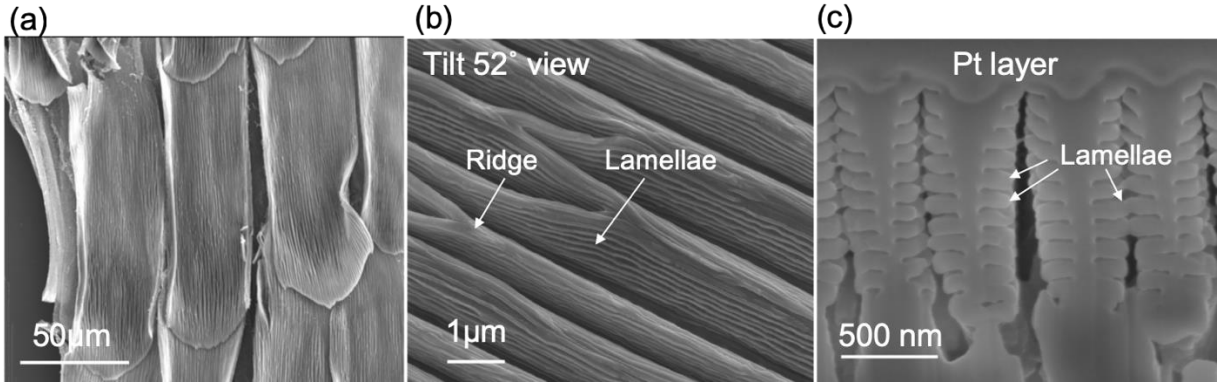

Figure 3.3. SE images of as-fired silica replicas after sol-gel coating on native butterfly wings. (a) Top-down image of replica scales, (b) Tilted view (52˚) of the fine details on the silica replica, and (c) a cross section image of a single silica replica scale milled by FIB.

The silica replicas were then exposed to Mg vapor generated by Mg_2Si granules at 750˚C for 6 h to produce MgO/Si replicas. The shape was well preserved according to SE images (Figure 3.4), and EDS analyses (Figure 3.5) revealed appreciable amounts of magnesium, silicon and oxygen, consistent with the formation of MgO/Si. In addition, Mg, Si and O were evenly distributed in the MgO/Si replicas as seen in the EDS mappings, confirming a uniform coating of the wing template.

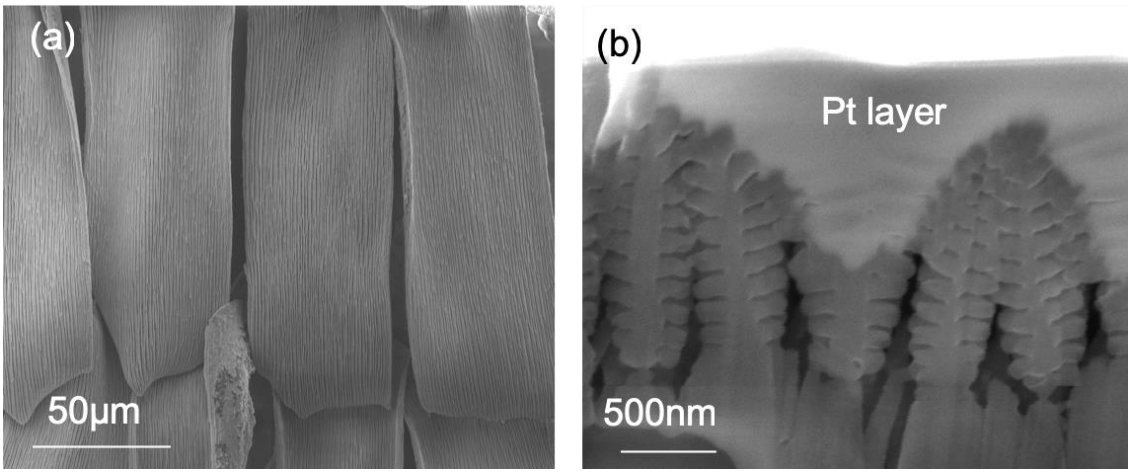

Figure 3.4. (a) Top-down and (b) FIB milled cross-section SE images of MgO/Si replicas after conversion at 750 ˚C for 6 h.

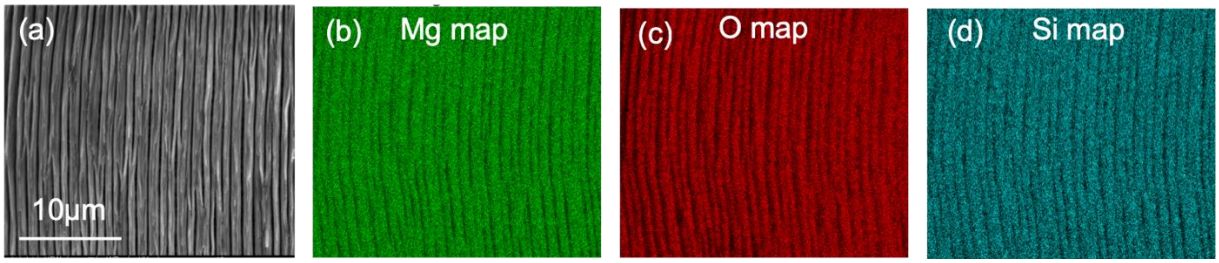

Figure 3.5. EDS elemental mappings of MgO/Si replicas.

The MgO/Si replicas were then immersed in 3M HCl to remove the MgO, followed by rinsing in DI water by immersing for 1 min. Without rinsing in water, $MgCl_2$ would precipitate out on the replicas during drying. After the acid dissolution step, the replicas were dried overnight at room temperature in the Ar atmosphere glovebox. SE images were taken of the porous Si replicas and cross sections were milled by FIB to observe the lamellae. As seen in Figure 3.6, the

"Christmas-tree" structure was retained well after acid dissolution, and nano-sized pores were generated throughout the lamellae due to the removal of MgO phase.

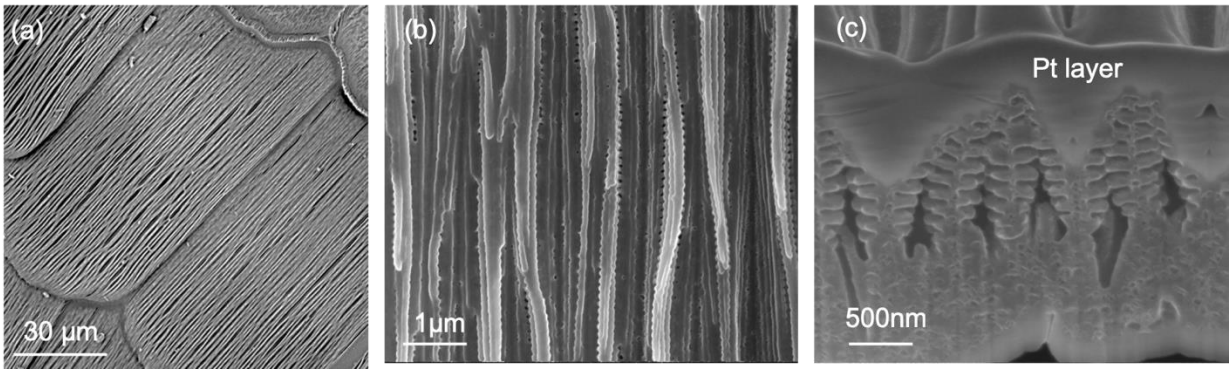

Figure 3.6. (a) (b)Top-down and (c) FIB milled cross-section SE images of porous Si replicas after selectively removing MgO using 3 M HCl (aq).

Porous Si replicas were then reacted with Mg vapor generated from pure Mg metal foil for the conversion step to Mg_2Si. The reaction was conducted at 600 ˚C for 2 h in a low-carbon steel ampoule sealed in Ar atmosphere (P_{O2} < 0.1 ppm). SE images of converted Mg_2Si replicas (Figure 3.7) indicated overall shape preservation.

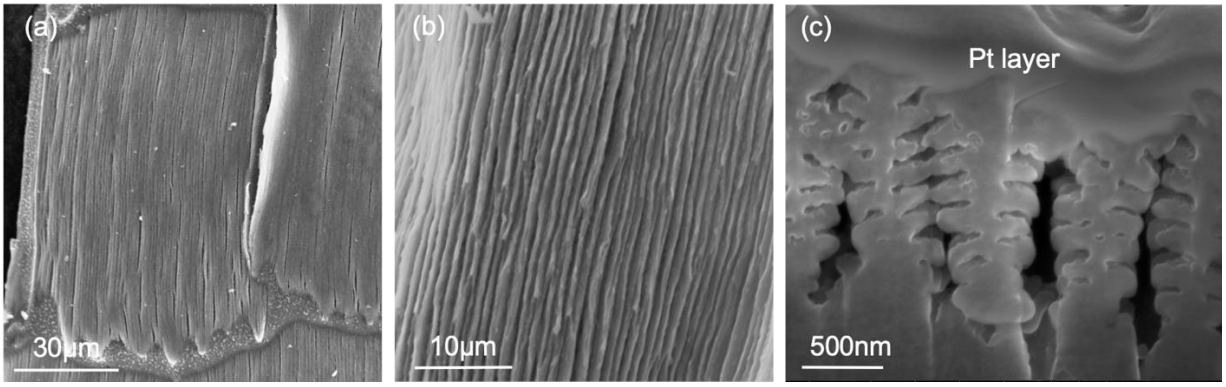

Figure 3.7. (a)(b) Top-down and (c) FIB milled cross-section SEM images of a Mg_2Si replicas.

The X-ray diffraction analyses were conducted at each stage of the replication process (i.e., SiO_2, MgO/Si, porous Si, and Mg_2Si). Figure 3.8 indicated that the chemical conversions were successful, and each conversion stage yielded the desired phase content.

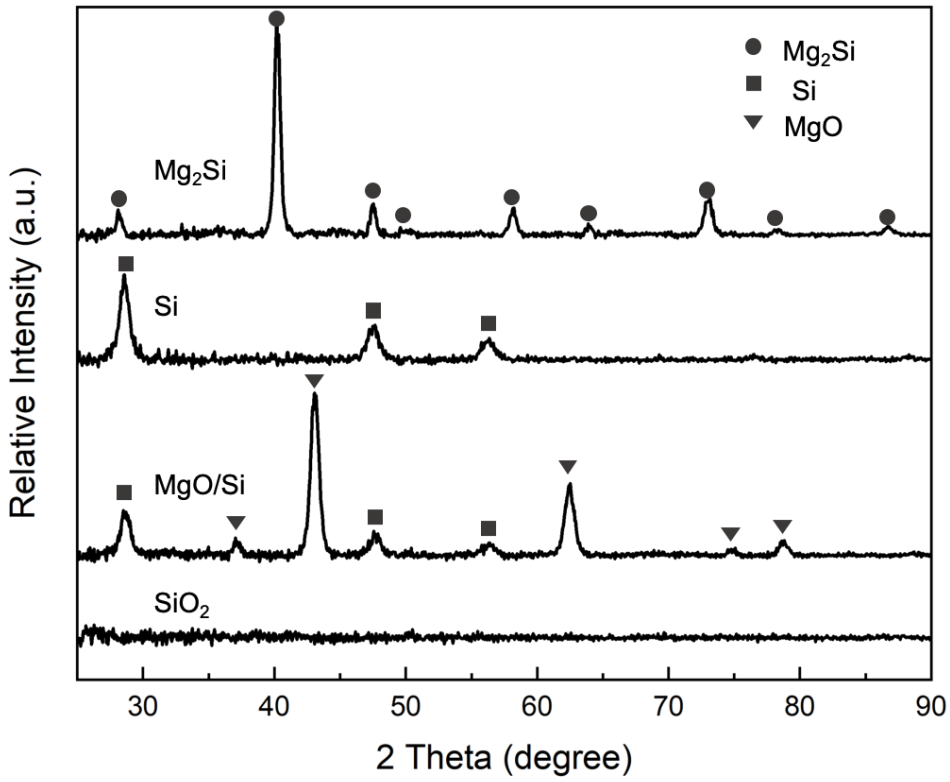

Figure 3.8. XRD spectra of SiO_2, MgO/Si, porous Si, and Mg_2Si *Morpho rhetenor* replicas, respectively.

3.3.2 Reflectivity Measurements of SiO_2 Replicas

Reflectance behavior was measured on sol-gel coated and air sintered SiO_2 butterfly scale replicas. The reflectance spectra of an individual SiO_2 replica scale were acquired using a PARISS hyperspectral imager equipped with a 100x microscope objective. The measurements were performed by Michael Allen from Deheyn Group at University of California San Diego. For SiO_2 replica scale reflectance measurement, the wavelength of the incident light was in a range of 360-1000 nm. Figure 3.9 (a) shows the hyperspectral mapping over a replica scale area of 25 µm x 50 µm. The different colors in the reflectance spectra in Figure 3.9 (b) corresponded to different color-coded areas in Figure 3.9 (a). The spectra revealed strong reflectance peaks between 380 and 400 nm, which was near the Ultraviolet (UV) wavelength range. The reflectance of the SiO_2 replica scales was blue-shifted compared to native *Morpho rhetenor* butterfly scales, the intensity peaks of which lie between 460 and 500 nm wavelength [85]. The reflectance intensity peak shift was consistent with the refractive index decrease from native butterfly scale component, chitin, to SiO_2

replicas (refractive index of SiO_2 is 1.45 at 850 nm, whereas the refractive index of chitin is 1.53 at 850 nm). Hence, it could be expected that the reflectance intensity peaks would shift to the higher wavelength range when increasing the refractive index of the replica materials. IR reflectivity measurements on the higher refractive index Mg_2Si replicas will be conducted at the Deheyn group in the future.

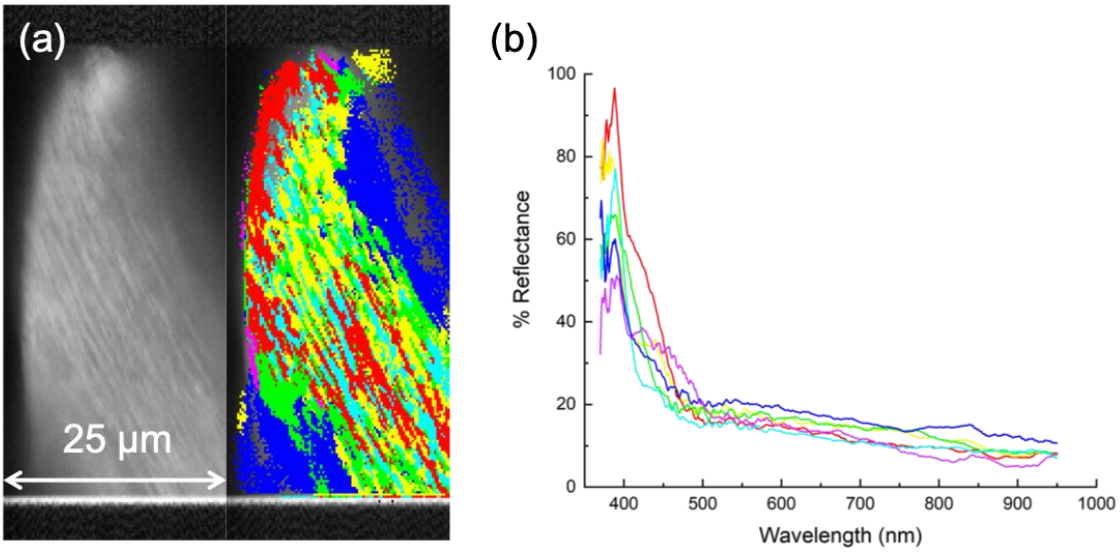

Figure 3.9. (a) Optical image and hyperspectral mapping, (b) reflectance spectra of an individual SiO_2 replica scale. Data Acquired by Michael Allen from the Scripps Research Institute of UC San Diego.

3.3.3 Surface Sol-gel (SSG) Coating, Morphology and Phase Analyses of the Replicas

A surface sol-gel coating method has also been developed and conducted on native *Morpho* wings to fabricate replicas with controllable coating thicknesses. As described in the experimental section, TEOS was used as the metal alkoxide precursor for preparation of silica replicas. An automated multivessel dip coater was utilized to apply layer-by-layer SSG coatings by immersing the native wings into different solutions. The coating process was repeated for 100 and 150 cycles, respectively, to investigate the increase in thickness resulting from an increase in SSG cycles. The mechanism for the coating process is illustrated in Figure 3.10 [113]. Silicon metal alkoxide molecules react with the hydroxyl groups on the scale surface and release alcohols. As discussed in Chapter 1 in this thesis, the hydrolysis reaction of a metal alkoxide can be accelerated by the use of acid or base as catalysts. For TEOS, the hydrolysis rate is very slow without adding a catalyst, and the hydrolysis rate constant of TEOS in water increases as the pH of the solution

decreases [28]. Previously in this thesis, HCl was used as a catalyst to prepare a silica sol-gel solution. Therefore, to facilitate the hydrolysis reaction during SSG coating, the pH of the solutions was adjusted to 1 using 0.5 M HCl.

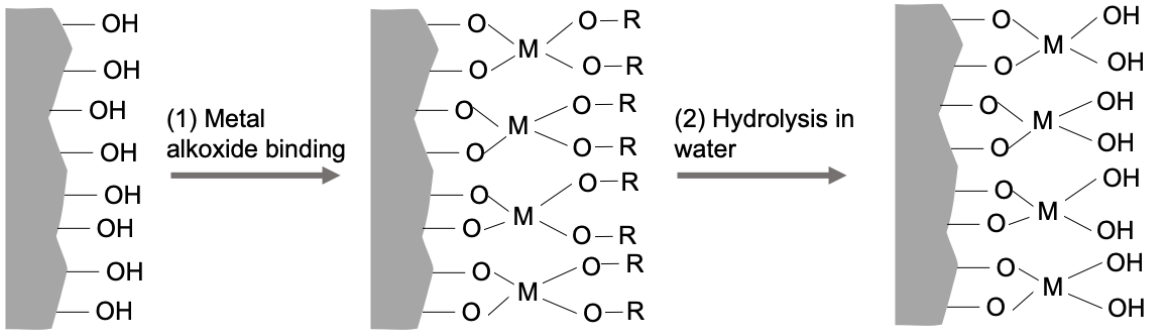

Figure 3.10. Illustration of a cycle of surface-sol-gel coating using a metal alkoxide precursor with a hydroxyl-rich surface.

To evaluate the morphology and the phase content of the replicas prepared by SSG coating, SEM and EDS analyses were conducted after each of the replication process. Figure 3.11 reveals the shape preservation of the native wing structure, and EDS analyses indicated that the as-coated samples possessed uniformly-distributed Si in the coating.

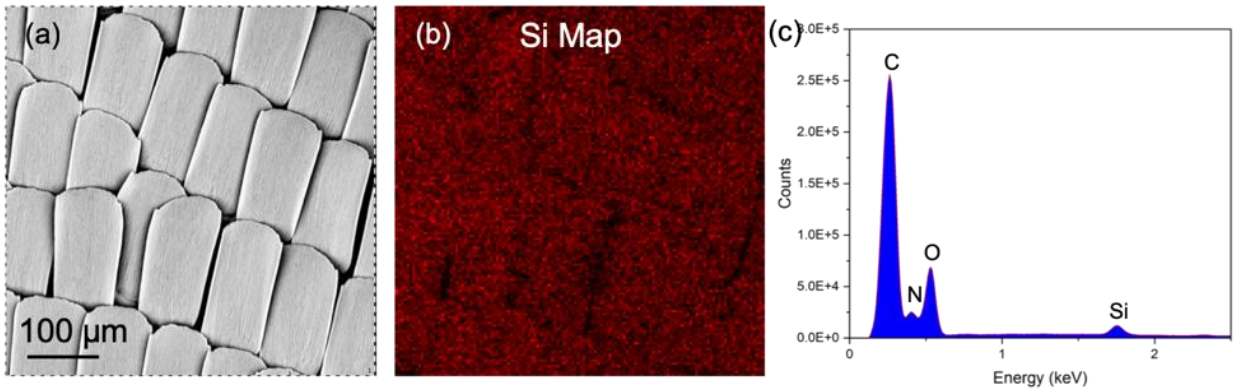

Figure 3.11. (a) BSE image and (b) EDS mapping of Si on an as-coated native *Morpho* wings after 100 cycles of SSG coating.

After SSG coating was completed, the as-coated wings were fired in air at 500˚C, with a low heating rate of 0.5 ˚C/min to avoid severe cracking and wrinkling of the wing scales. For the as-fired SiO_2 replicas, FIB milled cross sections of the scale were obtained and SEM imaging was conducted to observe the microstructure of the replicas. Figure 3.12 confirms the replication of the

intricate nanostructure. The lamellae thickness was reduced by almost half compared to those prepared by silica-sol-gel coating method. Each lamellae layer had a thickness of approximately 45 ± 1 nm.

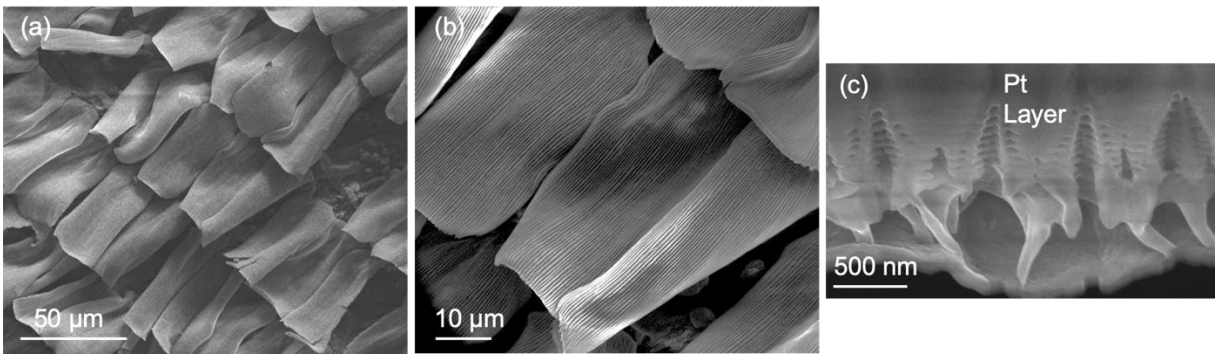

Figure 3.12. (a)(b) Top-down and (c) FIB milled cross-section SE images of as-fired SiO_2 replicas prepared by 100-cycle SSG coating and firing in air.

As-fired SSG coated silica replicas were then converted into MgO/Si replicas via magnesiothermic reduction at 750˚C for 6 h. Similarly, cross sections were obtained by ion-beam milling and SEM images were acquired. Figure 3.13(a) exhibited the "Christmas-tree" structure in the replicated scale cross section, and XRD analyses in Figure 3.13(b) verified the presence of only MgO and Si only after this conversion step.

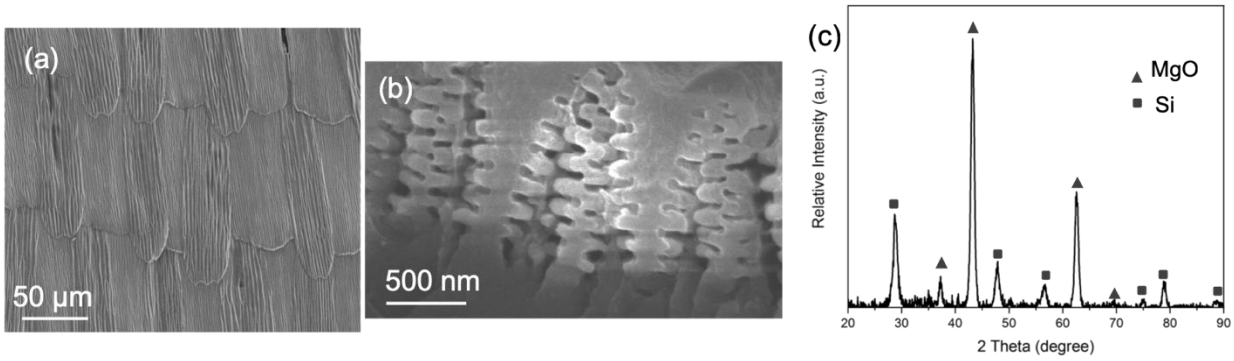

Figure 3.13. (a) Top-down SE image, (b) FIB milled cross-sectional SE image, and (b) XRD analyses of MgO/Si replicas prepared by 100-cycle SSG coating and magnesiothermic reduction.

MgO was then selectively removed by dissolution in 3M HCl. The MgO/Si replicas were immersed in the acid solution for 4 h, to allow for complete removal of MgO. Then the replicas were rinsed gently with DI water by immersing for 1 min to wash off the salts, followed by drying

at room temperature in the glovebox for 12 h. After this acid dissolution step, the "Christmas-tree" structure collapsed and was not retained, as seen in Figure 3.14(a). The ridges were still distinguishable, but the multi lamellae structure was distorted. Possible reasons that caused the structural distortion include: 1) capillary force during drying and 2) lamellae thickness was too thin to mechanically endure the self-weight. If the capillary force during drying caused the collapse of the tree structure, it could be improved by using a low-surface-tension solution for rinsing instead of DI water. At 25 ˚C, DI water has a surface tension of 71.97 mN/m, whereas ethanol has a much lower surface tension of 22.27 mN/m [114]. Therefore, ethanol was used for rinsing instead of DI water, and porous Si replicas were generated. Even though the capillary force was reduced, the structure still collapsed after the acid dissolution step, as seen in Figure 3.14(b). This indicated that this porous Si was mechanically too fragile. Hence, another replica was prepared by applying 150-cycle SSG coatings to increase the lamellae thickness, so as to improve the mechanical strength of the structure.

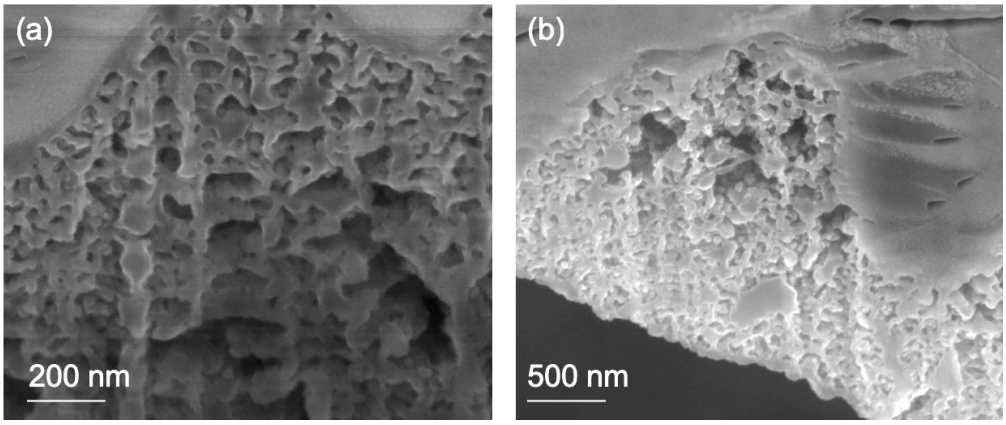

Figure 3.14. SE images of ion-beam milled cross sections on (a) porous Si replica after rinsing with DI water and drying, and (b) porous Si replica after rinsing with Ethanol and drying.

After conducting 150 cycles of SSG coating on native *Morpho* wings, the replicas underwent similar preparation steps as 100-cycle SSG coated wings. Cross sections of these replicas were obtained using ion-beam milling, and SEM images were acquired, as shown in Figure 3.15. Overall, the shape preservation from SiO_2 to porous Si was improved compared to the replicas prepared using 100 cycle SSG coatings. The ridges were standing upwards and the lamellae were not distorted severely after acid dissolution. Furthermore, nano-porosity was

observed from the SE image on the porous Si (Figure 3.15(c)). XRD analyses confirmed the phase content of the replicas after magnesiothermic reduction and acid dissolution.

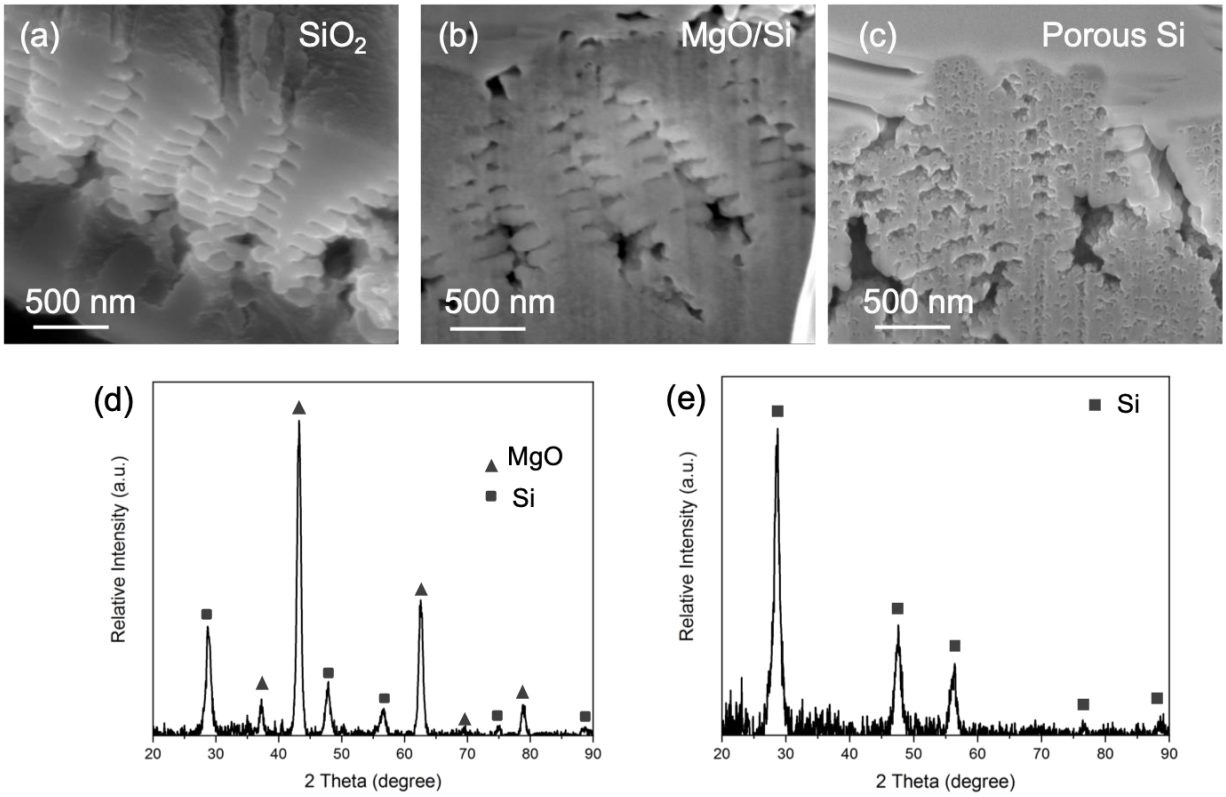

Figure 3.15. SEM images of ion-beam milled cross sections of (a) SiO_2, (b) MgO/Si and (c) porous Si, and (d)(e) X-ray diffraction spectra of MgO/Si and porous Si replicas, respectively, prepared by 150-cycle SSG coating.

The thicknesses of the lamellae in the SiO_2 replicas were measured and compared between 100-cycle and 150-cycle SSG coated samples. After firing, the 100-SSG-cycle SiO_2 replica had a lamellae thickness of 45 ± 1 nm, and 150-cycle SiO_2 replica had a lamellae thickness of 70 ± 1 nm. This thickness growth was consistent with a linear relationship of thickness vs. coating cycles, and it was calculated that each SSG cycle would deposit a 4.5 Å silica layer on the native butterfly wings.

Table 3-1. Thickness of lamellae layer of as-fired SiO_2 replicas prepared by different number of SSG coating cycles

Number of coating cycles	**Lamellae layer thickness**
150	70 ± 1 nm (measured)

100	45 ± 1 nm (measured)
1	4.5 Å (calculated)

3.3.4 Evaluation of Si/C Replicas Prepared via Wing Scale Carbonization

In order to provide electrical pathways to/from the Si nanostructure during the electrochemical tests, Si/C hybrid replicas were developed. One way for fabricating Si/C replicas is to utilize the organic carbon from the native butterfly wing template. In this section, the Si/C replicas were prepared by silica sol-gel coating on the native wings, followed by charring of the wings to retain carbon in the structure.

After charring the native wings coated with silica sol-gel in an inert Ar atmosphere ($p(O_2)$ < 0.1 ppm) , the color of the obtained SiO_2/C replicas turned black, compared to the white SiO_2 replicas prepared previously (Figure 3.16), which was consistent with carbon retention after this process. In addition, the fractured pieces of the replicated wings prepared by charring were larger than the fractured silica wing replicas, due to the apparent robust mechanical behavior of carbon.

Figure 3.16. Optical images of silica sol-gel coated wing scales after firing in air (left) and in inert Ar atmosphere (right).

The charred replicas went through a similar magnesiothermic reduction process to produce MgO/Si/C replicas (i.e., 750 ˚C for 6 h in a low-carbon steel ampoule sealed in Ar atmosphere (P_{O2} < 0.1 ppm)).

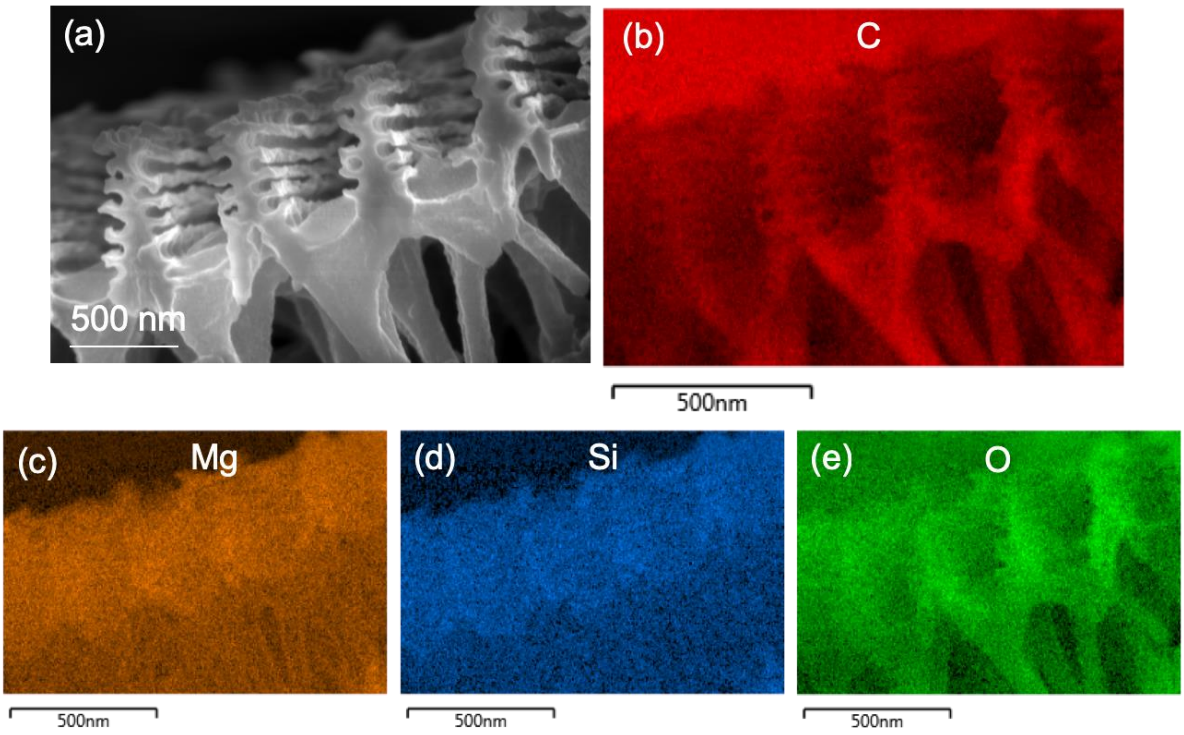

Figure 3.17. (a) Cross sectional SE image and EDS elemental mappings of (b) carbon, (c) Mg, (d) Si, and (e) oxygen of charred SiO_2/C replicas after magnesiothermic reduction.

Figure 3.17 provides a cross sectional view SE image and elemental maps of a charred replica after magnesiothermic reduction. The "Christmas-tree" structure was well preserved, that is, the lamellae and the ridges can be clearly observed from the SE image. The elemental maps of carbon indicated the skeleton structure which was retained from the charring process. The oxygen map revealed where the silica coating was located, and this map indicated that the silica uniformly coated the carbon structure.

To obtain porous Si/C replicas, the MgO/Si/C replicas from the previous step were immersed in 3 M HCl aqueous solution without stirring for 4 h to dissolve MgO. After acid dissolution, the EDS analyses revealed Mg and O, and MgO was also detected by XRD analyses (Figure 3.18). This indicated that MgO dissolution was incomplete after this step.

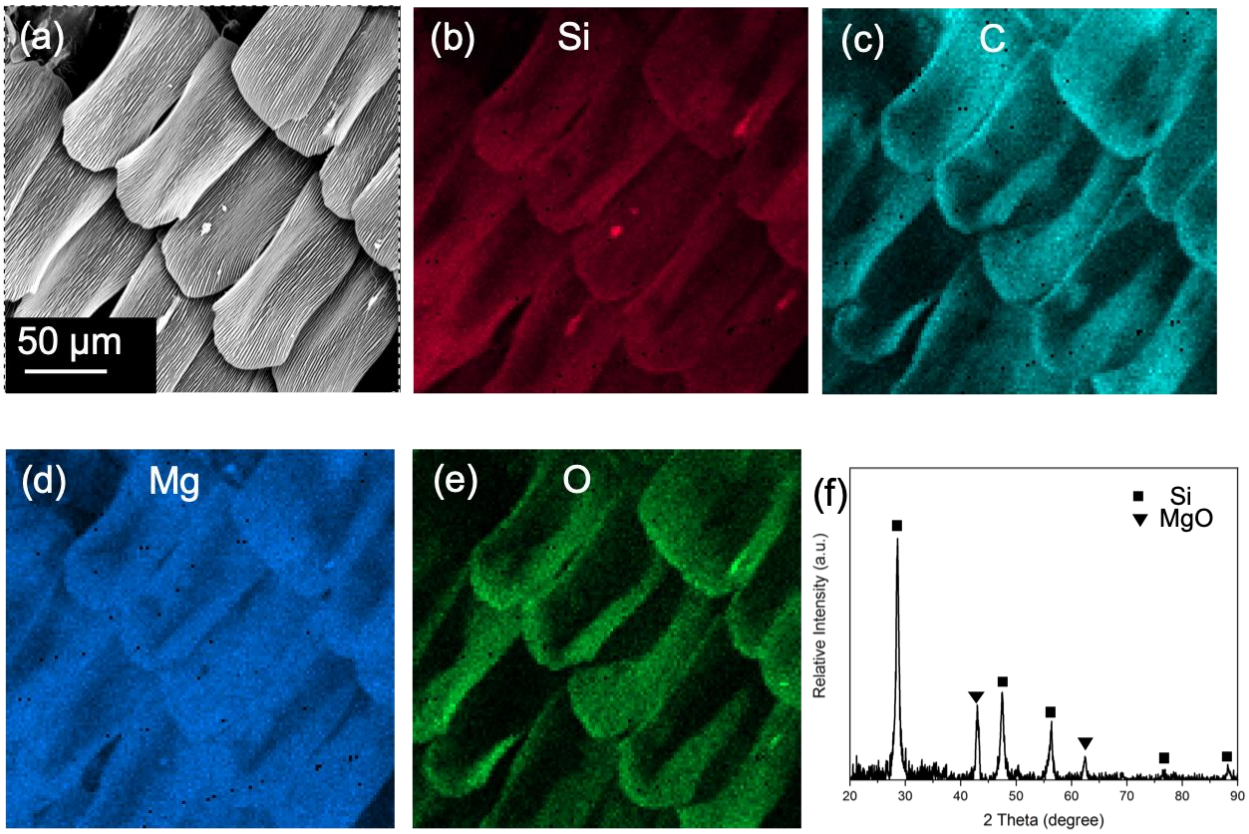

Figure 3.18. (a) Top-down SE image, and EDS elemental mappings of (b) Si, (c) C, (d) Mg, (e) O, respectively, as well as (f) XRD analyses of the MgO/Si/C replicas after dissolving in 3 M HCl solution for 4 h.

Furthermore, when the MgO/Si/C replicas were mixed with the HCl solution, the replicas floated up and were not fully immersed by the acid solution. To reduce the contact angle at the liquid/solid interface for enhanced wetting, the liquid/solid surface tension may be reduced. With the commercially-purchased 3 M HCl aqueous solution, the solvent was water, which possesses a surface tension, γ (water, 20 ˚C) = 72.86 mN/m [115]. Methanol exhibits a lower surface tension: γ (MeOH, 20 ˚C) = 22.50 mN/m [116]. Therefore, a 3 M HCl solution using methanol as the solvent was prepared by diluting concentrated HCl (12 M) to 3 M using methanol. Such a HCl-MeOH-bearing solution was then used to selectively remove MgO from the replicas. The replica pieces did not float on top of the HCl-MeOH solution, which indicated that wettability was improved by introducing methanol into the acid solution. XRD analyses in Figure 3.19 confirmed that the MgO was completely removed from the MgO/Si/C replicas after 4 h of dissolution in the 3 M HCl-MeOH solution. Top-down SEM images of the replicas revealed well-preserved scale

shapes (Figure 3.20), Cross-sectional SE images (Figure 3.20(b)) revealed well-retained "Christmas-tree" structures and nano-porosity generated upon MgO removal.

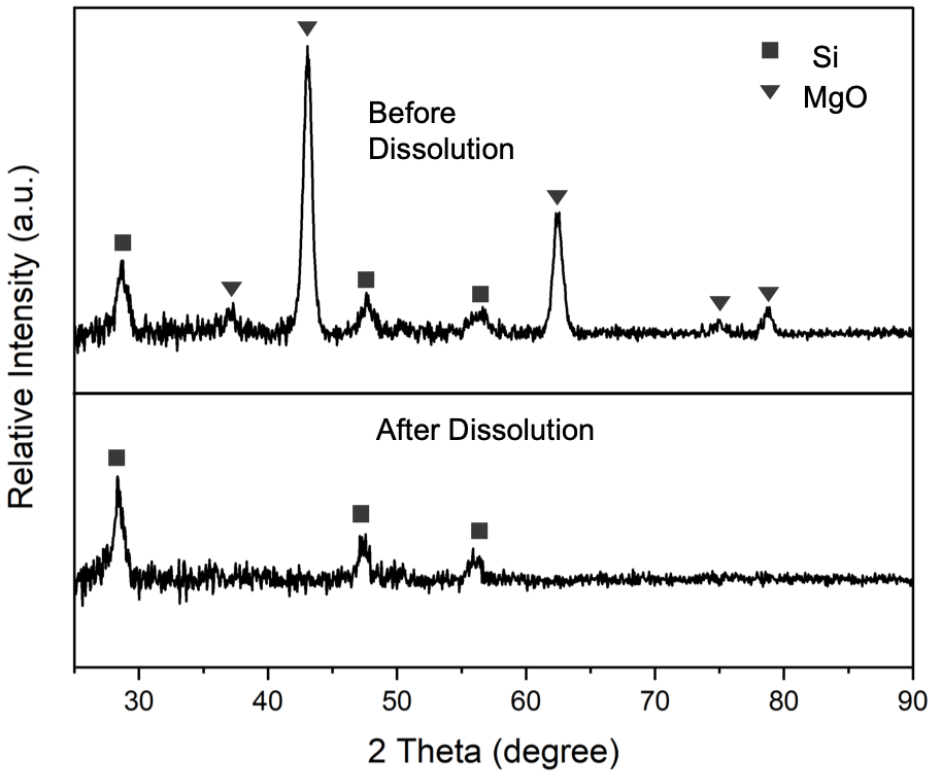

Figure 3.19. XRD analyses of the carbon-bearing replicas before and after acid dissolution in 3 M HCl-MeOH solution for 4 h.

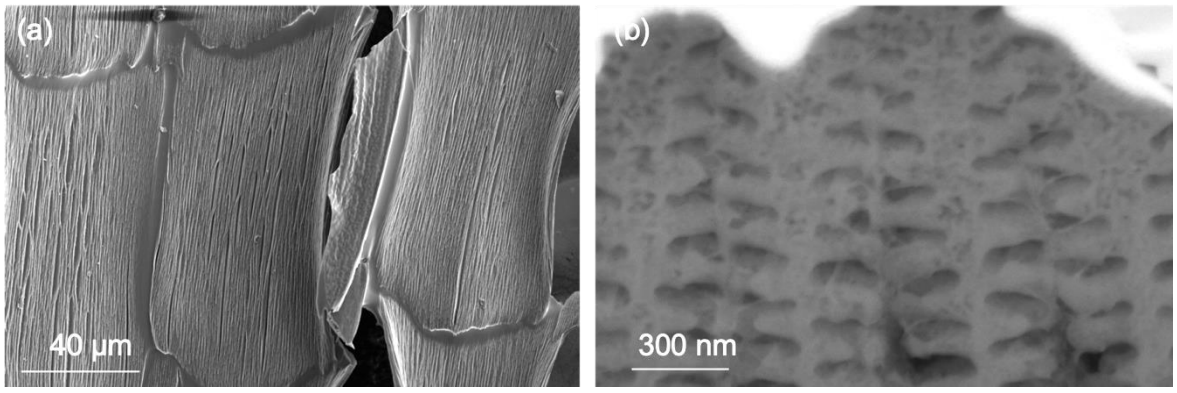

Figure 3.20. (a) Top-down and (b) cross-sectional SE images of the charred Si/C replicas after acid dissolution in a 3M HCl-MeOH solution.

3.3.5 Evaluation of Si/C Replicas Prepared via Methane Vapor Deposition

Another attempt made to prepare Si/C hybrid replicas was to use carbon vapor deposition at high temperature using a carbon precursor (CH_4 in this study). A. Ortega-Trigueros, *et al.* reported successful thin layer graphite deposition onto a SiO_2 mesoporous structure using methane gas at 925 ˚C for different dwell times (1 – 10 h) [112]. With this method, they claimed to obtain a uniformly distributed graphite coating on the porous template, with the coating thickness of 5 to 10 nm, depending on the reaction duration. The Si butterfly scale replicas prepared in section 3.2.2 in this chapter showed nano-sized porosities. In addition, the replicated Si structure had features in the size of tens of nanometers (i.e., the distance between adjacent lamellae layers was 20 to 40 nm). Hence, a 5-10 nm graphite coating layer was of great importance to coat the complex shaped replicas uniformly, but not to block the porosities or the nano architectures.

The Si replicas were placed in an alumina crucible. The replica fragments were spread evenly to a thin layer covering the bottom of the crucible to ensure the maximum exposure of the replicas to methane gas. The carbon vapor deposition on Si replicas was conducted at 950 ˚C for 6 h first, with methane/Ar mixture gas flowing at a rate of 20 ± 4 mL/min. Figure 3.21 revealed a uniform graphite coating on the Si "Christmas-tree" structure, indicating that the conductive coating layer was successfully deposited onto the Si structure. However, the space between ridges and lamellae layers was blocked by the graphite coating as shown in Figure 3.21. Therefore, the reaction duration was reduced to 0.5 h in order to obtain a uniform coating, but not to block the paths.

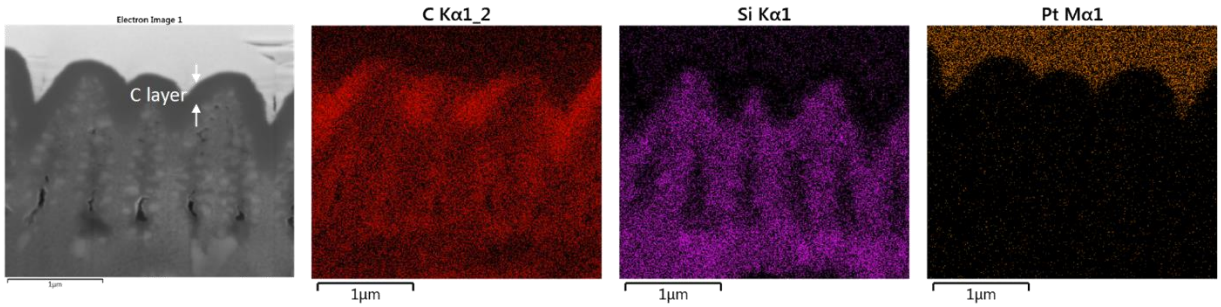

Figure 3.21. A FIB-milled cross-sectional SE image and EDS maps of C, Si and Pt (protective layer coating) of Si/C replicas after methane vapor deposition on Si replicas at 950 ˚C for 6 h.

The appearance of the Si replicas and the alumina crucible which contained the samples changed color after conducting carbon vapor deposition at 950 ˚C for 0.5 h. Figure 3.22 confirmed carbon deposition on the Si replicas by the uniformly distributed metallic grey color of graphite. The XRD scan (Figure 3.23(b)) detected graphite from the replicas after carbon vapor deposition, although the graphite coating can't be clearly distinguished in the cross-sectional SE image (Figure 3.23(a)). Hence, it can be concluded that after carbon vapor deposition on Si replicas at 950 ˚C for 0.5 h, graphite was coated on the Si structure based on the color indication and XRD analyses; and the coating thickness was very thin which cannot be even observed under high resolution SEM. TEM imaging will be needed in the future to observe the coating and obtain thickness information.

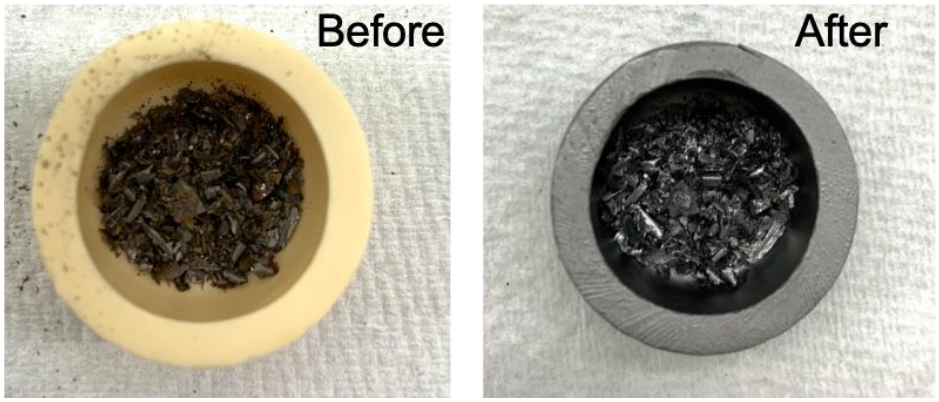

Figure 3.22. A photograph of the Si replicas placed in an alumina crucible (left) and the Si/C replicas inside the same crucible (right) after carbon vapor deposition at 950 ˚C for 0.5 h.

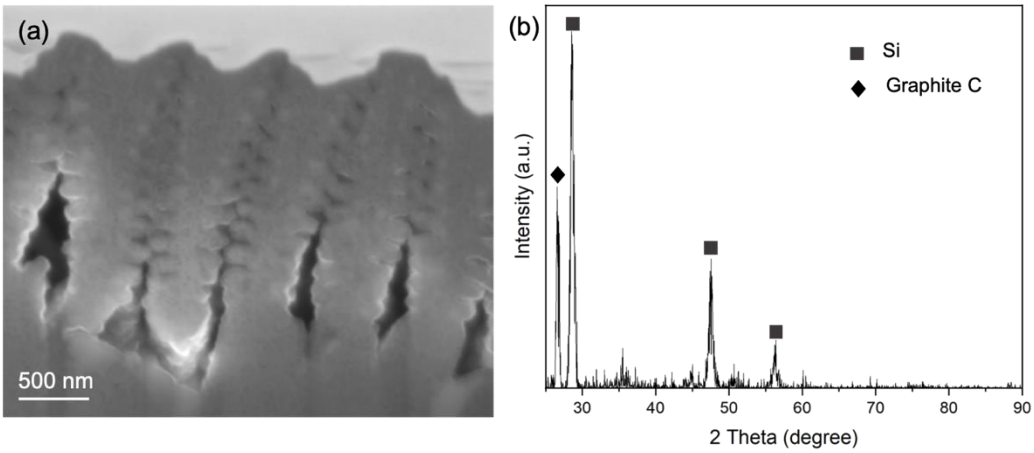

Figure 3.23. (a) FIB-milled cross-sectional SE image and (b) XRD analyses of the Si/C replicas prepared by carbon vapor deposition on Si replicas at 950 ˚C for 0.5 h.

3.4 Conclusions

In this chapter, the hierarchically-patterned, periodic 3D nanostructure of the *Morpho rhetenor* butterfly wing scales was successfully replicated in SiO_2 via silica sol-gel coating and organic pyrolysis. The SiO_2 replicas were further converted into MgO/Si via magnesiothermic reduction, then porous Si by selective dissolution of MgO, and finally high-refractive-index Mg_2Si via Mg-Si gas-solid chemical reaction, in order to enhance IR reflectance of such replicated structure. The intricate "Christmas-tree" structure was retained well throughout the whole chemical conversion process. In addition, to achieve a precise control of the coating thickness, a layer-by-layer surface sol-gel (SSG) process was developed using silicon alkoxide (TEOS) as the precursor. The SSG coating was conducted using an automated dip coater to repeat the coating cycle for 100 and 150 times, respectively, in order to establish the correlation between the number of coating cycles and the coating thickness. To measure the optical behavior of the replicas, reflectivity measurements were conducted on the sol-gel coated SiO_2 replicas, and the reflectance was "blue-shifted" (peak reflectivity wavelength decreased) compared to the native *Morpho rhetenor* reflectance. Such observation was consistent with the decrease of the refractive index from chitin to SiO_2. This helped confirm the assumption of enhanced IR reflectivity with high-refractive-index Mg_2Si replicas. The IR reflectivity of Mg_2Si replicas will be pursued in the future.

Si/C hybrid replicas were also successfully fabricated via two methods: charring the wing template to retain the native carbon; and/or applying a conformal carbon thin layer using methane as the vapor deposition precursor. Such replicas have great potential to be used as anode material in Li-ion batteries due to the high surface area of the nanostructure and conductive and mechanical properties provided by carbon.

4. DEPOSITION KINETICS OF SILICON ALKOXIDE ON CHITIN/CHITOSAN

4.1 Introduction

The surface sol-gel (SSG) process involves the stepwise chemical adsorption of metal alkoxides to form an ultrathin coating [117]. Precise control of coating thickness can be achieved by adjusting the number of the SSG cycles. Ideally, a single monolayer can be deposited with each cycle of the SSG process [113]. A variety of oxides have been deposited using the SSG method, such as Ti-O [118], Sn-O, Sm-O, Ba-O, Zr-O and Fe-O [117, 119]. It has been found that different precursors (oxides) react at different rates [119]. There have been a few reports of the SSG process using a Si-O precursor. Nina I. Kovtyukhova, *et al*. reported using a SSG technique to synthesis silica nanotubes within an anodic aluminum oxide membrane by using $SiCl_4$ as a silicon precursor [120]. Xin Zhang, *et al*. utilized $SiCl_4$ to deposit silica thin films on polyimide substrates using the SSG technique [121]. However, few studies of the surface sol-gel deposition kinetics of Si-O alkoxide precursor have been found, probably due to low hydrolysis rate [119]. When Ichinose, *et al*. conducted a research to evaluate the SSG kinetics using $Si(O\text{-}Me)_4$, they concluded that the adsorption required a stronger condition than for other metal alkoxides and was less reproducible than for other oxides [119]. Indeed, when preparing silica sol-gel solutions using a Si precursor (tetraethyl orthosilicate, TEOS) in Chapter 1 of this thesis, acid was added as a catalyst to promote hydrolysis of the alkoxide.

In Chapter 3 of this thesis, a pH-adjusted Si-O precursor was successfully deposited on native butterfly wings using the SSG coating process. The butterfly wings are made of mostly chitin, which has abundant hydroxyl groups that can react and bond with Si-O precursor molecules. Evaluating the adsorption between silicon alkoxide and hydroxyl groups from chitin (chitosan) became critical to better understand and control the SSG coating process on the native butterfly wings to replicate its unique structure, and furthermore, to extend the possibility of utilizing SSG process to precisely deposit Si-O precursors on other surfaces for a variety of applications.

A key component of butterfly wings, chitin, is the world's second most abundant naturally-occurring polysaccharide [122]. It has been found in a wide range of natural structures, formed by fungi, insects, crustaceans, mollusks, etc. Chitosan, a copolymer of glucosamine and N-glucosamine, is a partially deacetylated format of chitin, and can be purchased from commercial

vendors [123–125]. In this study, commercially-purchased chitosan powder has been used to mimic the adsorption of Si-O precursor (TEOS) onto the native butterfly wings. The chemical structure of chitosan is shown in Figure 4.1. The mole fraction of deacetylated units (i.e., the degree of deacetylation) is usually 70-90 %. Chitin and chitosan are being used in major research areas including medical, cosmetics, agriculture, food industries, pulp and paper, biotechnology, chemical production, and environmental applications [122].

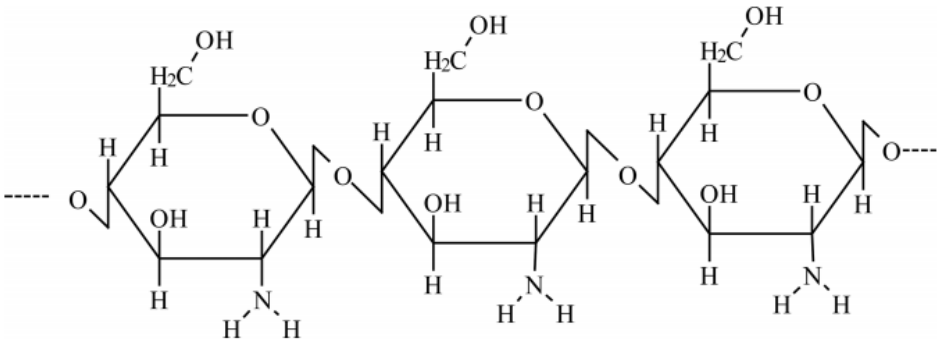

Figure 4.1. Structure of chitosan.

The purpose of this chapter is to enhance the adsorption rate of a Si-O precursor (TEOS) to hydroxyl groups, and most importantly, to investigate the kinetics and adsorption isotherms of the SSG adsorption process. With better understanding of the kinetic mechanism(s) of such binding between silica alkoxide and chitosan, the time required to achieve equilibrium adsorption of Si-O alkoxide onto native chitin templates can be determined.

4.2 Possible Kinetic Mechanisms

4.2.1 Mass Transport (Liquid Phase Diffusion)

Adsorption can be controlled by the mass transport of a reactant species forwards, or product species from, the solid/liquid interface. For liquid phase diffusion control, the change of adsorption with time, denoted as $d(\Gamma_i^t)/dt$ (change in adsorbed mass per area per time), can be expressed by a Noyes-Whitney-Nernst-type equation [126, 127]:

$$\frac{d(\Gamma_i^t)}{dt} = \frac{D_i\,(C_b - C_s)}{\delta_i} \qquad \text{Eqn. 4.1}$$

where D_i is the diffusion coefficient of a species i through a concentration boundary layer in the liquid; C_s, C_b are the concentration of this species in the liquid at the solid/liquid interface and in the bulk solution, respectively; and δ_i is the concentration boundary layer thickness for species i, which can be described as follows for laminar flow past a flat plate [128]:

$$\delta_i = \frac{4.64(X)^{1/2}(D_i)^{1/3}\nu^{1/6}}{(V)^{1/2}} \qquad \text{Eqn. 4.2}$$

where X is the distance from the leading edge of the plate, ν is the kinematic viscosity of the liquid, and V is the velocity of the bulk liquid.

Hence, for liquid phase diffusion-controlled kinetics, the adsorption rate should be independent of time, and should increase with the square root of the velocity (flow rate) of the bulk liquid past the plate. In addition, if the adsorption kinetic is controlled by liquid phase diffusion, the chemical reaction should be rapid that the concentration at the liquid/solid interface, C_s, reaches equilibrium and is constant [129]. In this case, the adsorption rate is linear with the bulk solution concentration, C_b, which is the concentration of the TEOS solution in our study.

4.2.2 Chemical Reaction at the Solid/Liquid Interface

The chemical reaction between TEOS and chitosan can be expressed as follows:

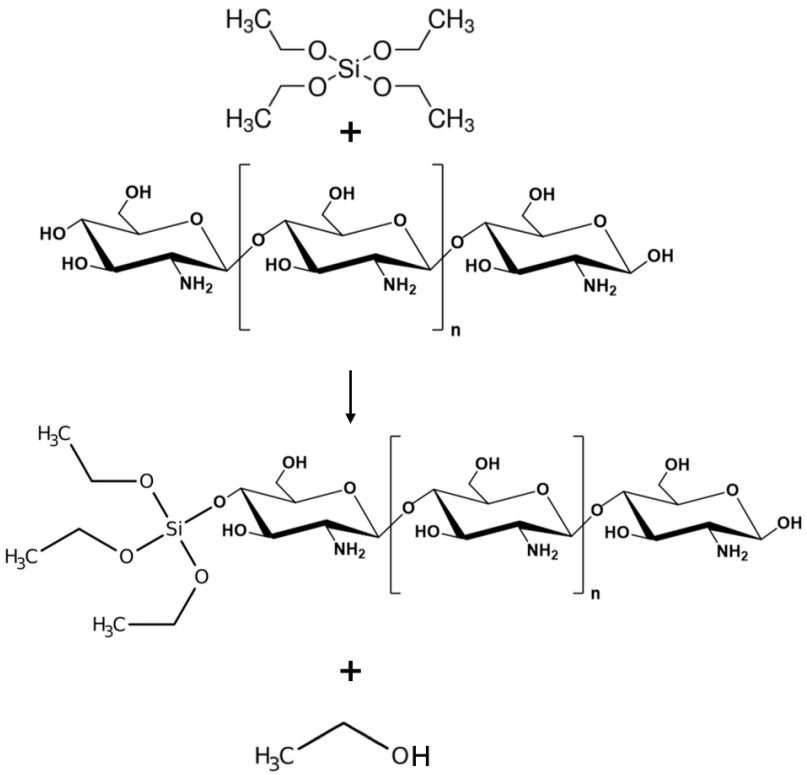

For a chemical-reaction-controlled process, several cases may be evaluated depending on the order of the chemical reaction. If the adsorption rate is controlled by a first order reaction, the change of adsorption with time can be expressed as [130, 131]:

$$\frac{d(\Gamma_i^t)}{dt} = k_1(\Gamma_i - \Gamma_i^t) \qquad \text{Eqn. 4.3}$$

Here, k_1 is a first-order reaction rate constant for adsorption. After rearranging and integrating Eqn. 4.3, we can obtain:

$$\ln[\,\Gamma_i - \Gamma_i^t] = \ln[\Gamma_i] - k_1 t \qquad \text{Eqn. 4.4}$$

Eqn. 4.4 indicates that, if the adsorption process is controlled by a first order reaction, the plots of $\ln[\,\Gamma_i - \Gamma_i^t]$ vs. time will yield a linear straight line.

If adsorption is controlled by a second-order reaction, then the change in adsorption with time can be expressed in the following equation:

$$\frac{d(\Gamma_i^t)}{dt} = k_2(\Gamma_i - \Gamma_i^t)^2 \qquad \text{Eqn. 4.5}$$

By rearranging and integrating the above equation, we obtain:

$$\frac{1}{\Gamma_i - \Gamma_i^t} = \frac{1}{\Gamma_i} + k_2 t \qquad \text{Eqn. 4.6}$$

Therefore, if the adsorption process is controlled by a second order chemical reaction, the plot of $\frac{1}{\Gamma_i - \Gamma_i^t}$ vs. time should yield a straight line, from which k_2 (second-order reaction constant) may be derived from the slope.

Quartz Crystal Microbalance (QCM) provides an in-situ, real-time evaluation of extremely sensitive mass changes from nanograms to micrograms, which makes it a great tool to study the mechanism and kinetics of the adsorption of TEOS onto chitosan in a molecular level. The technology relies on piezoelectric quartz sensor and its responses upon addition or removal of small amounts of mass onto the electrode surface, and it outputs the frequency data of the sensor oscillation. QCM frequency change can be used to calculate the mass adsorbed onto the sensor. The mass gain per area, Δm, can be calculated using the Sauerbrey equation [132–134].

$$\Delta f = -n[2(f_0)^2/\rho_Q \nu_Q](\Delta m) \qquad \text{Eqn. 4.7}$$

where f_0 is the fundamental resonance frequency of the quartz crystal, ρ_Q is the quartz density (2.650 g/cm^3), ν_Q is the wave velocity in quartz plate (3340 m/s), and n is the harmonic number. After rearranging Eqn. 4.7, we can obtain:

$$\Delta m = \frac{-C\,\Delta f}{n} \qquad \text{Eqn. 4.8}$$

where Δm is the change in areal mass, Δf is the difference in resonance frequency, C is the mass sensitivity constant (C = 17.7 ng/cm^2 Hz for a 5 MHz AT-cut quartz crystal [129, 135]), and n is the overtone number.

During the adsorption of TEOS on chitosan, if the adsorption rate is proportional to the square root of the flow rate of TEOS solutions, and also independent of time, then the adsorption rate is consistent with the mass transport control of TEOS molecules. If the adsorption rate is independent of flow rate, then a chemical reaction may be the rate-limiting step during this adsorption process, and QCM data can be plotted and fitted based on the different chemical reaction order models.

4.3 Experimental Design

4.3.1 Materials and Instruments

L-cysteine (BioReagent, ≥ 98% purity), glutaraldehyde (GA, catalog number G151-1) (50% in water), chitosan powder (practical grade) were purchased from Sigma Aldrich (St. Louis, MO, USA). Tetraethyl orthosilicate (98% purity), ethanol (anhydrous, 200 proof), acetic acid (glacial), hydrochloric acid (1.0 M), and sodium dodecyl sulfate (SDS) powder were purchased from Fisher Scientific (Hampton, NH, USA). All water used in the experiments was provided by an in-house water purification system (MilliQ®, Burlington, MA, USA), and it is referred to as DI water in the following text. A traceable pH/ORP meter with standard pH solution calibration function (Cole-Parmer, Vernon Hills, IL, USA) was used to measure the pH values of prepared TEOS precursor solutions. All chemicals were used as received without further purification. QCM Au sensors were supplied by NanoScience Instruments (BL-QSX 301, Phoenix, AZ, USA).

A UV/Ozone cleaner (ProCleaner™ Plus, Bioforce Nanosciences, Salt Lake City, UT) was used to clean the surface of Au sensors before coating deposition. The chitosan coating was deposited on Au sensors using a spin coater (650 Series, Laurell Technologies Corporation, North Wales, PA, USA). The coating solutions were mixed using a rotating shaker (Corning® LSE™ Orbital Shaker, Corning, NY, USA). The QSense Analyzer system (Biolin Scientific, Västra Frölunda, Sweden) was used to conduct QCM-D experiments and analyses.

4.3.2 Surface Functionalization and Chitosan Coating on QCM Au sensors

Before coating, the QCM Au sensors were cleaned first using a protocol recommended by the supplier (NanoScience Instruments). The sensors were first exposed to UV/Ozone for 10 min at room temperature. A cleaning solution containing DI water, ammonia (25 wt %), and hydrogen peroxide (30 wt %) in a 5:1: 1 volume ratio was prepared and heated to 75 ˚C, and the sensors were submerged in this solution for 5 min. Next, the sensors were rinsed thoroughly by spraying DI water onto the sensor for 30 s, and dried with 99.9% purity nitrogen gas (Air Gas, Radnor, PA, USA) at room temperature for 1 min. Lastly, the sensors were UV/Ozone treated again for 10 min.

A 1 wt % L-cysteine solution was prepared by dissolving 0.1 g L-cystein powder in 10 ml of DI water. The solution was further mixed using a rotating shaker at 160 rpm for 30 min. A 5 wt % glutaraldehyde solution was obtained by first adding 1 mL of glutaraldehyde (50 wt % in water)

in a 10 mL volumetric flask, and then adding water until the total solution volume was 10 mL. To prepare a 1 wt % chitosan solution, a 1 wt% acetic acid solution was first made by diluting from the glacial acetic acid. 1 g of chitosan powder was then dissolved in 10.1 mL of 1 wt% acetic acid in the rotating shaker at 200 rpm at 60 ˚C for 3 h.

The process of coating chitosan on the QCM Au sensors was as follows. The cleaned sensors were first immersed in a 1 wt % L-cysteine solution for 24 h to allow for the formation of a self-assembled monolayer (SAM). The sensors were then rinsed by spraying DI water and acetone, respectively, and dried with 99.9% nitrogen at room temperature for 1 min. Then the sensors were immersed in a 5 wt % glutaraldehyde solution for 1 h, followed by spraying with DI water onto the sensors and drying with nitrogen at room temperature for 1 min. Next, the sensors were immersed in a 1 wt % chitosan solution for 3 h. The active side of the Au sensors (Figure 4.2) was then spun at 3000 rpm for 20 s to remove the excessive chitosan to yield a thin chitosan layer. The sensors were dried in a desiccator for 24 h at room temperature before use in the QCM.

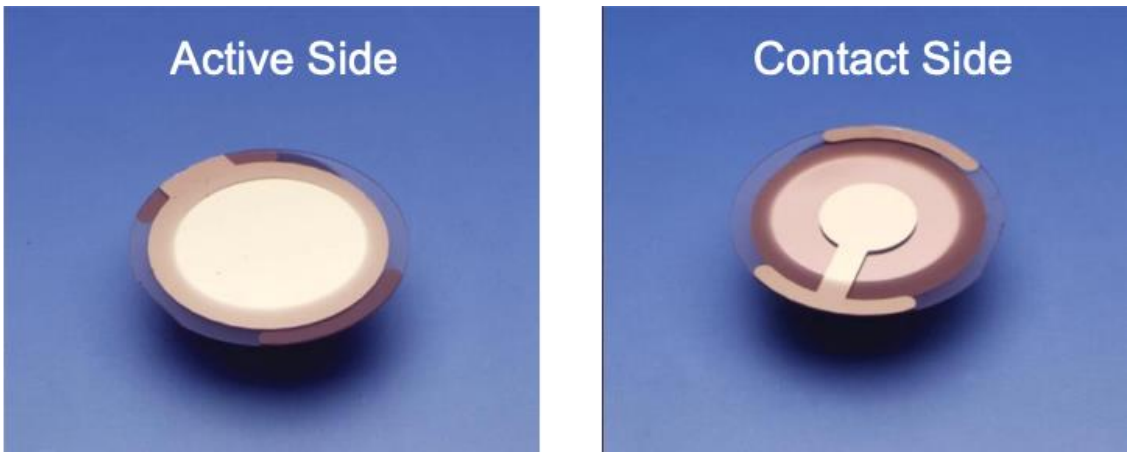

Figure 4.2. Images of the active side and the contact side (back side) of a cleaned QCM Au sensor (image adapted from QSense Analyzer Manual from Biolin Scientific).

The surface chemistry of the chitosan-coated Au sensor, before and after the QCM study, was evaluated using a fourier-transform infrared spectroscometer (FTIR) with an attenuated total reflection (ATR) sampling capability (Shimadzu, Kyoto, Japan). First, a scan was conducted in the laboratory air to eliminate the background environmental interference. Then the sample scan was conducted over the range 500 – 3500 cm^{-1}, and resolution was set to 4 cm^{-1} (i.e., the minimum

peak interval that can be distinguished). The transmittance valley peaks were digitally identified using the FTIR analyses software.

4.3.3 Preparation of Precursor Solutions

Precursor solutions of Si (IV) alkoxide were prepared from tetraethyl orthosilicate (TEOS) diluted with anhydrous ethanol. For example, to prepare 50 mL of a 20 mM TEOS solution in ethanol, 221 µL of TEOS was diluted with ethanol until the total mixture volume is 50 mL. The TEOS solution was mixed by ultrasonicating for 10 min to degas right before use. The ultrasonicating was conducted using an ultrasonic cleaner (Branson, Grainger, Lake Forest, IL, USA). TEOS solutions in other concentrations were prepared in the same fashion. To adjust the pH of the TEOS solutions to 1 ± 0.1, 500 µL of 1 M HCl(aq) was added to the 50 mL volumetric flask after adding TEOS, and ethanol was then added until the total mixture volume reached 50 mL. The pH of the prepared solution was measured using the pH meter. All solutions were prepared immediately before use.

4.3.4 Quartz Crystal Microbalance with Dissipation (QCM-D)

QCM-D is a real-time, surface-sensitive technique that monitors the mass change due to species adsorbed onto a quartz crystal from the change in resonance frequency of the oscillating quartz crystal. As mass is added or removed from the oscillating sensor, there will be a corresponding frequency change. Figure 4.3 illustrates a typical response of a QCM-D system.

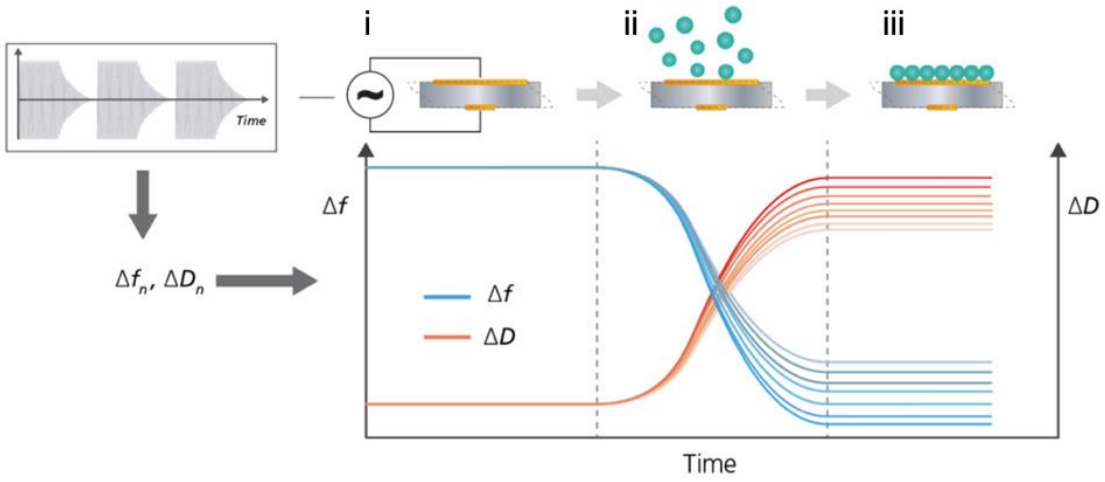

Figure 4.3 A schematic illustration of the operation of the QSense Analyzer, a multi-harmonic QCM-D, which can provide time-resolved information on f and D at multiple harmonics. As the mass is added on the QCM sensor, a real-time measurement of f and D will be recorded. In this schematic scenario, it shows i) bare sensor surface and stable baselines of multiple Δf and ΔD. ii) Molecules bind to the surface, and as a result, the frequencies decrease and the dissipation increase, indicating mass uptake and increasing energy loss. iii) The surface adsorption has completed, and the frequency and dissipation responses have stabilized. Image courtesy of Biolin Scientific (Västra Frölunda, Sweden).

A QCM-D system can also measure dissipation (i.e., energy loss). With the dissipation data, one can evaluate the viscoelasticity of the deposited film on the sensor. The QSense Analyzer used in this study can generate 1^{st}, 3^{rd}, 5^{th}, 7^{th}, 9^{th}, 11^{th}, 13^{th} harmonics, which corresponded to the fundamental frequencies of 5 MHz, 15 MHz, 25 MHz, 35 MHz, 45 MHz, 55 MHz, and 65 MHz, respectively. As shown in Figure 4.4, the area and depth of sensitivity were different for different harmonics. The fundamental harmonic covered the largest sensor area and had the deepest penetration in the deposited film. However, since the area covered by the fundamental harmonic was relatively close to the O-ring that secured the sensor in the chamber, it usually generated some noise that cannot be used to obtain accurate adsorption behavior data [136]. The harmonics with higher n number had lower penetration depth to the film, which reduced the information that was obtained from such relatively weak signals. Therefore, in this study, the 3^{rd} harmonic was used as it was neither extremely noisy nor extremely shallow. All evaluation of TEOS deposition onto chitosan only utilized the 3^{rd} harmonic throughout this study.

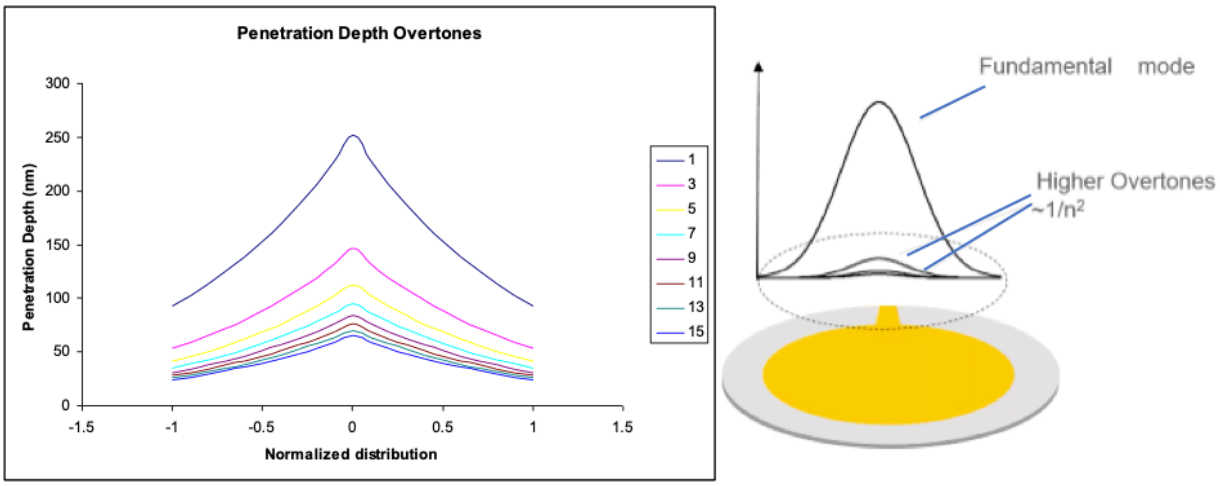

Figure 4.4. Normalized radial amplitude distribution and penetration depth for the frequencies with overtone number, n. Data courtesy of Biolin Scientific (Västra Frölunda, Sweden).

4.3.5 Measurement of Adsorption via Quartz Crystal Microbalance

To avoid metal alkoxide deposition on regular QCM module inner walls, which are comprised of titanium, the polytetrafluoroethylene (PTFE) flow module was chosen for this study since PTFE did not react with the alkoxide precursors. Before conducting the QCM analyses, the module chamber was cleaned with a flowing 2 % SDS solution at a rate of 400 µL/min for at least 30 min at 25 ˚C, followed by DI water flowing at 400 µL/min for another 30 min, and then anhydrous ethanol flowing at 400 µL/min for 15 minutes. The chamber was then opened and dried with 99.9% nitrogen gas by flowing N_2 gas for 3 min at 1 cfm. The tubing that connected the solution bottles and the modules was also purged with flowing nitrogen gas for 3 min. If the tubing was dried in this manner, then residual moisture would be pumped onto the experimental sensor surface and thereby alter the surface chemistry before the test.

Before introducing liquid into the module chamber, the solutions were degassed for at least 20 min to remove the bubbles trapped in the liquid. Gas bubbles formed on the sensor surface may influence the measured Δf and ΔD values. The QCM-D protocol for studying the adsorption behavior was as follows. A chitosan coated QCM Au sensor was mounted in a PTFE module (Biolin Scientific, Västra Frölunda, Sweden). The module chamber target temperature was set to 18 ˚C and left for at least 30 min to achieve a chamber temperature of 18 ˚C ± 0.05. The base overtones of 1^{st}, 3^{rd}, 5^{th}, 7^{th}, 9^{th}, 11^{th}, and 13^{th} resonances of the chitosan-coated Au sensor in air were then established. The sensor was then allowed to achieve a baseline resonance in the flowing

air, followed by a second baseline establishment in flowing anhydrous ethanol. Sufficient time (> 30 min) was needed to establish the baseline in ethanol, due to the temperature fluctuation when introducing new media (i.e., ethanol) into the sensor, O-ring swelling, and chitosan coating swelling. After the baseline in ethanol was achieved, a TEOS solution of a given concentration in ethanol was introduced into the sensor. Figure 4.5 provides an illustration to visualize the TEOS precursor solution flowing over the chitosan-coated Au sensor inside a QCM-D PTFE module chamber. After exposure to the TEOS solution for at least 30 min, anhydrous ethanol was passed over the sensor as a rinsing step to remove excessive and non-chemisorbed alkoxide molecules. It's worth noting that, when changing the media (i.e., from air to ethanol, from ethanol to TEOS solution, etc.), the pump was first stopped before switching the inlet tubing. This would help prevent the formation of gas bubbles and minimized pressure changes in the tubing and module chamber. To analyze the adsorption rate and amount, the 3rd harmonic was used in the Sauerbrey equation (Eqn. 4.8) to calculate the adsorbed mass.

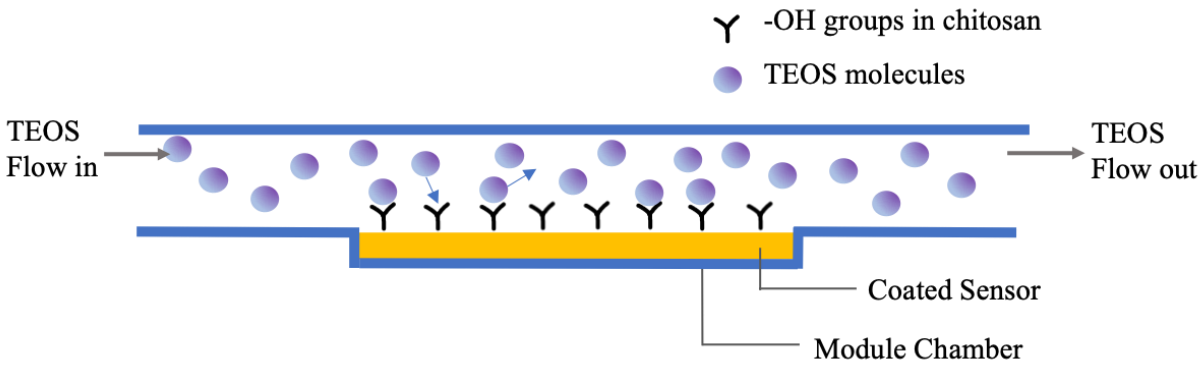

Figure 4.5. Illustration of the cross-sectional view of the QCM module chamber when flowing TEOS precursor over a chitosan-coated Au sensor.

Achievement of a stable baseline stability was very important for high sensitivity measurements and reproducible data with the QCM-D instrument. Typically, as a reference, for a clean 5 MHz sensor with a non-reactive coating operated at 25 ˚C and measured with a 3rd harmonic, a frequency drift of < 0.5 Hz/h in air, and < 1.5 Hz/h in water can be expected (Biolin Scientific Operation Guideline). If a sensor did not reach a flat baseline in air after 1 h, a troubleshooting procedure was conducted (e.g., remounting the sensor to adjust mounting stress, checking solvent leaks, re-cleaning the sensor and the module chamber, etc.).

Different flow rates (12.5 µL/min – 100 µL/min) were applied, while other parameters were kept constant, to investigate the relation between adsorption rate ($\frac{\mathrm{d}(\Gamma_i^t)}{dt}$) and flow rate ($V$). If the adsorption rate was found to be dependent of the square root of the flow rate, then the mass transport of the TEOS molecules in the bulk liquid was likely to be the rate-limiting step. If the adsorption rate did not rely on the flow rate, then a chemical reaction between TEOS and chitosan could be the rate-limiting step. Since the order of such chemical reaction was not known, the QCM raw data was plotted in accordance with to the parameters for chemical reaction models with different reaction orders to find the best fit.

TEOS precursors with different concentrations varying from 2.5 mM to 20 mM were exposed to the chitosan-coated Au sensors, while keeping other parameters the same (i.e., flow rate, temperature, etc), to study the effect of the concentration on the reaction kinetics.

4.4 Results and Discussion

4.4.1 Chitosan Coatings on Au Sensors

In order to use QCM-D to study the adsorption of TEOS onto chitosan, the oscillating sensor needs to be coated uniformly with chitosan. The solubility of chitosan powder in water is very low. Studies have shown that adding acid helps protonate the amino groups in chitosan and improves the solubility in water [137, 138], so as to yield uniform, clear chitosan aqueous solutions. In fact, studies have been conducted to pre-coat the QCM sensor and investigate the reaction kinetics. There are in general two ways of coating the QCM sensor with a reactive layer: through physical deposition, such as spin coating, or drop coating [139, 140], and through chemical bonding [141–144]. Among these studies, Triyana, *et al.* [143] developed a chemical bonding method to attach chitosan onto an Au QCM sensor, instead of physically depositing a chitosan layer. In their work, the chitosan layer was immobilized on to the Au sensor surface via a self-assembled monolayer of L-cysteine using glutaraldehyde as a cross-linking agent. Using this method, they claimed that the coated sensor was stable after 10 days of repeated measurements. Physical deposition of chitosan was therefore not used for this study, due to the possibility of the chitosan layer being rinsed off the sensor while flowing solutions continuously.

Fourier-transform infrared spectroscopy (FTIR) was utilized to analyze the coatings before and after the QCM experiments to detect the surface functional groups. Figure 4.6 - Figure 4.8

showed the IR transmittance spectra of a clean Au sensor with no coating, a SAM-chitosan-coated Au sensor surface before and after a QCM experiment during which a 20 mM TEOS precursor was passed over the sensor at 25 µL/min to bond with the chitosan layer, and then ethanol was introduced at 25 µL/min to rinse away the non-bonded TEOS on the sensor surface. Each characteristic transmittance valley peak was digitally identified by the software and the assignments of those peaks to corresponding functional group or chemical bonds are listed in the table below:

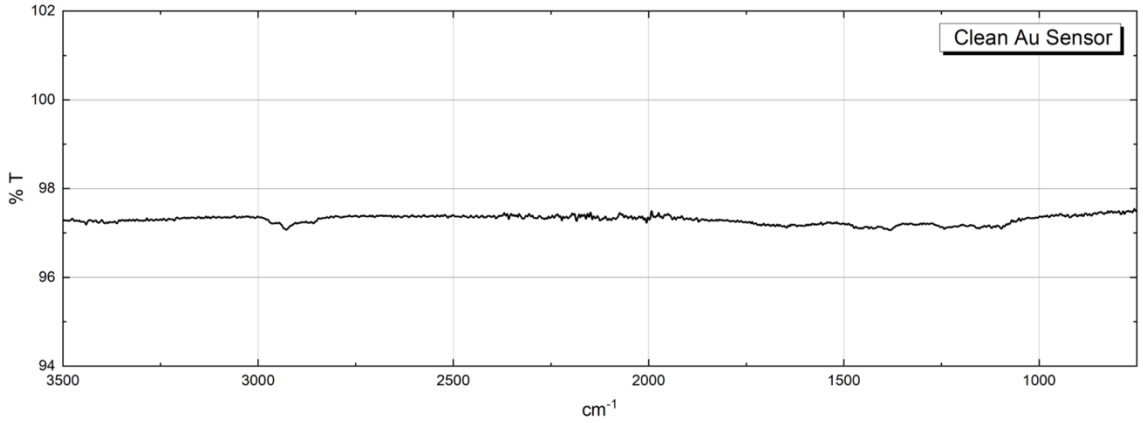

Figure 4.6. FTIR spectra of a clean QCM Au sensor without any coating on.

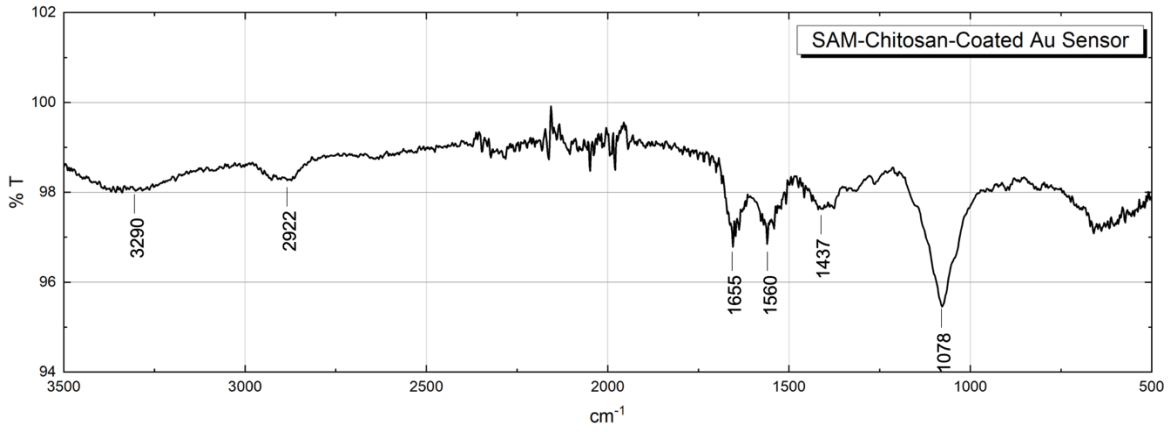

Figure 4.7. FTIR spectra of a chitosan-coated Au sensor using L-cysteine as a SAM layer and glutaraldehyde as a cross-linking agent for chitosan.

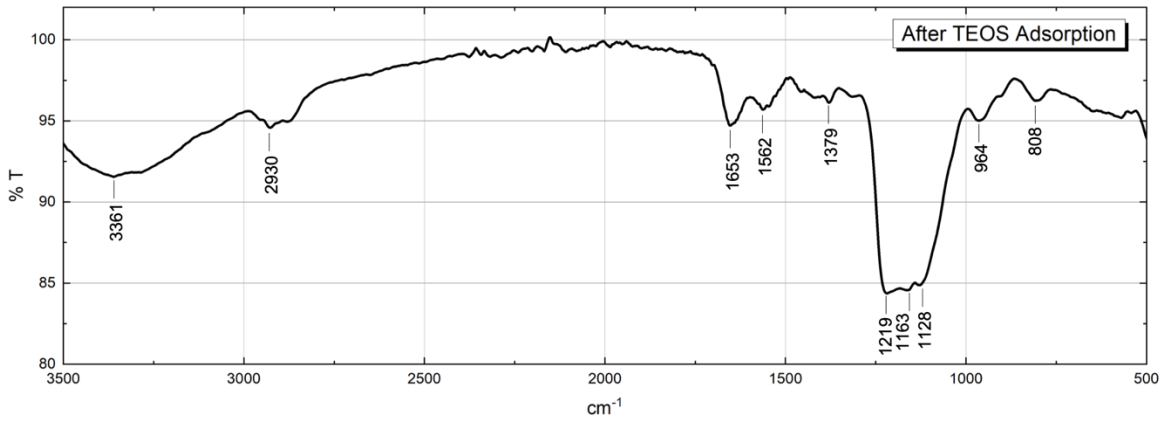

Figure 4.8. FTIR spectra of a chitosan-coated Au sensor after a QCM experiment, during which a 20 mM TEOS solution was passed over the sensor at 25 µL/min.

Table 4-1. FTIR transmittance valley peaks and associate assignments [145–148] to corresponding chemical bonds for Figure 4.7 and Figure 4.8, respectively.

Figure 4.7	
cm^{-1}	**Assignment**
1078	C-O stretch
1437	C-H stretch
1560	N-H stretch from amine
1655	C=O (Amide I)
2930 - 2874	C-H stretch
3290	O-H and N-H stretch

Figure 4.8	
cm^{-1}	**Assignment**
808	Si-O-Si stretch
964	Si-OH stretch
1128	C-O stretch
1163	C-H stretch (CH_3 in TEOS)
1219	Si-O-Si stretch
1379	Si-C stretch
1562	N-H stretch from amine
1653	C=O (Amide I)
1458 - 1379	C-C stretch
2930	C-H stretch
3500 - 3000	O-H stretch

The FTIR characteristic peak locations corresponded well to the presumed functional groups associate with the chitosan layer and TEOS precursor. The FTIR spectra of the Au sensor before the QCM experiment indicated hydroxyl groups (O-H) and amine groups (N-H), confirming that chitosan was coated successfully onto the Au sensor. After the QCM run, the FTIR spectra of the same sensor showed C-H bonds and Si-O-Si bonds, consistent with the deposition and chemical binding of TEOS molecules to chitosan.

SEM and EDS analyses were conducted on the chitosan-coated Au sensor after a QCM study, in which a 20 mM TEOS precursor solution was flowed at 25 µL/min over the coated sensor. As indicated in Figure 4.9, Si was detected from the sensor after the QCM study, and the distribution was uniform over the imaging area. The presence of Si confirmed the binding of TEOS with the chitosan on the QCM sensor.

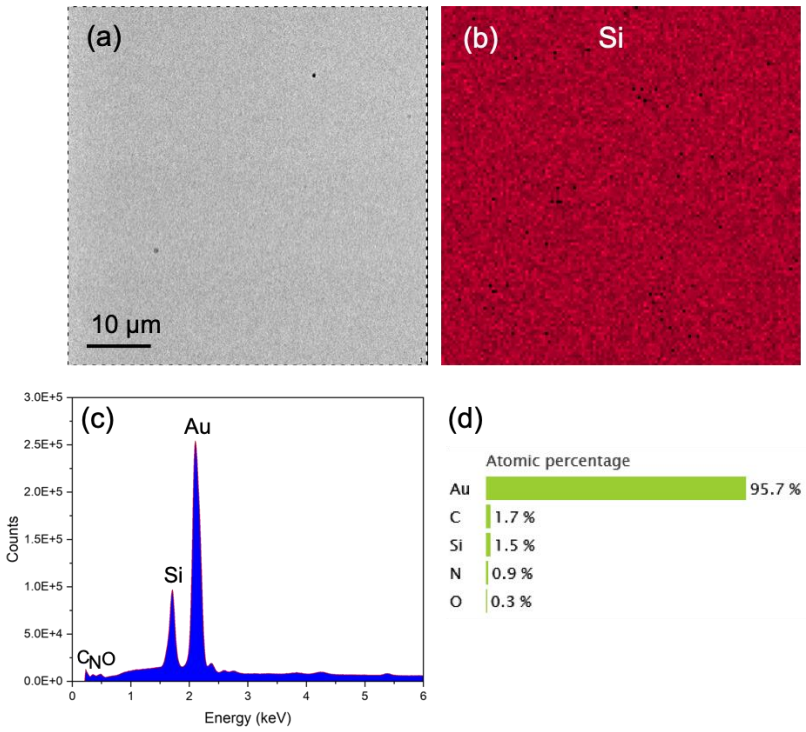

Figure 4.9. (a) Top-down SE image, (b)elemental mapping of Si, and (c)(d) EDS analyses of a chitosan-coated Au sensor after exposure to a 20 mM TEOS solution at 25 µL/min in the QCM-D system.

4.4.2 Determination of Adsorption Kinetics (Rate-limiting Step)

The rate-limiting step of adsorption of TEOS onto chitosan at 18˚C was investigated using a QCM-D instrument. The pH of the TEOS/ethanol solution was adjusted to 1 by using 1 M HCl (aq). To study the flow rate effect on the reaction kinetics, different flow rates were used for this study: 12.5 µL/min, 25 µL/min, 50 µL/min and 100 µL/min. TEOS solution concentrations were also varied from 2.5 mM, 5 mM, 7.5 mM, 10 mM and 20 mM to study the kinetic dependency on the concentration, while keeping the flow rate constant at 25 µL/min. The slopes of the frequency vs. time plots were used to measure the adsorption rates under different flow rates. When switching from the flowing baseline ethanol to TEOS precursor solution, the frequency decreased as mass was added to the chitosan-coated sensor. The frequency continued to decrease until a steady state was reached. When switching from the flowing TEOS precursor solution to ethanol, the frequency increased as the non-adsorbed TEOS was rinsed off of the chitosan-coated sensor. After reaching a steady state during the ethanol rinsing step, the measurement was stopped.

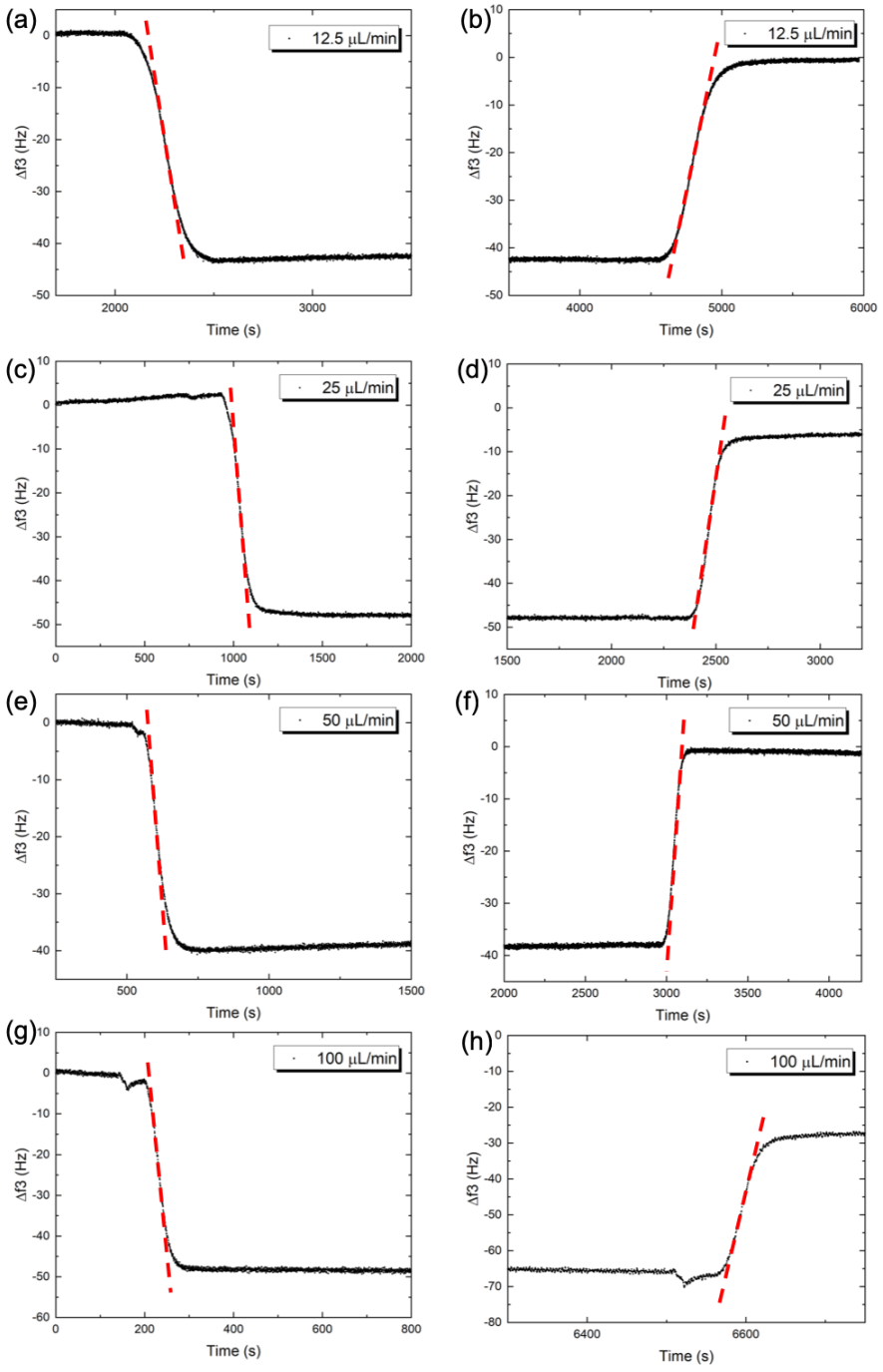

Figure 4.10. Plots of the resonant frequency shift as a function of time when flowing 20 mM TEOS precursor over a SAM-chitosan coated Au sensor at 18 ˚C using different flow rates. (a)(c)(e)(g): Δf vs t plots when introducing TEOS to the sensor (adsorption), (b)(d)(f)(h): Δf vs t plots when rinsing with ethanol after reaching a steady state with the flowing TEOS precursor solution (desorption). The flow rates were stated in the legendry of each plot. From top row to bottom row, the flow rates were 12.5 µL/min, 25 µL/min, 50 µL/min and 100 µL/min, respectively.

Table 4-2. Linear regression slope values and R^2 values of adsorption and desorption of TEOS onto the chitosan-coated surface at different flow rates.

Flow Rate (μL/min)	**Adsorption Linear Fit Slope (+)**	**Adsorption Linear Fit R^2**	**Desorption Linear Fit Slope**	**Desorption Linear Fit R^2**
12.5	0.194 ± 0.0006	0.997	0.150 ± 0.0003	0.998
25	0.419 ± 0.0022	0.997	0.350 ± 0.0019	0.997
50	0.630 ± 0.0019	0.998	0.430 ± 0.0021	0.997
100	0.963 ± 0.0073	0.997	0.887 ± 0.0074	0.996

As shown in Figure 4.10, the frequency changed linearly with time when introducing the flowing TEOS precursor solution and when rinsing with ethanol in the QCM-D module chamber. Therefore, the adsorption and desorption rates ($d(\Gamma_i^t)/dt$) were independent of time. Next, the correlations of adsorption/desorption rates with the flow rate (V) were also investigated. The adsorption rate was obtained from the slopes of Δf vs t plots when introducing TEOS precursor solutions (Figure 4.10(a-d)), and the desorption was from the slopes of Δf vs t plots when rinsing with ethanol (Figure 4.10(e-h)). The slope and R^2 values from the linear regressions of adsorption and desorption are listed in Table 4-2. Due to the time required for the initial mixing of the TEOS precursor with baseline ethanol solution, the initial adsorption rate was not used for kinetic calculation (same for the desorption section). Instead, the adsorption rate was obtained by using the change in adsorption with time over the central 50 % of the adsorption time period. Linear regressions were utilized to obtain the slope values. If the adsorption/desorption kinetic was controlled by liquid phase diffusion (mass transport of TEOS molecules to the chitosan-coated sensor surface), then the sorption rate should be independent of time, and increase with the square root of the velocity of the bulk liquid ($V^{1/2}$). Hence, the plots of adsorption/desorption rate as a function of $V^{1/2}$ should yield a straight line.

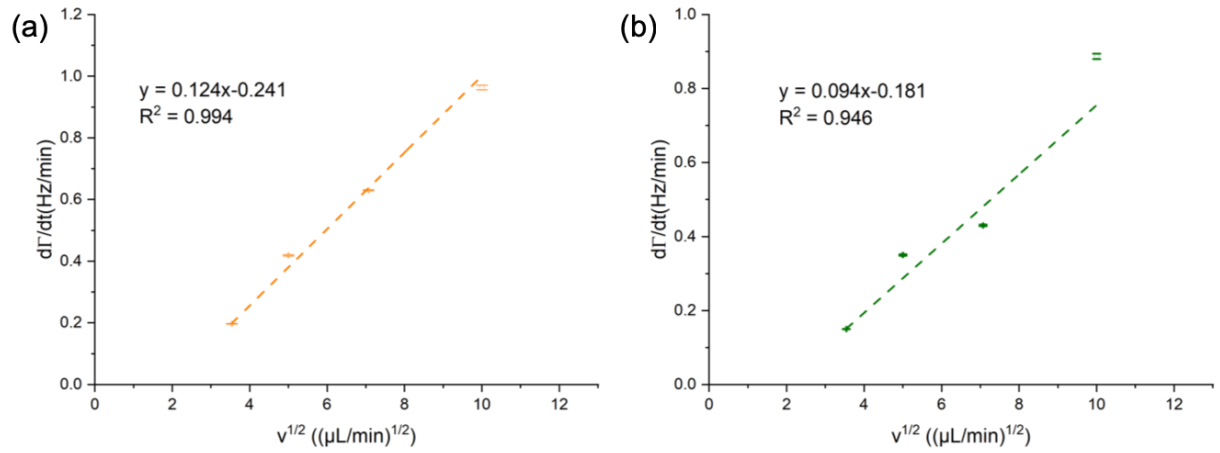

Figure 4.11. Linear regression analyses of (a) adsorption rate and (b) desorption rate as a function of the square root of the flow rate, based on the data from Figure 4.10. Errors represent the standard errors of the linear fit slopes.

The linear regressions for adsorption and desorption both showed a good fit, with R^2 values of 0.995 and 0.957, respectively. The analyses revealed a linear dependence of sorption rate vs square root of the flow rate, which indicated that the rate-limiting step of TEOS adsorption onto chitosan was liquid phase diffusion (when the flow rate was less than 100 µL/min).

Various concentrations of TEOS in ethanol (solution pH = 1) were also evaluated for this study. In general, the frequency shifts from QCM measurements can be interpreted as mass changes, and/or the changes of the density and the viscosity of the solution. To minimize the density and viscosity differences of the TEOS solutions, the concentrations of the TEOS solutions were limited to low values and to a narrow range (i.e., 2.5 mM, 7.5 mM, 5 mM, 10 mM and 20 mM). Within this range, the viscosity and density of the TEOS solution were assumed to remain nearly constant compared to the baseline ethanol solution. The frequency vs. time data using the 3rd harmonics generated by the QCM-D system for adsorption using different TEOS concentrations were plotted and are shown in Figure 4.12. A significant decrease in the frequency shift was observed, indicating an efficient deposition of TEOS onto the chitosan surface. The adsorption rate was obtained from the linear regression slopes from the Δf vs. t plots

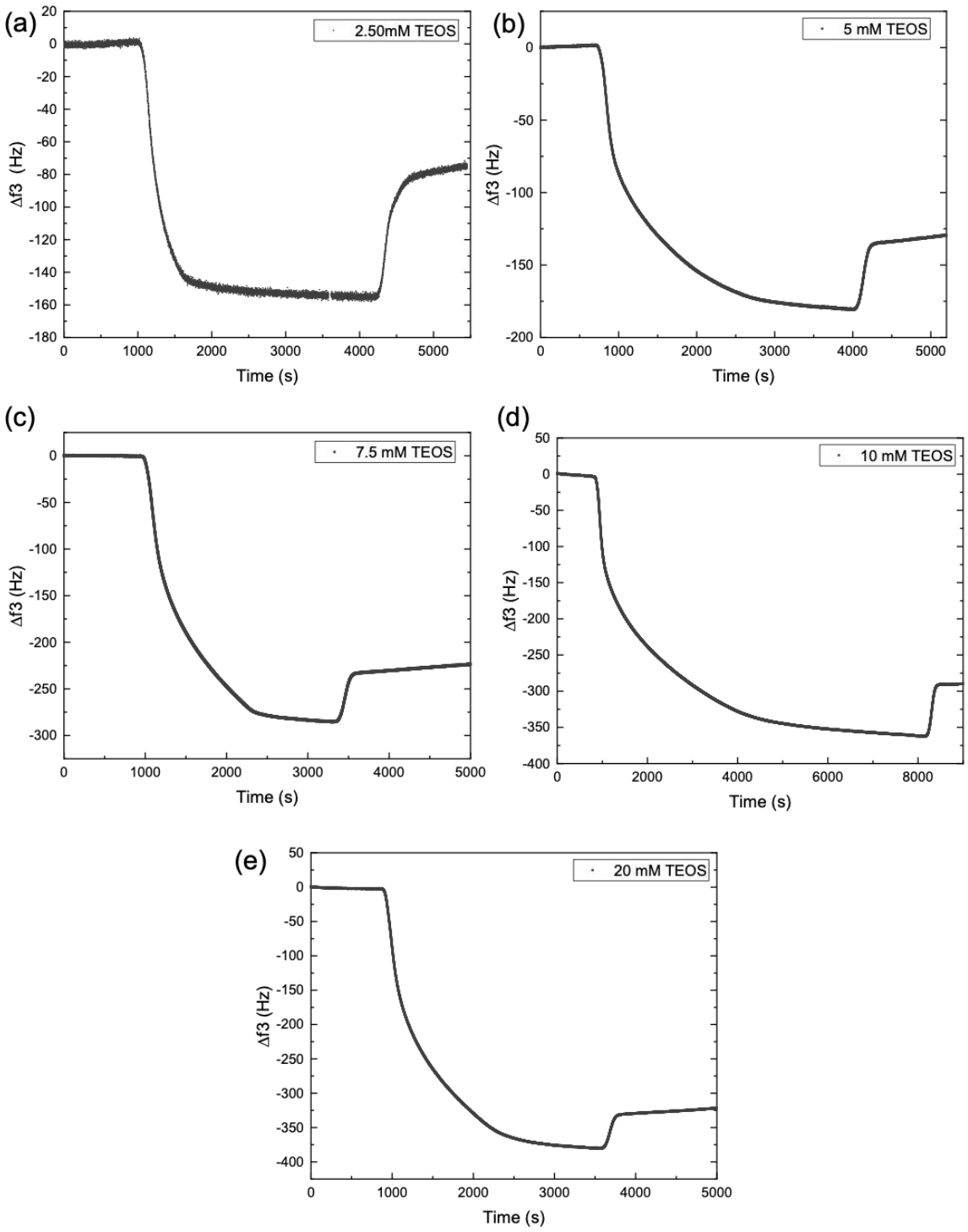

Figure 4.12. Δf_3 vs t plots generated by the raw QCM frequency data from the 3rd harmonic when flowing TEOS (pH = 1) solutions of different concentrations (2.5 mM, 5 mM, 7.5 mM, 10 mM, and 20 mM) over a SAM-chitosan coated Au sensor at a 25 µL/min flow rate.

The adsorption rate when flowing different concentrations of the TEOS solution was obtained from the slope of a linear regression of the Δf vs t plot during adsorption in Figure 4.12. The adsorption linear fit slope values, and the fitting quality of the linear regression (R^2) are listed in the table below:

Table 4-3. Linear regression slope values and R^2 values of adsorption of TEOS onto the chitosan-coated surface for different TEOS solution concentrations.

Concentration (C_i, mM)	**Adsorption Linear Fit Slope (+)**	**R^2**
2.5	0.3373±0.0033	0.981
5	0.4158±0.0015	0.999
7.5	0.5258±0.0017	0.999
10	0.8120±0.0025	0.999
20	1.0187±0.0030	0.998

The adsorption rate vs concentration plot is shown in Figure 4.13. According to the plot, the adsorption rate increased proportionally to the bulk concentration of the TEOS solution. The linear regression of the adsorption rate vs concentration yielded a R^2 value close to 1. The linear dependency of the adsorption rate on the concentration validated the mass transport controlled regime of the TEOS deposition onto a chitosan surface, based on the Noyes-Whitney-Nernst-type equation in Eqn. 4.1.

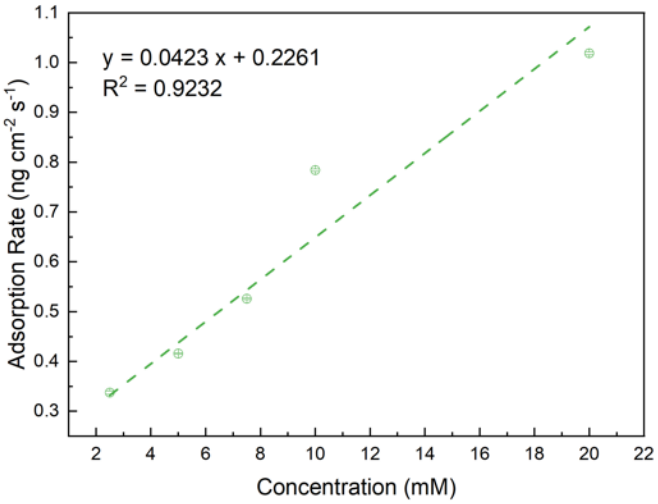

Figure 4.13. Adsorption rate vs. concentration plot when flowing TEOS solutions with various concentrations ranging from 2.5 mM, 5 mM, 7.5 mM, 10 mM and 20 mM onto a chitosan coated QCM Au sensor at a flow rate of 25 μL/min at 18 ˚C.

4.5 Conclusions

In this chapter, the deposition behavior of a silicon alkoxide precursor, tetraethyl orthosilicate, onto a chitosan-bearing surface was investigated using a QCM-D system at 18 ˚C. The chitosan coating was applied to a QCM Au sensor by utilizing L-cysteine to form a self-assembled monolayer on Au and glutaraldehyde as a cross-linking agent to bond with L-cysteine and chitosan. The rate-limiting step during adsorption was evaluated by changing the flow rate of the adsorbate solution, and further validated by changing the concentration of the TEOS solution. It was found that the adsorption rate was linear with the square root of the flow rate, and it increased proportionally with the TEOS concentration. Therefore, it can be concluded that the adsorption of TEOS onto a chitosan surface was liquid-phase-diffusion controlled at 18 ˚C.

REFERENCES

1. Bux, S.K., Yeung, M.T., Toberer, E.S., Snyder, G.J., Kaner, R.B. and Fleurial, J.P., 2011. Mechanochemical synthesis and thermoelectric properties of high quality magnesium silicide. *Journal of Materials Chemistry*, *21*(33), pp.12259-12266.

2. Balout, H., Boulet, P. and Record, M.C., 2014. Thermoelectric properties of Mg_2Si thin films by computational approaches. *The Journal of Physical Chemistry C*, *118*(34), pp.19635-19645.

3. McWilliams, D. and Lynch, D.W., 1963. Indexes of Refraction of Mg_2Si, Mg_2Ge, and Mg_2Sn. *JOSA*, *53*(2), pp.298_1-299.

4. Kato, T., Sago, Y. and Fujiwara, H., 2011. Optoelectronic properties of Mg_2Si semiconducting layers with high absorption coefficients. *Journal of Applied Physics*, *110*(6), p.063723.

5. Chernev, I.M., Shevlyagin, A.V., Galkin, K.N., Stuchlik, J., Remes, Z., Fajgar, R. and Galkin, N.G., 2016. On the way to enhance the optical absorption of a-Si in NIR by embedding Mg_2Si thin film. *Applied Physics Letters*, *109*(4), p.043902.

6. Deng, Q., Wang, Z., Wang, S. and Shao, G., 2017. Simulation of planar Si/Mg_2Si/Si pin heterojunction solar cells for high efficiency. *Solar Energy*, *158*, pp.654-662.

7. Udono, H., Tajima, H., Uchikoshi, M. and Itakura, M., 2015. Crystal growth and characterization of Mg_2Si for IR-detectors and thermoelectric applications. *Japanese Journal of Applied Physics*, *54*(7S2), p.07JB06.

8. Sakamoto, T., Iida, T., Kurosaki, S., Yano, K., Taguchi, H., Nishio, K. and Takanashi, Y., 2011. Thermoelectric behavior of Sb-and Al-doped n-type Mg_2Si device under large temperature differences. *Journal of electronic materials*, *40*(5), pp.629-634.

9. Fedorov, M.I. and Isachenko, G.N., 2015. Silicides: Materials for thermoelectric energy conversion. *Japanese Journal of Applied Physics*, *54*(7S2), p.07JA05.

10. Schmidt, R.D., Case, E.D., Giles, J., Ni, J.E. and Hogan, T.P., 2012. Room-temperature mechanical properties and slow crack growth behavior of Mg_2Si thermoelectric materials. *Journal of electronic materials*, *41*(6), pp.1210-1216.

11. Chen, Z.J., Zhou, B.Y., Li, J.X. and Wen, C.L., 2016. Thermoelectric properties of Al-doped Mg_2Si thin films deposited by magnetron sputtering. *Applied Surface Science*, *386*, pp.389-392.

12. Zhao, Y., Dou, S.X., Ionescu, M. and Munroe, P., 2006. Significant improvement of activation energy in MgB_2 / Mg_2Si multilayer films. *Applied physics letters*, *88*(1), p.012502.

13. Kogut, I. and Record, M.C., 2012. Magnesium silicide thin film formation by reactive diffusion. *Thin Solid Films*, *522*, pp.149-158.

14. Battiston, S., Boldrini, S., Fiameni, S., Famengo, A., Fabrizio, M. and Barison, S., 2012. Multilayered thin films for oxidation protection of Mg_2Si thermoelectric material at middle–high temperatures. *Thin Solid Films*, *526*, pp.150-154.

15. Gordin, A.S. and Sandhage, K.H., 2018. In situ high-temperature X-ray diffraction analysis of Mg_2Si formation kinetics via reaction of Mg films with Si single crystal substrates. *Intermetallics*, *94*, pp.200-209.

16. Chu, W.K., Lau, S.S., Mayer, J.W., Müller, H. and Tu, K.N., 1975. Implanted noble gas atoms as diffusion markers in silicide formation. *Thin Solid Films*, *25*(2), pp.393-402.

17. Lee, H.J., Cho, Y.R. and Kim, I.H., 2011. Synthesis of thermoelectric Mg_2Si by a solid state reaction. *Journal of ceramic processing research*, *12*(1), pp.16-20.

18. Matsui, H., Kuramoto, M., Ono, T., Nose, Y., Tatsuoka, H. and Kuwabara, H., 2002. Growth of Ca2Si layers on Mg_2Si/Si (1 1 1) substrates. *Journal of crystal growth*, *237*, pp.2121-2124.

19. Hosono, T., Matsuzawa, Y., Kuramoto, M., Momose, Y., Tatsuoka, H. and Kuwabara, H., 2003. Simple fabrication of Mg_2Si thermoelectric generator. In *Solid State Phenomena* (Vol. 93, pp. 447-452). Trans Tech Publications Ltd.

20. Hu, J., Sato, Y., Hosono, T. and Tatsuoka, H., 2009. Growth condition dependence of structural and electrical properties of Mg_2Si layers grown on silicon substrates. *Vacuum*, *83*(12), pp.1494-1497.

21. Wittmer, M., Lüthy, W. and Von Allmen, M., 1979. Laser induced reaction of magnesium with silicon. *Physics Letters A*, *75*(1-2), pp.127-130.

22. Goranova, E., Amov, B., Baleva, M., Trifonova, E.P. and Yordanov, P., 2004. Ion beam synthesis of Mg_2Si. *Journal of materials science*, *39*(5), pp.1857-1859.

23. Serikawa, T., Henmi, M. and Kondoh, K., 2004. Microstructure and Mg concentration of Mg–Si thin film deposited by ion beam sputtering on glass substrate. *Journal of Vacuum Science & Technology A: Vacuum, Surfaces, and Films*, *22*(5), pp.1971-1974.

24. Larruquert, J.I. and Keski-Kuha, R.A., 2000. Reflectance measurements and optical constants in the extreme ultraviolet for thin films of ion-beam-deposited SiC, Mo, Mg_2Si, and InSb and of evaporated Cr. *Applied optics*, *39*(16), pp.2772-2781.

25. Song, S.W., Reade, R.P., Kostecki, R. and Striebel, K.A., 2005. Electrochemical studies of the $LiFePO_4$ thin films prepared with pulsed laser deposition. *Journal of the Electrochemical Society*, *153*(1), p.A12.

26. Brinker, C.J. and Scherer, G.W., 2013. *Sol-gel science: the physics and chemistry of sol-gel processing*. Academic press.

27. Vorotilov, K., Petrovsky, V. and Vasiljev, V., 1995. Spin coating process of sol-gel silicate films deposition: effect of spin speed and processing temperature. *Journal of Sol-Gel Science and Technology*, *5*(3), pp.173-183.

28. Ro, J.C. and Chung, I.J., 1989. Sol-gel kinetics of tetraethyl orthosilicate (TEOS) in acid catalyst. *Journal of non-crystalline solids*, *110*(1), pp.26-32.

29. Pope, E.J.A. and Mackenzie, J.D., 1986. Sol-gel processing of silica: II. The role of the catalyst. *Journal of non-crystalline solids*, *87*(1-2), pp.185-198.

30. Fardad, M.A., 2000. Catalysts and the structure of SiO_2 sol-gel films. *Journal of Materials science*, *35*(7), pp.1835-1841.

31. Brinker, C.J., 1988. Hydrolysis and condensation of silicates: effects on structure. *Journal of Non-Crystalline Solids*, *100*(1-3), pp.31-50.

32. Syms, R.R.A. and Holmes, A.S., 1994. Deposition of thick silica-titania sol-gel films on Si substrates. *Journal of non-crystalline solids*, *170*(3), pp.223-233.

33. Kozuka, H. and Higuchi, A., 2003. Stabilization of Poly (vinylpyrrolidone)-containing Alkoxide Solutions for Thick Sol-Gel Barium Titanate Films. *Journal of the American Ceramic Society*, *86*(1), pp.33-38.

34. Allen, T.G., 2018. *Spectroscopic characterization of nonlinear optical and biophotonic materials* (Doctoral dissertation, Georgia Institute of Technology).

35. Nagamori, M., Malinsky, I. and Claveau, A., 1986. Thermodynamics of the Si-CO system for the production of silicon carbide and metallic silicon. *Metallurgical Transactions B*, *17*(3), pp.503-514.

36. Yasuda, K., Nohira, T., Takahashi, K., Hagiwara, R. and Ogata, Y.H., 2005. Electrolytic reduction of a powder-molded SiO_2 pellet in molten $CaCl_2$ and acceleration of reduction by Si addition to the pellet. *Journal of the Electrochemical Society*, *152*(12), p.D232.

37. Davis, S.C., 2012. *Stress and microstructural evolution during shape-preserving silica magnesiothermic reduction* (Doctoral dissertation, Georgia Institute of Technology).

38. Bao, Z., Weatherspoon, M.R., Shian, S., Cai, Y., Graham, P.D., Allan, S.M., Ahmad, G., Dickerson, M.B., Church, B.C., Kang, Z. and Abernathy Iii, H.W., 2007. Chemical reduction of three-dimensional silica micro-assemblies into microporous silicon replicas. *Nature*, *446*(7132), pp.172-175.

39. Sandhage, K.H., Dickerson, M.B., Huseman, P.M., Caranna, M.A., Clifton, J.D., Bull, T.A., Heibel, T.J., Overton, W.R. and Schoenwaelder, M.E., 2002. Novel, bioclastic route to self-assembled, 3D, chemically tailored meso/nanostructures: Shape-preserving reactive conversion of biosilica (diatom) microshells. *Advanced Materials*, *14*(6), pp.429-433.

40. Barin, I., 1989. Thermochemical data of pure substances. *VCH*.

41. Gourishankar, K.V., Ranjbar, M.K. and Pierre, G.S., 1993. Revision of the enthalpies and gibbs energies of formation of calcium oxide and magnesium oxide. *Journal of phase equilibria*, *14*(5), pp.601-611.

42. Hayati-Roodbari, N., Berger, R.J., Bernardi, J., Kinge, S., Hüsing, N. and Elsaesser, M.S., 2017. Monolithic porous magnesium silicide. *Dalton Transactions*, *46*(27), pp.8855-8860.

43. Wu, P., Wang, H., Tang, Y., Zhou, Y. and Lu, T., 2014. Three-dimensional interconnected network of graphene-wrapped porous silicon spheres: in situ magnesiothermic-reduction synthesis and enhanced lithium-storage capabilities. *ACS applied materials & interfaces*, *6*(5), pp.3546-3552.

44. Bass, M., DeCusatis, C., Enoch, J., Lakshminarayanan, V., Li, G., Macdonald, C., Mahajan, V. and Van Stryland, E., 2009. *Handbook of optics, volume i: Geometrical and physical optics, polarized light, components and instruments (set)*. McGraw-Hill, Inc.

45. Mackenzie, J.D., 1982. Glasses from melts and glasses from gels, a comparison. *Journal of Non-Crystalline Solids*, *48*(1), pp.1-10

46. Nayeb-Hashemi, A.A., Clark, J.B. and Pelton, A.D., 1984. The Mg-Si (magnesium-silicon) system. *Bulletin of alloy phase diagrams*, *5*(4), pp.365-374.

47. Chen, W., Tao, X., Zhang, J., Fang, Q. and Yang, J., 2005. Sol–Gel-Processed SiO_2/TiO_2/Methylcellulose Composite Materials for Optical Waveguides. *Journal of the American Ceramic Society*, *88*(11), pp.2998-3002.

48. Powder Diffraction File Card No. 45–946 for MgO, International Center for Diffraction Data

49. Powder Diffraction File Card No. 27–1402 for Si, International Center for Diffraction Data

50. Powder Diffraction File Card No. 35–0773 for Mg_2Si, International Center for Diffraction Data

51. Freund, L.B. and Suresh, S., 2004. *Thin film materials: stress, defect formation and surface evolution*. Cambridge university press.

52. Xia, Z., Davis, S.C., Eftekhar, A.A., Gordin, A.S., Askari, M., Li, Q., Ghasemi, F., Sandhage, K.H. and Adibi, A., 2014. Magnesiothermically Formed Porous Silicon Thin Films on Silicon-on-Insulator Optical Microresonators for High-Sensitivity Detection. *Advanced Optical Materials*, *2*(3), pp.235-239.

53. Roessler, D.M. and Huffman, D.R., 1997. Magnesium Oxide (MgO). In *Handbook of optical constants of solids* (pp. 919-955). Academic Press.

54. Noyes, J., Sumper, M. and Vukusic, P., 2008. Light manipulation in a marine diatom. *Journal of Materials Research*, *23*(12), pp.3229-3235.

55. De Stefano, L., Rea, I., Rendina, I., De Stefano, M. and Moretti, L., 2007. Lensless light focusing with the centric marine diatom Coscinodiscus walesii. *Optics Express*, *15*(26), pp.18082-18088.

56. Trevino, J., Liew, S.F., Noh, H., Cao, H. and Dal Negro, L., 2012. Geometrical structure, multifractal spectra and localized optical modes of aperiodic Vogel spirals. *Optics express*, *20*(3), pp.3015-3033.

57. Lawrence, N., Trevino, J. and Dal Negro, L., 2012. Control of optical orbital angular momentum by Vogel spiral arrays of metallic nanoparticles. *Optics letters*, *37*(24), pp.5076-5078.

58. Bozinovic, N., Golowich, S., Kristensen, P. and Ramachandran, S., 2012. Control of orbital angular momentum of light with optical fibers. *Optics letters*, *37*(13), pp.2451-2453.

59. Choi, S.S., Lee, S.G., Im, S.S., Kim, S.H. and Joo, Y.L., 2003. Silica nanofibers from electrospinning/sol-gel process. *Journal of Materials Science Letters*, *22*(12), pp.891-893.

60. Siouffi, A.M., 2003. Silica gel-based monoliths prepared by the sol–gel method: facts and figures. *Journal of Chromatography A*, *1000*(1-2), pp.801-818.

61. Holmes, A.S., Syms, R.R., Li, M. and Green, M., 1993. Fabrication of buried channel waveguides on silicon substrates using spin-on glass. *Applied optics*, *32*(25), pp.4916-4921.

62. Yamaguchi, T., Serikawa, T., Henmi, M., Oginuma, H. and Kondoh, K., 2006. Mg_2Si coating technology on magnesium alloys to improve corrosion and wear resistance. *Materials transactions*, *47*(4), pp.1026-1030.

63. Mahan, J.E., Vantomme, A., Langouche, G. and Becker, J.P., 1996. Semiconducting Mg_2Si thin films prepared by molecular-beam epitaxy. *Physical Review B*, *54*(23), p.16965.

64. Hu, J., Sato, Y., Hosono, T. and Tatsuoka, H., 2009. Growth condition dependence of structural and electrical properties of Mg_2Si layers grown on silicon substrates. *Vacuum*, *83*(12), pp.1494-1497.

65. Xi-Na, W., Yong, W., Jin, Z., Tian-Chong, Z., Zeng-Xia, M., Yang, G., Qi-Kun, X., Xiao-Long, D., Xiao-Na, Z., Xiao-Dong, H. and Ze, Z., 2009. Thermal stability of Mg_2Si epitaxial film formed on Si (111) substrate by solid phase reaction. *Chinese Physics B*, *18*(7), p.3079.

66. Xiao, Q., Fang, D., Liu, X., Liao, Y., Zhao, K. and Xie, Q., 2017. Heat treatment temperature effects on the formation of Mg_2Si films deposited by electron beam evaporation. *Journal of Materials Science: Materials in Electronics*, *28*(1), pp.702-706.

67. Vantomme, A., Mahan, J.E., Langouche, G., Becker, J.P., Van Bael, M., Temst, K. and Van Haesendonck, C., 1997. Thin film growth of semiconducting Mg_2Si by codeposition. *Applied physics letters*, *70*(9), pp.1086-1088.

68. Vantomme, A., Langouche, G., Mahan, J.E. and Becker, J.P., 2000. Growth mechanism and optical properties of semiconducting Mg_2Si thin films. *Microelectronic engineering*, *50*(1-4), pp.237-242.

69. Perrow, J.M., Smeltzer, W.W. and Embury, J.D., 1968. The role of structural defects in the growth of nickel oxide films. *Acta Metallurgica*, *16*(10), pp.1209-1218.

70. Levenspiel, O., 1999. Chemical reaction engineering. *Industrial & engineering chemistry research*, *38*(11), pp.4140-4143.

71. Alves, H., Koster, U., Aghion, E. and Eliezer, D., 2001. Environmental Behavior of Magnesium and Magnesium Alloysd. *Materials Technology*, *16*(2), pp.110-126.

72. Mikhail, R.S. and Gouda, V.K., 1960. Rate of oxidation of magnesium metal in dry oxygen. *Journal of Applied Chemistry*, *10*(9), pp.384-388.

73. Leontis, T.E. and Rhines, F.N., 1946. Rates of high temperature oxidation of magnesium and magnesium alloys. *Trans AIME*, *166*, pp.265-294.

74. Murray, J.L., 1986. The Mg− Ti (magnesium-titanium) system. *Bulletin of alloy phase diagrams*, *7*(3), pp.245-248.

75. Nayeb-Hashemi, A.A., Clark, J.B. and Swartzendruber, L.J., 1985. The Fe− Mg (Iron-Magnesium) system. *Bulletin of Alloy Phase Diagrams*, *6*(3), pp.235-238.

76. Haitani, T., Tamura, Y., Motegi, T., Kono, N. and Tamehiro, H., 2003. Solubility of iron in pure magnesium and cast structure of Mg-Fealloy. *In Materials science forum* (Vol. 419, pp. 697-701). Trans Tech Publications Ltd., Zurich-Uetikon, Switzerland.

77. Okamoto, H., 2000. Cr-Mg (chromium-magnesium). *Journal of phase equilibria*, *21*(2).

78. Silberglied, R.E., 1984. Visual communication and sexual selection among butterflies. *The biology of butterflies*.

79. Vukusic, P. and Sambles, J.R., 2003. Photonic structures in biology. *Nature*, *424*(6950), pp.852-855.

80. Boulenguez, J., Berthier, S. and Leroy, F., 2012. Multiple scaled disorder in the photonic structure of Morpho rhetenor butterfly. *Applied Physics A*, *106*(4), pp.1005-1011.

81. Ghiradella, H., 1991. Light and color on the wing: structural colors in butterflies and moths. *Applied optics*, *30*(24), pp.3492-3500.

82. Yoshioka, S. and Kinoshita, S., 2004. Wavelength–selective and anisotropic light–diffusing scale on the wing of the morpho butterfly. *Proceedings of the Royal Society of London. Series B: Biological Sciences*, *271*(1539), pp.581-587.

83. Vukusic, P., Sambles, J.R., Lawrence, C.R. and Wootton, R.J., 1999. Quantified interference and diffraction in single Morpho butterfly scales. *Proceedings of the Royal Society of London. Series B: Biological Sciences*, *266*(1427), pp.1403-1411.

84. Saito, A., Ishikawa, Y., Miyamura, Y., Akai-Kasaya, M. and Kuwahara, Y., 2007, October. Optimization of reproduced Morpho-blue coloration. In *Photonic Crystals and Photonic Crystal Fibers for Sensing Applications III* (Vol. 6767, p. 676706). International Society for Optics and Photonics.

85. Tippets, C.A., Fu, Y., Jackson, A.M., Donev, E.U. and Lopez, R., 2016. Reproduction and optical analysis of Morpho-inspired polymeric nanostructures. *Journal of Optics*, *18*(6), p.065105.

86. Potyrailo, R.A., Bonam, R.K., Hartley, J.G., Starkey, T.A., Vukusic, P., Vasudev, M., Bunning, T., Naik, R.R., Tang, Z., Palacios, M.A. and Larsen, M., 2015. Towards outperforming conventional sensor arrays with fabricated individual photonic vapour sensors inspired by Morpho butterflies. *Nature communications*, *6*(1), pp.1-12.

87. Gralak, B., Tayeb, G. and Enoch, S., 2001. Morpho butterflies wings color modeled with lamellar grating theory. *Optics express*, *9*(11), pp.567-578.

88. Plattner, L., 2004. Optical properties of the scales of Morpho rhetenor butterflies: theoretical and experimental investigation of the back-scattering of light in the visible spectrum. *Journal of the Royal Society Interface*, *1*(1), pp.49-59.

89. Banerjee, S., Cole, J.B. and Yatagai, T., 2007. Colour characterization of a Morpho butterfly wing-scale using a high accuracy nonstandard finite-difference time-domain method. *Micron*, *38*(2), pp.97-103.

90. Song, B., Johansen, V.E., Sigmund, O. and Shin, J.H., 2017. Reproducing the hierarchy of disorder for Morpho-inspired, broad-angle color reflection. *Scientific reports*, *7*, p.46023.

91. Saison, T., Peroz, C., Chauveau, V., Berthier, S., Sondergard, E. and Arribart, H., 2008. Replication of butterfly wing and natural lotus leaf structures by nanoimprint on silica sol–gel films. *Bioinspiration & biomimetics*, *3*(4), p.046004.

92. Watanabe, K., Hoshino, T., Kanda, K., Haruyama, Y., Kaito, T. and Matsui, S., 2005. Optical measurement and fabrication from a Morpho-butterfly-scale quasistructure by focused ion beam chemical vapor deposition. *Journal of Vacuum Science & Technology B: Microelectronics and Nanometer Structures Processing, Measurement, and Phenomena*, *23*(2), pp.570-574.

93. Butt, H., Yetisen, A.K., Mistry, D., Khan, S.A., Hassan, M.U. and Yun, S.H., 2016. Morpho Butterfly-Inspired Nanostructures. *Advanced Optical Materials*, *4*(4), pp.497-504.

94. Leertouwer, H.L., Wilts, B.D. and Stavenga, D.G., 2011. Refractive index and dispersion of butterfly chitin and bird keratin measured by polarizing interference microscopy. *Optics express*, *19*(24), pp.24061-24066.

95. Niu, S., Li, B., Mu, Z., Yang, M., Zhang, J., Han, Z. and Ren, L., 2015. Excellent structure-based multifunction of morpho butterfly wings: A review. *Journal of Bionic Engineering*, *12*(2), pp.170-189.

96. Jo, S., Woo, J.Y., Oh, J.H., Shim, H., Seo, S., Jeon, E.S., Kim, M. and Han, C.S., 2020. Angle-Insensitive Transmission and Reflection of Nanopatterned Dielectric Multilayer Film for Colorful Solar Cells. *ACS Applied Materials & Interfaces*.

97. Szczech, J.R. and Jin, S., 2011. Nanostructured silicon for high capacity lithium battery anodes. *Energy & Environmental Science*, *4*(1), pp.56-72.

98. Nitta, N., Wu, F., Lee, J.T. and Yushin, G., 2015. Li-ion battery materials: present and future. *Materials today*, *18*(5), pp.252-264.

99. Roy, P. and Srivastava, S.K., 2015. Nanostructured anode materials for lithium ion batteries. *Journal of Materials Chemistry A*, *3*(6), pp.2454-2484.

100. Yoon, T., Bok, T., Kim, C., Na, Y., Park, S. and Kim, K.S., 2017. Mesoporous silicon hollow nanocubes derived from metal–organic framework template for advanced lithium-ion battery anode. *ACS nano*, *11*(5), pp.4808-4815.

101. Casimir, A., Zhang, H., Ogoke, O., Amine, J.C., Lu, J. and Wu, G., 2016. Silicon-based anodes for lithium-ion batteries: Effectiveness of materials synthesis and electrode preparation. *Nano Energy*, *27*, pp.359-376.

102. Goodenough, J.B. and Kim, Y., 2011. Challenges for rechargeable batteries. *Journal of Power Sources*, *196*(16), pp.6688-6694.

103. Ma, D., Cao, Z. and Hu, A., Si-based anode materials for Li-ion batteries: a mini review. Nano Micro Lett. 6 (4), 347–358 (2014).

104. Li, Y., Meng, Q., Ma, J., Zhu, C., Cui, J., Chen, Z., Guo, Z., Zhang, T., Zhu, S. and Zhang, D., 2015. Bioinspired carbon/SnO_2 composite anodes prepared from a photonic hierarchical structure for lithium batteries. *ACS Applied Materials & Interfaces*, *7*(21), pp.11146-11154.

105. Xia, Y., Sun, B., Wei, Y., Tao, B. and Zhao, Y., 2017. Simple sol-gel method synthesis of 3-dimension $Li_4Ti_5O_{12}$-TiO_2 nanostructures using butterfly wings as biotemplates for high rate performance lithium-ion batteries. *Journal of Alloys and Compounds*, *705*, pp.58-63.

106. Tang, Y.P., Hong, L., Jin, Y.C., Zhang, H.L. and Zheng, G.Q., 2014. Study on the Bionic Preparation and Properties of TiO_2 as Three-Dimensional Anode Materials for Lithium-Ion Batteries. In *Advanced Materials Research* (Vol. 875, pp. 1507-1510). Trans Tech Publications Ltd.

107. Terranova, M.L., Orlanducci, S., Tamburri, E., Guglielmotti, V. and Rossi, M., 2014. Si/C hybrid nanostructures for Li-ion anodes: An overview. *Journal of Power Sources*, *246*, pp.167-177.

108. Jeong, S., Li, X., Zheng, J., Yan, P., Cao, R., Jung, H.J., Wang, C., Liu, J. and Zhang, J.G., 2016. Hard carbon coated nano-Si/graphite composite as a high performance anode for Li-ion batteries. *Journal of Power Sources*, *329*, pp.323-329.

109. Zhu, X., Jiang, X., Yao, X., Leng, Y., Xu, X., Peng, A., Wang, L. and Xue, Q., 2019. Si/aC Nanocomposites with a Multiple Buffer Structure via One-Step Magnetron Sputtering for Ultrahigh-Stability Lithium-Ion Battery Anodes. *ACS Applied Materials & Interfaces*, *11*(49), pp.45726-45736.

110. Ji, J., Ji, H., Zhang, L.L., Zhao, X., Bai, X., Fan, X., Zhang, F. and Ruoff, R.S., 2013. Graphene-encapsulated Si on ultrathin-graphite foam as anode for high capacity lithium-ion batteries. *Advanced Materials*, *25*(33), pp.4673-4677.

111. Chen, Y., Bao, L., Du, N., Yang, T., Mao, Q., Lu, X., Lin, Y. and Ji, Z., 2018. In situ synthesis of carbon doped porous silicon nanocomposites as high-performance anodes for lithium-ion batteries. *Nanotechnology*, *30*(3), p.035602.

112. Ortega-Trigueros, A., Narciso, J. and Caccia, M., 2020. Synthesis of high-surface area mesoporous SiC with hierarchical porosity for use as catalyst support. *Journal of the American Ceramic Society*, *103*(10), pp.5966-5977.

113. Ichinose, I., Kawakami, T. and Kunitake, T., 1998. Alternate Molecular Layers of Metal Oxides and Hydroxyl Polymers Prepared by the Surface Sol-Gel Process. *Advanced materials*, *10*(7), pp.535-539.

114. Dean, J.A., 1992. *Lange's handbook of chemistry* (Vol. 15). New York: McGraw-Hill.

115. Pallas, N.R. and Harrison, Y., 1990. An automated drop shape apparatus and the surface tension of pure water. *Colloids and Surfaces*, *43*(2), pp.169-194.

116. Adamson, A.W. and Gast, A.P., 1967. *Physical chemistry of surfaces* (Vol. 150, p. 180). New York: Interscience publishers.

117. Ichinose, I., Senzu, H. and Kunitake, T., 1996. Stepwise adsorption of metal alkoxides on hydrolyzed surfaces: A surface sol-gel process. *Chemistry letters*, *25*(10), pp.831-832.

118. Takaki, R., Takemoto, H., Fujikawa, S. and Toyoki, K., 2008. Fabrication of nanofins of TiO_2 and other metal oxides via the surface sol–gel process and selective dry etching. *Colloids and Surfaces A: Physicochemical and Engineering Aspects*, *321*(1-3), pp.227-232.

119. Ichinose, I., Senzu, H. and Kunitake, T., 1997. A surface sol− gel process of TiO_2 and other metal oxide films with molecular precision. *Chemistry of materials*, *9*(6), pp.1296-1298.

120. Kovtyukhova, N.I., Mallouk, T.E. and Mayer, T.S., 2003. Templated surface sol–gel synthesis of SiO_2 nanotubes and SiO_2-insulated metal nanowires. *Advanced materials*, *15*(10), pp.780-785.

121. Zhang, X., Mao, L. and Ma, J., 2012. Surface sol–gel synthesis of silica films on polyimide substrate. *Journal of sol-gel science and technology*, *61*(1), pp.34-38.

122. Gerente, C., Lee, V.K.C., Cloirec, P.L. and McKay, G., 2007. Application of chitosan for the removal of metals from wastewaters by adsorption—mechanisms and models review. *Critical reviews in environmental science and technology*, *37*(1), pp.41-127.

123. Pillai, C.K.S., Paul, W. and Sharma, C.P., 2009. Chitin and chitosan polymers: Chemistry, solubility and fiber formation. *Progress in polymer science*, *34*(7), pp.641-678.

124. No, H.K. and Meyers, S.P., 1995. Preparation and characterization of chitin and chitosan—a review. *Journal of aquatic food product technology*, *4*(2), pp.27-52.

125. Domard, A. and Rinaudo, M., 1983. Preparation and characterization of fully deacetylated chitosan. *International Journal of Biological Macromolecules*, *5*(1), pp.49-52.

126. Noyes, A.A. and Whitney, W.R., 1897. The rate of solution of solid substances in their own solutions. *Journal of the American Chemical Society*, *19*(12), pp.930-934.

127. Nernst, W., 1904. Theorie der Reaktionsgeschwindigkeit in heterogenen Systemen. *Zeitschrift für physikalische Chemie*, *47*(1), pp.52-55.

128. Cussler, E.L. and Cussler, E.L., 2009. *Diffusion: mass transfer in fluid systems*. Cambridge university press.

129. Kubiak, K., Adamczyk, Z. and Oćwieja, M., 2015. Kinetics of silver nanoparticle deposition at PAH monolayers: reference QCM results. *Langmuir*, *31*(10), pp.2988-2996.

130. Ganesan, P., Kamaraj, R. and Vasudevan, S., 2013. Application of isotherm, kinetic and thermodynamic models for the adsorption of nitrate ions on graphene from aqueous solution. *Journal of the Taiwan Institute of Chemical Engineers*, *44*(5), pp.808-814.

131. Maurer, S.A., Bedbrook, C.N. and Radke, C.J., 2012. Competitive sorption kinetics of inhibited endo-and exoglucanases on a model cellulose substrate. *Langmuir*, *28*(41), pp.14598-14608.

132. Ho, Y.S. and McKay, G., 1999. Pseudo-second order model for sorption processes. *Process biochemistry*, *34*(5), pp.451-465.

133. Sauerbrey, G.Z., 1959. The use of quarts oscillators for weighing thin layers and for microweighing. *Z. Phys.*, *155*, pp.206-222.

134. Rodahl, M., Höök, F., Krozer, A., Brzezinski, P. and Kasemo, B., 1995. Quartz crystal microbalance setup for frequency and Q-factor measurements in gaseous and liquid environments. *Review of Scientific Instruments*, *66*(7), pp.3924-3930.

135. Stålgren, J.J.R., Eriksson, J. and Boschkova, K., 2002. A comparative study of surfactant adsorption on model surfaces using the quartz crystal microbalance and the ellipsometer. *Journal of colloid and interface science*, *253*(1), pp.190-195.

136. Andersson, K.I., Eriksson, M. and Norgren, M., 2011. Removal of lignin from wastewater generated by mechanical pulping using activated charcoal and fly ash: Adsorption isotherms and thermodynamics. *Industrial & Engineering Chemistry Research*, *50*(13), pp.7722-7732.

137. Rinaudc, M., Pavlov, G. and Desbrieres, J., 1999. Solubilization of chitosan in strong acid medium. *International Journal of Polymer Analysis and Characterization*, *5*(3), pp.267-276.

138. Rinaudo, M., Pavlov, G. and Desbrieres, J., 1999. Influence of acetic acid concentration on the solubilization of chitosan. *Polymer*, *40*(25), pp.7029-7032.

139. Kittle, J.D., Wang, C., Qian, C., Zhang, Y., Zhang, M., Roman, M., Morris, J.R., Moore, R.B. and Esker, A.R., 2012. Ultrathin chitin films for nanocomposites and biosensors. *Biomacromolecules*, *13*(3), pp.714-718.

140. Casteleijn, M.G., Richardson, D., Parkkila, P., Granqvist, N., Urtti, A. and Viitala, T., 2018. Spin coated chitin films for biosensors and its analysis are dependent on chitin-surface interactions. *Colloids and Surfaces A: Physicochemical and Engineering Aspects*, *539*, pp.261-272.

141. Labidi, A., Salaberria, A.M., Fernandes, S.C., Labidi, J. and Abderrabba, M., 2016. Adsorption of copper on chitin-based materials: Kinetic and thermodynamic studies. *Journal of the taiwan institute of chemical engineers*, *65*, pp.140-148.

142. Tiraferri, A., Maroni, P., Caro Rodríguez, D. and Borkovec, M., 2014. Mechanism of chitosan adsorption on silica from aqueous solutions. *Langmuir*, *30*(17), pp.4980-4988.

143. Triyana, K., Sembiring, A., Rianjanu, A., Hidayat, S.N., Riowirawan, R., Julian, T., Kusumaatmaja, A., Santoso, I. and Roto, R., 2018. Chitosan-based quartz crystal microbalance for alcohol sensing. *Electronics*, *7*(9), p.181.

144. Ayad, M.M., Salahuddin, N. and Minisy, I.M., 2014. Detection of some volatile organic compounds with chitosan-coated quartz crystal microbalance. *Designed monomers and polymers*, *17*(8), pp.795-802.

145. Lawrie, G., Keen, I., Drew, B., Chandler-Temple, A., Rintoul, L., Fredericks, P. and Grøndahl, L., 2007. Interactions between alginate and chitosan biopolymers characterized using FTIR and XPS. *Biomacromolecules*, *8*(8), pp.2533-2541.

146. Rubio, F., Rubio, J. and Oteo, J.L., 1998. A FT-IR study of the hydrolysis of tetraethylorthosilicate (TEOS). *Spectroscopy Letters*, *31*(1), pp.199-219.

147. Essel, T.Y., Koomson, A., Seniagya, M.P.O., Cobbold, G.P., Kwofie, S.K., Asimeng, B.O., Arthur, P.K., Awandare, G. and Tiburu, E.K., 2018. Chitosan composites synthesized using acetic acid and tetraethylorthosilicate respond differently to methylene blue adsorption. *Polymers*, *10*(5), p.466.

148. Gui-Long, X., Changyun, D., Yun, L., Pi-Hui, P., Jian, H. and Zhuoru, Y., 2011. Preparation and characterization of Raspberry-like SiO_2 particles by the sol-gel method. *Nanomaterials and Nanotechnology*, *1*, p.21.